Development and Experimental Validation of Large Eddy Simulation Techniques for the Prediction of Combustion-Dynamic Process in Syngas Combustion: Characterization of Autoignition, Flashback, and Flame-Liftoff at Gas-Turbine Relevant Operating Conditions

FINAL SCIENTIFIC/TECHNICAL REPORT

Reporting Period: October 01, 2011 to August 31, 2015

Principal Authors:

Matthias Ihme (co-PI)

James F. Driscoll (co-PI)

Date Report Issued:

October 12, 2015

DOE Award Number:

DE-FE0007060

Submitting Organization:

University of Michigan
1058 Wolverine Tower, 3003 S. State St.
Ann Arbor, MI 48109-1274 USA

Disclaimer

Abstract

The objective of this closely coordinated experimental and computational research effort is the development of simulation techniques for the prediction of combustion processes, relevant to the oxidation of syngas and high hydrogen content (HHC) fuels at gas-turbine relevant operating conditions. Specifically, the research goals are (i) the characterization of the sensitivity of syngas ignition processes to hydrodynamic processes and perturbations in temperature and mixture composition in rapid compression machines and flow-reactors and (ii) to conduct comprehensive experimental investigations in a swirl-stabilized gas turbine (GT) combustor under realistic high-pressure operating conditions in order (iii) to obtain fundamental understanding about mechanisms controlling unstable flame regimes in HHC-combustion.

Contents

Chapter 1

Background and Motivation

The objective of this closely coordinated experimental and computational research effort is the development of validated simulation techniques for the prediction of autoignition and unstable combustion processes, relevant to the oxidation of syngas and high hydrogen content (HHC) fuels at gas-turbine relevant operating conditions. Specifically, the research goals are (i) to develop improved physics-based LES modeling capabilities for the accurate characterization of autoignition, flashback, and flame liftoff in partially-premixed and stratified gas-turbine combustion regimes; (ii) by applying this LES-combustion model, to perform detailed simulations in order to isolate, understand, and quantify facility effects that are manifested by observed irregularities and stochastic ignition events at high-pressure and low/intermediate temperature conditions; and to conduct comprehensive experimental investigations in a swirl-stabilized gas turbine (GT) combustor under realistic high-pressure operating conditions in order (iii) to obtain fundamental understanding about mechanisms controlling unstable flame regimes in HHC-combustion and (iv) to establish a comprehensive database for LES/RANS model validation and low-order model development.

Detailed experimental studies will be conducted in a swirl-stabilized burner to isolate critical combustion mechanisms that control the flame stability, including autoignition, flashback, and flame liftoff. Combustor stability margins will be characterized and effects of variations in equivalence ratio, H_2/CO composition, and changes in GT-operating conditions (pressure, temperature, and mass flow rates) on combustor stability and pollutant emissions (CO and NO_x) will be quantified. Our existing high-speed simultaneous PIV-PLIF laser diagnostics will be utilized to image unsteady combustion regimes and to provide quantitative measurements for flame structure, velocity fields, and transient flame-base dynamics. All experiments will be conduced in our existing high-pressure gas turbine combustor facility (UM-HPGTCF) that provides realistic operating conditions (20 atm pressure, 750 K combustor inlet temperature, and up to 1 kg/s air mass flow rate).

The objective of the complementary computational research effort consists in the development of a fully validated large-eddy simulation (LES) capability for the accurate prediction of unsteady GT combustion processes, combustor stability margins, and pollutant formation.

By extending our existing LES-modeling techniques, improved subgrid-scale models will be developed for the accurate characterization of autoignition, flashback and flame liftoff, under consideration of detailed HHC-reaction chemistry and turbulence/chemistry interaction. Utilizing this LES-combustion formulation, a complementary modeling effort addresses the characterization of facility-induced nonidealities in flow-reactor experiments. These nonidealities arise from high Reynolds number turbulence transition, mixture stratification, and other mechanisms associated with turbulence/chemistry interaction and localized mixture inhomogeneities. Currently, the underlying physical processes are not fully understood, and their systematic characterization can assist in interpreting experimentally observed irregularities and stochastic autoignition processes in flow-reactor studies. From this knowledge, low-dimensional models and regime diagrams will be developed that can be utilized for chemical-kinetics investigations and for guiding future FR-designs to reduce facility effects.

Chapter 2

Characterization of Facility Effects in Rapid Compression Machines

1 Introduction

With the rapidly growing energy demand and environmental concerns, the utilization of reformed fuels is gaining increasing attention. Specifically, the operation of HHC-fuels in power-generation applications offers enormous potential for significant reductions in greenhouse-gases, particulate matters, and other harmful and corrosive substances. Syngas contains varying amounts of carbon monoxide (CO) and hydrogen (H_2) as main fuel components and other species such as water (H_2O) and carbon dioxide (CO_2). Syngas can be generated from different sources including coal, biomass, organic waste, and refinery residuals [1]. Other advantages of the syngas-technology are its potential for clean utilization of fossil fuel source when combined with carbon-capture and sequestration strategies [2], and the separation of pollutants (sulfur, ammonia, and PM) before combustion [3].

Integrated gasification combined cycle (IGCC) power generation technologies can provide significant improvements in thermal efficiency and dramatic reductions in environmental impact compared to conventional coal-fired power plants. In these and other high-efficiency/low-emission combined cycle power plants, syngas is generated from the partial oxidation of coal with oxygen and steam in high-pressure gasifiers [4, 5]. The subsequent gas turbine cycle utilizes the excess enthalpy of the high-temperature syngas mixture from the gasification process, resulting in a significant increase in overall power plant efficiency.

Although the successful operation of gas turbines using syngas has been demonstrated [6, 7], fundamental scientific and technological challenges must be overcome in order to utilize the full potential of IGCC systems. These challenges are primarily attributed to the low density and higher diffusivity of hydrogen compared to conventional hydrocarbon fuels. Variations in the thermo-diffusive properties of the mixture can lead to significant modifications in flame speed, flammability limits, and other fundamental combustion characteristics [8–10], which can adversely affect combustion stability and fuel conversion. In addition, high flame

temperatures associated with hydrogen combustion make NO_x emissions a concern, and dilution strategies are requires to reduce these emissions to acceptable levels [11].

Currently, the combustor design is further complicated by uncertainties in the syngas combustion kinetics at gas-turbine-relevant operating conditions. These uncertainties are reflected by large discrepancies between chemical kinetics models and experimental data of syngas mixtures at high pressures ($p_0 > 10$ bar) and intermediate temperatures ($T_0 < 1000$ K). To reconcile these observed discrepancies, experimental studies were conducted in rapid compression machines, shock tubes, and flow reactors; revised CO/H_2 reaction mechanisms were developed [1, 3, 12–25], and different hypotheses have been put forward to explain the discrepancies between experiments and predictions, including (i) sensitivity of rate coefficients at high-pressure/low-temperature conditions, (ii) effects of inhomogeneities in mixture composition and flow-field structure on ignition characteristics in experimental facilities, (iii) catalytic effects of syngas mixture due to contaminations with metal carbonyls and nitric oxides, and (iv) the significance of induction chemistry related to compressibility, mixing, and surface-catalytic effects. However, limitations in experimental instrumentation and diagnostics limits the systematic investigation of these hypotheses. Furthermore, the characterization of such facility-induced non-idealities has so far mainly focused on shock tubes and rapid compression machines, and detailed experimental and computational investigations of flow-reactors have not been performed. This is partially attributed to the high-Reynolds number flow regimes in FR (with Reynolds numbers in excess of 2×10^5). To address these issues, in the following a closely coordinate experimental and computation research program will be proposed in order to obtain an improved understanding about critical combustion-physical processes and to enable the successful implementation of HHC-combustion in GT-systems.

The renewed interest in syngas combustion led to numerous experimental studies in order to obtain improved understanding about the combustion-physical properties and reaction chemistry of syngas oxidation under gas-turbine-relevant operating conditions. These experiments are typically conducted in shock tubes (STs), flow reactors (FRs), and rapid compression machines (RCMs), and Refs. [1,3,12,26] provide comprehensive overviews about experimental investigations and measurements for ignition delay time, flame speed, and other combustion-physical properties.

Interestingly, comparisons of ignition delay times between measurements and computations exhibit significant discrepancies [12] that increase with decreasing initial temperature of the syngas/air mixture. To reconcile these discrepancies, different explanations have been proposed, including incomplete reaction mechanisms and uncertainties in rate constants, effects of gas impurities and surface-catalytic processes, wall-heat transfer and large-scale mixing, and drifts in operating conditions. Although some of these mechanisms are particular to specific facilities [27, 28], the disparity of measurements among different facilities would suggest that such secondary processes might also be present at different levels in other facilities, and their potential contributions require careful characterization.

Over recent years, computational and experimental studies have been conducted to characterize the flow field structure and wall heat transfer in RCMs [29–34]. Intrusive and non-

intrusive measurements of temperature and species have been performed to demonstrate the existence of a so-called adiabatic core region. In this adiabatic core region the gas mixture is not directly affected by heat losses and boundary layer effects. The mixture contained in this volume is isentropically compressed, and the combustion of the nominally uniform composition can be approximated as a homogeneous reactor system. In this context it is noted that the existence of this adiabatic core region is fundamental in order to relate rapid compression experiments to zero-dimensional homogeneous ignition studies. Although this volumetric ignition scenario is the prevailing combustion mode in RCMs, deflagrative ignition modes have also been observed experimentally [26, 34, 35]. These front-like ignition modes have been associated with a gradual increase in the pressure trace [35]. Investigations by Elsworth *et al.* [35] and others suggest that these non-uniform ignition processes are initiated at particles that are present in the test gas mixture. They also concluded that deflagration modes become more relevant in hydrogen-containing mixtures, which was attributed to the enhanced sensitivity of these mixtures to impurities.

While experimental investigations mainly focused on the large-scale fluid motion and wall heat transfer effects, the role of turbulence and fluctuations in composition and temperature on the ignition and combustion in RCMs has so far not been appreciated. The objective of this contribution is to address this aspect. To this end, a model is developed that enables the characterization of turbulence fluctuations and variations in mixture composition and temperature during the compression and ignition of the gas mixture.

The potential importance of turbulence in RCMs can be assessed from the Reynolds number Re, which can be estimated as

$$\mathrm{Re} = \frac{l_1^*}{\tau^*}\frac{d^*}{\nu^*} \,, \tag{2.1}$$

where the ratio l_1^*/τ^* is the characteristic speed of the piston, l_1^* is the length of the RCM driven section, τ^* is the compression time, d^* is the diameter of the test section, and ν^* is the kinematic viscosity of the gas mixture at reference condition. Typical Reynolds numbers for RCMs are in the range $\mathrm{Re} \approx \mathcal{O}(10^4 - 10^5)$, suggesting that the compression and subsequent ignition is not unaffected by turbulence. This argument is supported by recent investigations by Guibert *et al.* [34], in which PIV measurements in a RCM-facility were performed. These measurements showed that mean flow fluctuations above 5 m/s can be obtained at the end of the RCM compression phase. This magnitude is in qualitative agreement with turbulence measurements in idealized internal combustion engines [36].

The following sources of turbulence can be identified in RCMs:

- *Filling process:* The filling process of the driven section with the fresh test gas mixture is accompanied by the generation of small-scale turbulence fluctuations that are approximately homogeneously distributed in the entire test section. If the compression phase is initiated directly after the filling process, providing insufficient time for the complete decay, the initially introduced turbulence is amplified during the compression.

- *Corner vortices:* During the compression phase, the piston motion generates corner vortices and large vortical structures. The roll-up of these structures induces flow field perturbations and the entrainment of cold fluid into the core region [30, 37]. Although these corner vortices can be reduced by appropriate piston-crown design [30, 32], their contributions cannot be entirely eliminated.

- *Boundary layer-generated turbulence:* During the compression phase, the piston motion induces a mean flow, which leads to the formation of a boundary layer. At sufficiently high Reynolds numbers, the boundary layer transitions, which is associated with the generation of turbulence. This wall-generated turbulence is subsequently transported into the core region, where it will be further amplified through the mean strain interaction.

- *Turbulence production by compressive strain:* During the compression phase, the rapid piston motion induces a time-dependent strain rate, leading to enhanced turbulence production. This nonequilibrium process is dependent on the strain-rate profile, and is a main mechanism for the turbulence amplification at the end of the compression phase.

Although the relative contributions of these mechanisms have so far not been experimentally quantified and are most-likely dependent on facility design and operating conditions, theoretical investigations suggest that the mean-strain amplification is a main process for the turbulence-generation in piston compression machines [38–40].

In order to quantify the turbulence at the end of the RCM-compression phase, rapid distortion theory is utilized to model the turbulence amplification by the piston-induced mean-strain. Sources of turbulence that arise from the filling process, boundary-layer, and vortical roll-up are hereby considered as feeding mechanisms to this mean-strain amplification, and are in the following parametrically represented in terms of an initial turbulence level, which is denoted by $\mathcal{T}_u$.

Following the compression phase, the ignition of the test gas mixture is modeled by considering the distribution of thermal and mixture inhomogeneities, which interact among each other through turbulent mixing and diffusion. To this end, a Lagrangian Fokker-Planck (LFP) model is derived, and closure is obtained using a k–ε formulation and an IEM ("interaction by exchange with the mean") micromixing model. The particular advantage of this model is that this LFP formulation reduces to the well-known homogeneous reactor model in the absence of turbulence and mixture inhomogeneities.

2 Mathematical Model

In the following, a mathematical model is developed to describe the compression and subsequent combustion process in a rapid compression machine. This model development is

guided by the interest in developing a low-order model that enables the identification of important process parameters and their effects on the ignition and combustion process in RCM-facilities. To this end, the RCM is modeled as a one-dimensional system and geometric variations due to contractions in the driven section are not considered. Such converging sections are utilized by different groups [34, 41] to connect the driven and the test-gas regions. While such contractions are beneficial in preventing the boundary layer from entering the test-gas section, they locally enhance the strain and promote flow separation.

The schematic of the RCM is illustrated in Fig. 2.1, consisting of a driver section and a driven section; both sections are separated by a freely moving piston with mass m^*. A coordinate system x_1^* is introduced, and the location of the piston with respect to the coordinate origin is denoted by x_P^*. Conditions in the driven and the driver sections are denoted by subscripts "1" and "2," respectively, and all dimensional quantities are indicated by an asterisk.

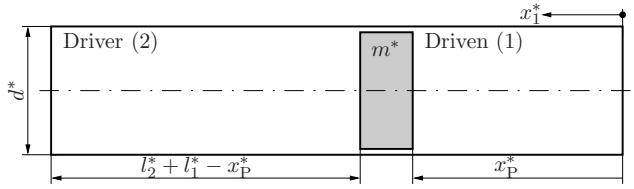

Figure 2.1: Schematic of rapid compression machine. During the compression phase, the piston (gray) compresses the gas mixture in the driven section. The location of the piston is denoted by x_P^*; mass of the piston is m^*, and initial length of the driver section is l_2^*. The diameter of the RCM is denoted by d^*.

To describe the kinematics of the RCM during the compression phase, the following reference quantities are identified:

$$\begin{aligned} \text{Length scale:} \qquad & l_1^* = x_\mathrm{P}^*(t^* = 0) \,, \\ \text{Time scale:} \qquad & \tau^* = \sqrt{\frac{m^* l_1^*}{\Delta p^* A^*}} \,, \\ \text{Pressure difference:} \qquad & \Delta p^* = p_2^*(t^* = 0) - p_1^*(t^* = 0) \,, \end{aligned}$$

where p^* is the pressure and A^* is the constant piston area. With these reference properties, the following non-dimensional quantities can be defined:

$$t = \frac{t^* - t_\mathrm{C}^*}{\tau^*} \,, \quad x_\mathrm{P} = \frac{x_\mathrm{P}^*}{l_1^*} \,, \quad \ell = \frac{l_2^*}{l_1^*} \,,$$
$$c = \frac{\tau^* c^*}{m^*} \,, \qquad p = \frac{p^*}{\Delta p^*} \,,$$

where c^* is the friction coefficient, t^* is the time, and t_C^* corresponds to the duration of the

compression phase, which can be evaluated as

$$x_{\mathrm{P}}(0) = \int_{-t_{\mathrm{C}}}^{0} \dot{x}_{\mathrm{P}}(t')\mathrm{d}t' + 1\,. \tag{2.2}$$

In this equation, $\dot{x}_{\mathrm{P}}$ is the piston speed and $t_{\mathrm{C}} = t_{\mathrm{C}}^*/\tau^*$.

The mathematical model consists of three components, describing

(i) the kinematics of the piston motion during the compression phase,

(ii) the amplification of the turbulence and compositional fluctuations by piston-induced mean-strain, and

(iii) the subsequent ignition of the test gas mixture under consideration of turbulence/chemistry interaction, wall-heat-loss effects, and detailed reaction chemistry.

These individual modeling components are discussed in the following sections.

2.1 Piston Motion

The motion of the piston can be described by a second-order ordinary differential equation for a mass-spring-damping system. This equation is derived by applying a force balance on the freely moving piston:

$$\ddot{x}_{\mathrm{P}} + p_{2,\mathrm{s}} \left(\frac{\ell + 1 - x_{\mathrm{P}}}{\ell} \right)^{-\gamma} - p_{1,\mathrm{s}} x_{\mathrm{P}}^{-\gamma} + c\dot{x}_{\mathrm{P}} = 0\,. \tag{2.3}$$

The subscript "s" denotes the initial state at the beginning of the compression phase. The second and third term represent the pressure force acting on the piston, and the last term on the left-hand-side corresponds to the friction force. The pressure evolution in the driver and driven sections are derived from the isentropic state relation, in which the ratio of specific heats, γ, is assumed to be constant during the compression phase. This is accurate within $\pm 10\,\%$ for the species compositions and conditions considered here.

2.2 Flow Field Evolution during Compression Phase

The flow field in the driven section is characterized by the conservation equations for mass, momentum, species, and temperature, together with the ideal gas law. Using the references quantities $l_1^*, \tau^*, \Delta p^*, m^*$, and A^*, the governing equations can be written in non-dimensional

form as [42]:

$$\mathcal{D}_t\rho = -\rho\nabla\cdot\boldsymbol{u}\,, \tag{2.4a}$$

$$\rho\mathcal{D}_t\boldsymbol{u} = -\nabla p + \frac{1}{\mathrm{Re}}\nabla\cdot\underline{\underline{\sigma}}\,, \tag{2.4b}$$

$$\rho\mathcal{D}_t\boldsymbol{Y} = \frac{1}{\mathrm{Re}\,\mathrm{Sc}}\nabla\cdot(\rho\upsilon\nabla\boldsymbol{Y}) + \rho\dot{\boldsymbol{\omega}}\,, \tag{2.4c}$$

$$\rho c_p\mathcal{D}_t T = \mathrm{Ec}\,\mathcal{D}_t p + \frac{\mathrm{Le}}{\mathrm{Re}\,\mathrm{Sc}}\nabla\cdot(\lambda\nabla T) + \frac{1}{\mathrm{Re}\,\mathrm{Sc}}\left(\rho\upsilon\sum_i c_{p,i}\nabla Y_i\right)\nabla T + \frac{\mathrm{Ec}}{\mathrm{Re}}\underline{\underline{\sigma}} : \nabla\boldsymbol{u} + \rho\dot{\omega}_T\,, \tag{2.4d}$$

$$p = \frac{1}{\mathrm{Ec}}\rho R T\,, \tag{2.4e}$$

where ρ is the density, $\boldsymbol{u}$ is the velocity vector, $\underline{\underline{\sigma}}$ is the viscous stress tensor, υ is the diffusivity, and $\mathcal{D}_t = \partial_t + \boldsymbol{u}\cdot\nabla$ is the substantial derivative. The Reynolds number Re is defined in Eq. (2.1), the Schmidt number is $\mathrm{Sc} = \nu^*/\upsilon^*$, the Lewis number is $\mathrm{Le} = \lambda^*/(\rho^* c_p^* \upsilon^*)$, and $\mathrm{Ec} = (l_1^*/\tau^*)^2(c_p^* T^*)^{-1}$ is the Eckert number. The vector of species mass fractions and the corresponding production rates are denoted by $\boldsymbol{Y}$ and $\dot{\boldsymbol{\omega}}$, respectively; T is the non-dimensional temperature and $\dot{\omega}_T$ is the non-dimensional heat release rate.

2.2.1 Mean Flow

Velocity, species mass fractions, and temperature are decomposed into a mean and a fluctuating quantity following the ensemble averaging procedure, *viz.* $\phi = \overline{\phi} + \phi'$. Since the Mach number is small, fluctuations in density can be neglected. It is assumed that the thermodynamic properties are not affected by variations in the composition. Furthermore, all viscous-diffusive properties are assumed to be constant during the compression phase. Under the assumption that the flow-field in the driven section is uni-directional, the mean velocity can be evaluated from the mean continuity equation and piston motion as

$$\overline{u}_1 = \alpha(t)x_1 \qquad \text{with} \qquad \alpha(t) = \frac{\dot{x}_\mathrm{P}(t)}{x_\mathrm{P}(t)}\,, \tag{2.5}$$

where α is the time-dependent mean strain rate. The evolution of the mean mixture composition and temperature during the compression phase can be derived from Eqs. (2.4c) and (2.5):

$$\overline{\boldsymbol{Y}} = \langle\boldsymbol{Y}\rangle + \boldsymbol{\beta}(t)\left(x_1 - \frac{x_\mathrm{P}(t)}{2}\right) \qquad \text{with} \qquad \boldsymbol{\beta}(t) = \boldsymbol{\beta}_\mathrm{s}\xi(t)\,, \tag{2.6}$$

where $\langle\cdot\rangle$ corresponds to a volume-averaged quantity, $\boldsymbol{\beta}_\mathrm{s}$ denotes the stratification of the species composition at the beginning of the compression, and the compression ratio $\xi(t)$ is

evaluated as [43]:

$$\xi(t) = \exp\left\{-\int_{-t_C}^{t} \alpha(t')\mathrm{d}t'\right\} = \frac{1}{x_P(t)} \,. \tag{2.7}$$

The temporal evolution of the mean pressure and temperature during the RCM compression phase are evaluated from the isentropic state relations:

$$\langle T\rangle(t) = \langle T_s\rangle \xi(t)^{\gamma-1} \,, \tag{2.8}$$

$$\langle p\rangle(t) = \langle p_s\rangle \xi(t)^{\gamma} \,. \tag{2.9}$$

The mean flow solution is then used to evaluate the amplification of turbulence and compositional fluctuations during the compression phase. For this, the rapid distortion theory is employed, and the derivation is discussed in the next section.

2.2.2 Turbulent Flow Field

Amplifications of turbulence and fluctuations in mixture composition are described using rapid distortion theory (RDT). RDT describes the evolution of initially homogeneous turbulence when it is subjected to rapid strain [43–45]. Specifically, RDT assumes that the evolution of the turbulence is controlled by the mean flow, and only weakly interacts with itself during the time over which the mean strain is applied. This can be characterized by the criterion

$$\frac{1}{\alpha}\frac{u_s'}{l_m} \ll 1 \,, \tag{2.10}$$

where α is the characteristic mean strain rate (defined in Eq. (2.5)) and l_m/u_s' is the eddy lifetime. Under these conditions, the non-linear terms in the fluctuating conservation equations can be neglected, and the resulting linearized equations can be written in index notation as

$$\partial_i u_i' = 0 \,, \tag{2.11a}$$

$$\partial_t u_i' + \alpha x_1 \partial_1 u_i' + \alpha u_1' \delta_{1i} = -\frac{1}{\bar{\rho}}\partial_i p' \,, \tag{2.11b}$$

$$\partial_t \boldsymbol{Y}' + \alpha x_1 \partial_1 \boldsymbol{Y}' + u_1' \boldsymbol{\beta} = 0 \,, \tag{2.11c}$$

$$\partial_t T' + \alpha x_1 \partial_1 T' = -(\gamma-1)\alpha T' \,. \tag{2.11d}$$

Note that all viscous-diffusive contributions are neglected in deriving Eqs. (2.11), since they will only add an exponentially decaying coefficient in the RDT-formulation that is small compared to the strain-induced amplification rate. The temporal evolution of the normal stresses and variance of species mass fractions and temperature is given by the following

equations:

$$\frac{\langle u_1'^2\rangle}{\mathcal{T}_u^2} = \frac{3}{8\pi}\xi^2 \iint \frac{e_2^2+e_3^2}{(e_1^2\xi^2+e_2^2+e_3^2)^2}\sin\theta \mathrm{d}\theta\mathrm{d}\phi \;, \tag{2.12a}$$

$$\frac{\langle u_\alpha'^2\rangle}{\mathcal{T}_u^2} = \frac{3}{8\pi}\iint \left\{ \frac{e_\alpha^2 e_1^2(1-\xi^2)}{(e_1^2\xi^2+e_2^2+e_3^2)^2}\times \left[\frac{(1-\xi^2)(1-e_1^2)}{e_1^2\xi^2+e_2^2+e_3^2}-2\right]+(1-e_\alpha^2)\right\}\sin\theta\mathrm{d}\theta\mathrm{d}\phi \;, \quad \text{for } \alpha=\{2,3\} \tag{2.12b}$$

$$\frac{\langle \boldsymbol{Y}'^2\rangle}{\mathcal{T}_{\boldsymbol{Y}}^2} = \frac{3}{8\pi}\frac{\mathcal{T}_u^2}{\mathcal{T}_{\boldsymbol{Y}}^2}\boldsymbol{\beta}_\mathrm{s}^2 \iint J^2(e_2^2+e_3^2)\sin\theta\mathrm{d}\theta\mathrm{d}\phi + 1 \;, \tag{2.12c}$$

$$\frac{\langle T'^2\rangle}{\mathcal{T}_T^2} = \xi^{2(\gamma-1)} \;, \tag{2.12d}$$

where θ is the polar angle with $\theta \in [0,\pi]$, ϕ is the azimuthal angle with $\phi \in [0,2\pi]$, $\boldsymbol{e} = (\cos\theta, \sin\theta\cos\phi, \sin\theta\sin\phi)^T$ is the time-dependent unit wave number vector in spherical coordinates, and the term

$$J = \int_{-t_\mathrm{C}}^{0} \frac{\xi^2}{e_1^2\xi^2+e_2^2+e_3^2}\mathrm{d}t' \tag{2.13}$$

introduces a memory effect in Eq. (2.12c).

Equations (2.12) show that the amplification of the turbulence, scalar- and temperature-fluctuations during the RCM compression phase are directly dependent on turbulence intensity $\mathcal{T}_u$, scalar fluctuations $\mathcal{T}_{\boldsymbol{Y}}$, temperature fluctuation $\mathcal{T}_T$, mixture stratification $\boldsymbol{\beta}_\mathrm{s}$, and the compression ratio ξ. The parameters $\mathcal{T}_u$, $\mathcal{T}_{\boldsymbol{Y}}$, and $\mathcal{T}_T$ are defined as

$$\mathcal{T}_u = u_\mathrm{s}'\left(=u_\mathrm{s}^{*\prime}\frac{\tau^*}{l_1^*}\right) \;, \quad \mathcal{T}_{\boldsymbol{Y}} = \boldsymbol{Y}_\mathrm{s}'\left(=\sqrt{\boldsymbol{Y}_\mathrm{s}^{*\prime 2}}\right) \;, \quad \mathcal{T}_T = T'\left(=\frac{T^{*\prime}}{T^*}\right) \;. \tag{2.14}$$

2.3 Ignition and Combustion Phase

Following the compression phase, it is assumed that the combustion of the test gas mixture occurs through autoignition. The temporal evolution of the mixture is described by a Lagrangian Fokker-Planck model. This is a particle method and accounts for the interaction between turbulence, scalar mixing, and wall heat transfer.

In the absence of a mean flow, the decay of the homogeneous turbulence during the combustion phase is described by the evolution equations for the turbulent kinetic energy $\langle k\rangle = \frac{1}{2}\langle u_i'^2\rangle$ and dissipation rate $\langle\varepsilon\rangle$

$$\mathrm{d}_t\langle k\rangle = -\langle\varepsilon\rangle \;, \tag{2.15a}$$

$$\mathrm{d}_t\langle\varepsilon\rangle = -C_{\varepsilon,2}\frac{\langle\varepsilon\rangle}{\tau_\mathrm{t}} \qquad \text{with} \qquad \tau_\mathrm{t} = \frac{\langle k\rangle}{\langle\varepsilon\rangle} \;, \tag{2.15b}$$

where $C_{\varepsilon,2}$ is a constant, and τ_t is the eddy life-time. The solution to Eqs. (2.15) can be described by a power-law decay as [43]

$$\langle k\rangle = \langle k\rangle_0 \left(\frac{t}{\tau_0}+1\right)^{-n} , \qquad \langle \varepsilon\rangle = \langle \varepsilon\rangle_0 \left(\frac{t}{\tau_0}+1\right)^{-(n+1)} , \tag{2.16}$$

and the subscript "0" denotes the condition at $t = 0$, corresponding to the end of the compression phase, and $\tau_0 = n\langle k\rangle_0/\langle\varepsilon\rangle_0$. Using standard k–ε closure modeling, τ_0 and τ_t can be expressed as

$$\tau_0 = \frac{n}{C_D} l_m \langle k\rangle_0^{-1/2} , \tag{2.17a}$$

$$\tau_\mathrm{t} = \frac{1}{n}(t+\tau_0) , \tag{2.17b}$$

where $\langle\varepsilon\rangle_0 = C_D\langle k\rangle_0^{3/2} l_m^{-1}$ was used [43,46]; n and C_D are constants, and l_m is a characteristic mixing length. These parameters are specified in Sec. 3.

The temporal evolution of the mixture is obtained from the solution of the LFP-model, which can be written as [47]:

$$\mathrm{d}\boldsymbol{\psi} = \dot{\boldsymbol{\omega}}\mathrm{d}t - \boldsymbol{a}(\boldsymbol{\psi})\mathrm{d}t + \boldsymbol{b}(\boldsymbol{\psi})\mathrm{d}W(t) , \tag{2.18}$$

where $\boldsymbol{\psi} = (\boldsymbol{Y}, T)^T$ denotes the vector of the species mass fractions and temperature, and $\dot{\boldsymbol{\omega}}$ is the corresponding source term. The second term on the right-hand-side of Eq. (2.18) is the drift term, accounting for the interaction and micromixing among the ignition kernels. The last term is the diffusion term, and W denotes a Wiener process. It can be seen that in the limit of $\boldsymbol{a} \to 0$ and $\boldsymbol{b} \to 0$ the well-known homogeneous reactor model is recovered. As such, Eq. (2.18) can be considered as a first-order extension to the constant-volume homogeneous combustion problem.

The drift-term in Eq. (2.18) is modeled using the "interaction by exchange with the mean (IEM)" model [47], which is given as:

$$\boldsymbol{a} = \underline{\underline{A}} \begin{pmatrix} \boldsymbol{Y} - \langle \boldsymbol{Y}\rangle \\ T - \langle T_\downarrow\rangle \end{pmatrix} \quad \text{and} \quad \underline{\underline{A}} = \mathrm{diag}\left(\boldsymbol{\tau}_{\boldsymbol{Y}}, (\tau_T + \tau_\downarrow)\right)^{-1} . \tag{2.19}$$

By introducing the time scale ratios [48] $C_Z = \tau_\mathrm{t}/\tau_Z$, $C_Y = \tau_Y/\tau_Z$, $C_T = \tau_T/\tau_Z$, and τ_t from Eq. (2.17b), $\underline{\underline{A}}$ can be written as

$$\underline{\underline{A}} = \frac{C_Z}{C_Y}\frac{n}{(t+\tau_0)} \begin{pmatrix} \underline{\underline{I}} & 0 \\ 0 & \frac{C_Y}{C_T}\left(1 + \tau_\downarrow \frac{C_Z}{C_T}\frac{n}{(t+\tau_0)}\right)^{-1} \end{pmatrix} , \tag{2.20}$$

where $\underline{\underline{I}}$ is the identity matrix, and C_Z, C_Y, and C_T are constants of order unity (specified in Tab. 2.1). Wall-heat-loss effects are incorporated in Eq. (2.19) through an adiabatic expansion

model [49] by introducing the non-adiabatic core temperature $\langle T_\downarrow \rangle$ and the thermal diffusion time scale $\tau_\downarrow$ in Eq. (2.19). Details on the model formulation are presented in Sec. 2.4.

The term $\boldsymbol{b}$ in Eq. (2.18) enforces that the diffusion process is constrained to the accessible state-space. This term is modeled as

$$\boldsymbol{b}^2(\boldsymbol{\psi}) = \underline{\underline{A}} \begin{pmatrix} \langle \boldsymbol{\psi}'^2 \rangle f(\boldsymbol{\psi}) \\ \langle T'^2 \rangle f(T) \end{pmatrix} \tag{2.21}$$

with the shape function [47]

$$f(\psi) = \frac{(\psi - \psi^-)(\psi^+ - \psi)}{\langle (\psi - \psi^-)(\psi^+ - \psi) \rangle} , \tag{2.22}$$

and $\psi^\pm$ denotes the minimum and maximum value of a quantity ψ in the composition vector.

2.4 Consideration of Wall-Heat-Loss Effects

Effects of heat losses on the gas mixture during the ignition and combustion phase are accounted for in Eq. (2.18) through the non-adiabatic core temperature $\langle T_\downarrow \rangle$. The calculation of this quantity follows the volume-expansion model of Tanaka *et al.* [49]. In the present formulation $\langle T_\downarrow \rangle$ is obtained from the solution of the temperature equation, Eq. (2.4d), in which heat-flux contributions due the species diffusion and density gradients are neglected. The temperature profile in the boundary layer can then be obtained from the solution of the energy equation, which is here written in polar coordinates as:

$$\partial_t \Theta = (1 - \Theta) \mathrm{d}_t \ln(\langle T \rangle - T_\mathrm{W}) + \frac{\mathrm{Le}}{\mathrm{Re}\,\mathrm{Sc}} \frac{1}{r} \partial_r (r \upsilon \partial_r \Theta) , \tag{2.23}$$

where r is the radius, T_W is the wall temperature, $\langle T \rangle$ is obtained from the LFP solution, and Θ is the normalized temperature, which is defined as

$$\Theta = \frac{T - T_\mathrm{W}}{\langle T \rangle - T_\mathrm{W}} . \tag{2.24}$$

The boundary conditions for Eq. (2.23) are:

$$\text{Adiabatic core region:} \qquad \partial_r \Theta|_{r=0} = 0 , \tag{2.25}$$

$$\text{Isothermal wall:} \qquad \Theta|_{r=d/2} = 0 . \tag{2.26}$$

With the time-dependent solution of Eq. (2.23), the non-adiabatic core temperature can then be computed as

$$\langle T_\downarrow \rangle = (\langle T \rangle - T_\mathrm{W}) \frac{8}{d^2} \int_0^{d/2} \Theta r \mathrm{d}r + T_\mathrm{W} . \tag{2.27}$$

The displacement thickness of the thermal boundary layer is

$$\delta_\downarrow = \int_0^{d/2} (1 - \Theta) \mathrm{d}r , \tag{2.28}$$

so that the thermal diffusion time scale can then be evaluated as $\tau_\downarrow = \delta_\downarrow^2 / \upsilon$.

n	C_D	C_Z	C_T	C_Y	l_m
1.3	0.1664	2.0	1.0	1.0	0.0259

Table 2.1: Model constants for RCM-model.

3 Specification of Model Configuration

The compression-ignition model, that was developed in the previous sections, is applied to the free-piston RCM at the University of Michigan [41]. The UM-RCM facility consists of a pressurized driver section having a length of 5.54 m and an inner diameter of 154 mm. The driven section, containing the test gas mixture, is separated from the driver section through a freely moving piston. The driven section is 2.54 m long and has an inner diameter of 101.2 mm. The end of the driven section is connected to the test section with an inner diameter of 50.8 mm and a length of 50.6 mm. In the following, the geometry of the UM-RCM facility is modeled as cylinder having a constant diameter, and the dimensions are corrected to reproduce the geometric compression ratio of the facility. The length of the driven section, including the test section, is $l_1^* = 2970$ mm, the length of the test section is 77 mm, resulting in a compression ratio of $\xi = 38.6$. The diameter of all sections is kept constant and equal to that of the UM-RCM with 101.2 mm. The mass of the piston is $m^* = 2.575$ kg, the pressure in the driver section is $p_{2,\mathrm{s}}^* = 2.0735$ bar, and friction is neglected. The initial pressure in the driven section is $p_{1,\mathrm{s}}^* = 0.097$ bar and the ratio of specific heats is $\gamma = 1.3$. Note that the cross-section area and the mass of the piston only affect the reference time scale τ^*, which is evaluated to be $\tau^* = 69.36$ ms.

The test gas in the driven section consists of a fuel-lean syngas/air mixture. Different syngas mixtures, with the composition:

$$\phi(\nu_{\mathrm{H_2}}\mathrm{H_2} + \mathrm{CO}) + \nu_{\mathrm{CO_2}}\mathrm{CO_2} + \nu_{\mathrm{O_2}}\mathrm{O_2} + \nu_{\mathrm{N_2}}\mathrm{N_2} \tag{2.29}$$

are considered. In this equation, ν_i is the stoichiometric coefficient of species i; ϕ is the equivalence ratio, which can be expressed in terms of the mixture fraction Z and its stoichiometric value Z_{st} [48]:

$$\phi = \frac{Z}{Z_{\mathrm{st}}} \frac{1 - Z_{\mathrm{st}}}{1 - Z} \ . \tag{2.30}$$

The chemical mechanism by Li *et al.* [50] is used to describe the syngas combustion, and all model constants used in the LFP model are summarized in Tab. 2.1.

4 Results

4.1 RCM Compression Phase

The temporal evolution of piston location, piston velocity, and mean strain rate are illustrated in Fig. 2.2. Note that the time and all other quantities are non-dimensionalized, and $t = 0$ corresponds to the end of the compression phase. From this figure, it can be seen that the piston exhibits an approximately constant acceleration up to $t = -0.35$, after which the piston decelerates due to the compression of the test gas mixture in the driven section.

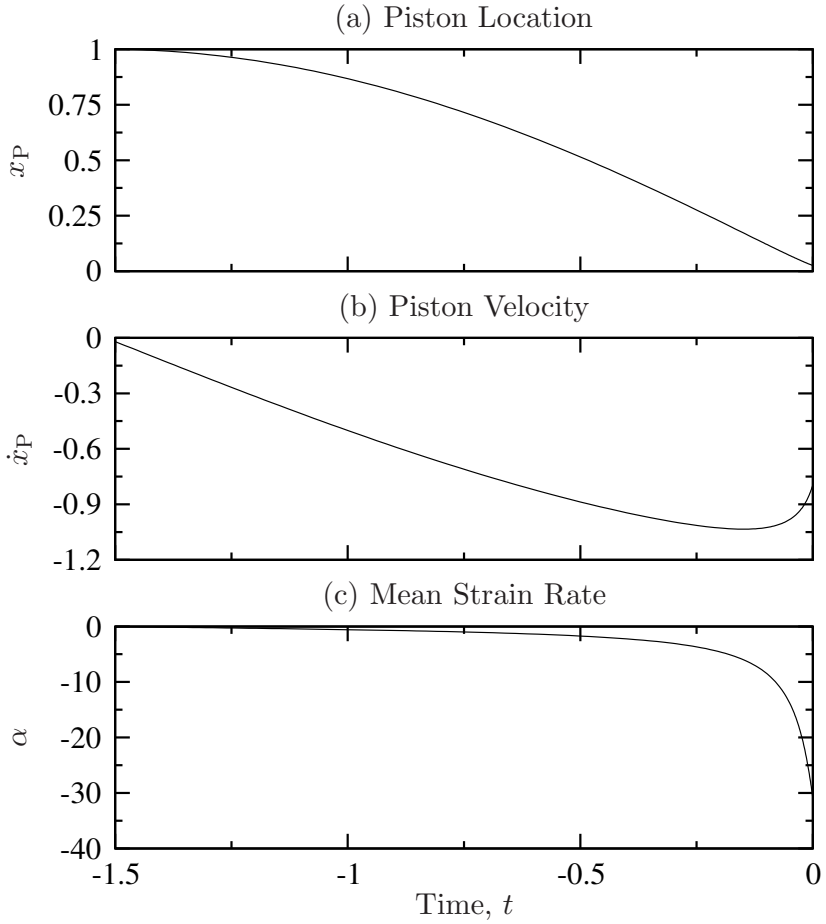

Figure 2.2: Kinematics of the RCM-facility during the compression phase, showing (a) the piston location x_P, (b) the piston velocity $\dot{x}_P$, and (c) the mean strain rate $\alpha = \dot{x}_P/x_P$.

The mean strain rate, shown in Fig. 2.2(c), remains small up to $t = -0.35$. However, beyond this point α rapidly increases in magnitude until it reaches a value of -39.5 at the end of the compression phase.

4.1.1 Turbulence Amplification during Compression Phase

The temporal evolution of the turbulence and compositional fluctuations during the RCM compression phase are shown in Fig. 2.3. From this figure, it can be seen that all turbulent quantities remain approximately constant and equal to their initial values up to $t = -0.35$. Beyond this point a nearly exponential increase in the turbulence quantities is observable, which is associated with the rapid increase in the strain rate (see Fig. 2.2(c)). Physically, the turbulence amplification can be understood as result of the mean-flow induced distortion of turbulent eddies and the corresponding increase in Reynolds stresses [45].

The evolution of the scalar variance for different values of mixture stratification is shown in Fig. 2.3(b). Since $\langle Y'^2 \rangle$ has a quadratic dependence on β_s (see Eq. (2.12c)), scalar fluctuations are amplified due to the mean stratification. Although not further considered in the present work, it is noted that such mean stratification effects could become of potential importance when an internal mixture preparation is facilitated.

Since RCM-facilities employ different compression ratios, we will next investigate how the compression ratio affects the turbulence production during the compression phase. For this, additional calculations are performed in which the compression ratio is extended up to $\xi = 100$. Results of this analysis are presented in Fig. 2.4; for reference, the gray area in this figure indicates the typical range of RCM compression ratios. Figure 2.4(a) shows the dependence of the normal stresses and the turbulent kinetic energy as function of compression ratio. Note that the turbulence level in the driven section is only a function of the turbulence level $\mathcal{T}_u$ and the current compression ratio, but – unlike the scalar fluctuations – is not affected by the temporal evolution of the compression phase. Following an initial transition, all normal stress components are linearly dependent on the compression ratio. Due to the rapid straining, the initially isotropic turbulence field transitions to anisotropy, in which the $\langle u_1'^2 \rangle$-component is growing fastest and exceeding the other components by a factor of two.

The results from this RDT analysis are particularly interesting, since they reveal the sensitivity of the turbulence level at the end of the RCM-compression phase to the mean-strain amplification. Specifically, Fig. 2.4 shows that for RCM-facilities with compression ratios as high as 40 the turbulence is amplified by as much as a factor of 50. The reader is reminded that in this work different turbulence contributions are parametrically represented in terms of an initial turbulence level. Despite this simplification, these results indicate that the piston-induced mean-strain is a relevant mechanism in enhancing the fluctuations in the test gas mixture at the end of the compression phase. In conjunction with Fig. 2.3 it can also be conjectured that turbulence-generating mechanisms that evolve throughout the compression phase (such as wall-generated turbulence and the formation of corner vortices) will also be affected by the compressive strain, which is mainly prevailing during the later stage of the compression phase.

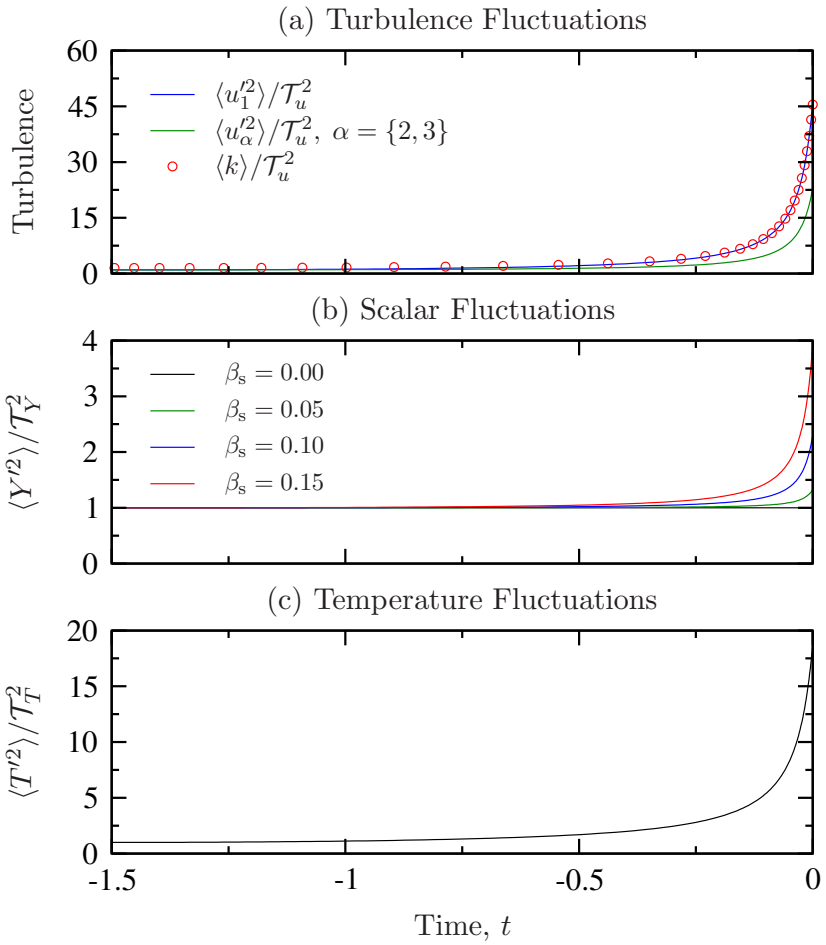

Figure 2.3: Temporal evolution of (a) turbulence and fluctuations in (b) composition and (c) temperature during the RCM-compression phase.

4.1.2 Effects of Temperature Fluctuations and Wall Heat Losses

The objective of this section is to analyze the coupling between turbulence, temperature fluctuations, and wall heat losses in the absence of compositional variations of the test-gas mixture. Recently, Mittal & Sung performed acetone-PLIF measurements to characterize the temperature field in a RCM-facility. They reported root-mean-square (rms) temperature fluctuations around 25 K and measured instantaneous peak temperature fluctuations as large as 100 K after compression for a RCM with a geometric compression ratio of 15.1 [32]. These temperature inhomogeneities are generated by the mixing between fluid in the colder boundary layer and the test gas mixture in the core region during the compression. In the present formulation, these multidimensional mixing processes are not explicitly modeled, so that temperature fluctuations at the end of the compression phase are directly represented through

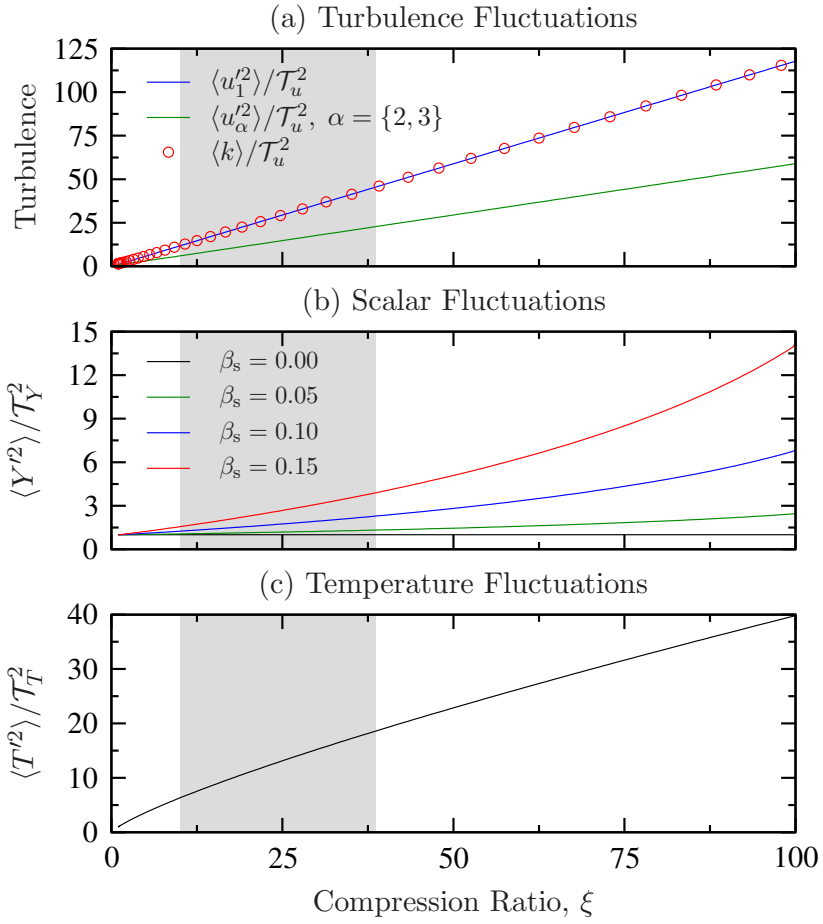

Figure 2.4: Amplification of turbulence quantities as function of compression ratio, showing (a) turbulent normal stresses and turbulent kinetic energy, (b) amplification of the scalar variance for different values of initial mixture stratification, and (c) amplification of temperature variance. The region in gray illustrates the typical range of RCM compression ratios.

the parameter $\mathcal{T}_T$ and the mean compression temperature $\langle T^* \rangle$. Therefore, Eq. (2.12d) is not solved, and the reader should associate $\mathcal{T}_T$ with the temperature perturbations at the beginning of the ignition phase.

To quantify the role of temperature perturbations on the ignition dynamics, the mixture composition is kept constant, and the temperature of all particles is initialized from a Gaussian distribution with mean $\langle T^* \rangle$ and variance $(\mathcal{T}_T \langle T^* \rangle)^2$.

Simulation results for different levels of initial temperature fluctuations, $\mathcal{T}_T$, are presented in Fig. 2.5. For these calculations, the initial turbulence level is kept constant with $\mathcal{T}_u = 0.1$. The mixture composition is $H_2/O_2/CO_2/O_2/N_2 = 7.33/9.71/1.98/17.01/63.97$ with $\phi = 0.5$, and pressure and temperature at the end of the compression phase are $\langle p^* \rangle = 20$ bar and $\langle T^* \rangle = 850$ K. The wall temperature is set equal to 90 percent of the mean temperature at

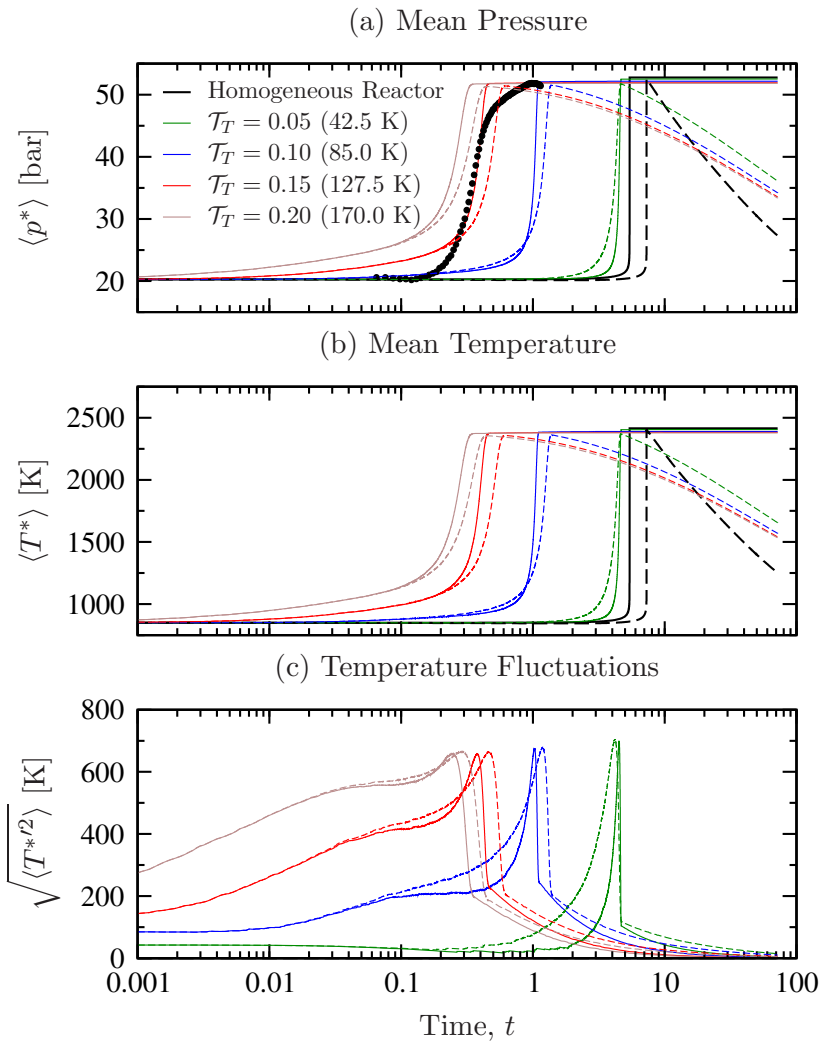

Figure 2.5: Evolution of (a) mean pressure, (b) mean temperature, and (c) temperature fluctuations for different values of temperature perturbations $\mathcal{T}_T$ and fixed turbulence level of $\mathcal{T}_u = 0.1$; corresponding temperature fluctuations at the end of the compression phase are given in parentheses. The mixture composition is $H_2/O_2/CO_2/O_2/N_2 = 7.33/9.71/1.98/17.01/63.97$ and $\phi = 0.5$; pressure and temperature at the end of the compression phase are $\langle p^* \rangle = 20$ bar and $\langle T^* \rangle = 850$ K, respectively. Solid lines correspond to adiabatic results and dashed lines show results with wall heat losses. Pressure-corrected measurements for the same mixture composition are shown by closed symbols [26].

the end of the compression phase. Solid lines indicate adiabatic results, and non-adiabatic simulations are shown by dashed lines.

The results show that the initial temperature fluctuations have a direct effect on the onset of the ignition, and with increasing levels of $\mathcal{T}_T$ the ignition time reduces. It can also be seen that the slope of the pressure and temperature traces decrease with increasing levels of initial

temperature fluctuation. This is in qualitative agreement with experimental results which are included for comparisons in Fig. 2.5(a).

Comparisons between adiabatic and non-adiabatic simulations show that for these operating conditions wall heat losses are secondary in affecting the onset of ignition. While wall heat losses typically lead to a delay in τ_{ig}, it is interesting to point out that non-adiabatic conditions can also have an opposite effect, as evident for the case with $\mathcal{T}_T = 0.05$ (see green lines in Fig. 2.5). For this condition the heat loss favors a slightly earlier ignition which is opposite to the homogeneous reactor simulation and configurations with higher turbulence levels.

The evolution of the rms temperature is presented in Fig. 2.5(c), showing that the location of the peak temperature fluctuation directly correlates with the ignition delay time, which is commonly associated with the location of the steepest pressure slope:

$$\tau_{\mathrm{ig}} = \{t | d_t \langle p_1^* \rangle (t) \rightarrow \max\} \ . \tag{2.31}$$

Beyond this ignition point the temperature fluctuations rapidly decay and the products reach a uniform composition.

Since in the present model the ignition process is controlled by the turbulence evolution, we will next analyze effects of different turbulence levels on the ignition dynamics of the mixture. To this end, simulations are performed for increasing levels of turbulence and keeping the temperature fluctuations constant with $\mathcal{T}_T = 0.1$. Results of this parametric study are illustrated in Fig. 2.6. It can be seen that very low turbulence levels lead to extended ignition processes, which is reflected by large temperature fluctuations. The reduced turbulence level $\mathcal{T}_u$ increases the turbulence time scale τ_0 ($\tau_0 \propto \mathcal{T}_u^{-1}$, see Eq. (2.17a)), resulting in a suppressed micromixing, so that individual ignition kernels evolve in isolation without significant interaction with their respective environments. With increasing turbulence levels, the heat transfer from hot to cold ignition kernels is enhanced resulting in faster ignition of the entire mixture. Note that for the conditions considered here, the heat release exceeds the heat loss by turbulent mixing so that quenching is not relevant.

By considering both parametric dependencies, the ignition delay time as function of $\mathcal{T}_u$ and $\mathcal{T}_T$ can be evaluated. This is illustrated in Fig. 2.7, showing the ratio of the ignition delay times between LFP-model and homogeneous reactor solution, $\tau_{\mathrm{ig}}/\tau_{\mathrm{ig}}^{\mathrm{HR}}$. The results of this parametric study show that – in the absence of compositional inhomogeneities – initial perturbations in temperature have a direct effect on reducing the ignition delay, irrespectively of adiabatic or non-adiabatic operating conditions; wall heat loss only lead to a shift to lower values of $\mathcal{T}_T$. From Fig. 2.7 is can also be seen that for low values of $\mathcal{T}_T$ the turbulence can either reduce or increase the ignition delay. This can be attributed to the interaction between turbulence and chemistry, and will be further discussed in the context of a Damköhler analysis in Sec. 4.1.4.

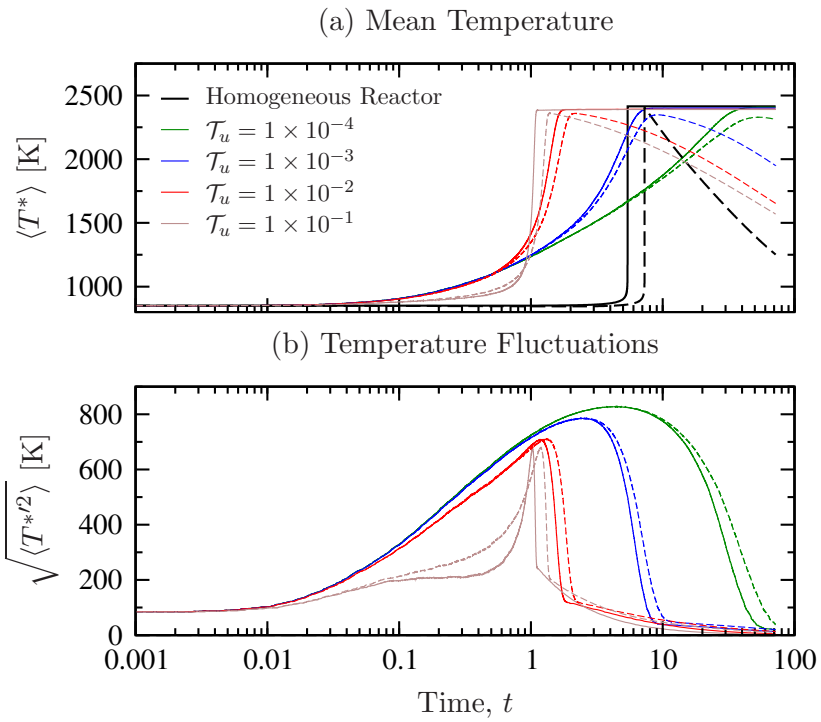

Figure 2.6: Evolution of (a) mean temperature and (b) temperature fluctuations for different levels of turbulence $\mathcal{T}_u$ and fixed temperature perturbation of $\mathcal{T}_T = 0.1$. The mixture composition is $H_2/O_2/CO_2/O_2/N_2 = 7.33/9.71/1.98/17.01/63.97$ and $\phi = 0.5$; pressure and temperature at the end of the compression phase are $\langle p^* \rangle = 20$ bar and $\langle T^* \rangle = 850$ K, respectively. Solid lines correspond to adiabatic results and dashed lines show results with wall heat losses.

4.1.3 Compositional Variations of Test Gas Mixture

Effects of turbulence and compositional variations on the ignition behavior are investigated next. To this end, we will focus on the adiabatic formulation. Under this condition the LFP-model can be reduced to a two-scalar problem in which the temporal evolution of the mixture can be fully described by the mixture fraction Z and a reaction progress variable C. With this, the state-vector in Eq. (2.18) takes the form $\boldsymbol{\psi} = (Z, C)^T$, and the progress variable is defined from a linear combination of major product mass fractions, $C = Y_{CO_2} + Y_{CO} + Y_{H_2O} + Y_{H_2}$. This formulation allows for precomputing the reaction chemistry prior to the LFP-computation and tabulating all thermochemical quantities in terms of Z and C. Using this formulation, the LFP model is solved for a range of turbulence intensities $\mathcal{T}_u$ and initial mixture fraction fluctuations $\mathcal{T}_Z$. The mixture is selected from Ref. [26], having the following composition: $H_2/CO/CO_2/O_2/N_2 = 6.7/4.5/12.2/18.7/57.9$ and $\phi = 0.3$. The temperature and pressure at the end of the compression phase are $\langle T^* \rangle = 944$ K and $\langle p^* \rangle = 11.2$ bar, respectively. For the present case, the mean mixture stratification is set to zero. The mixture composition is

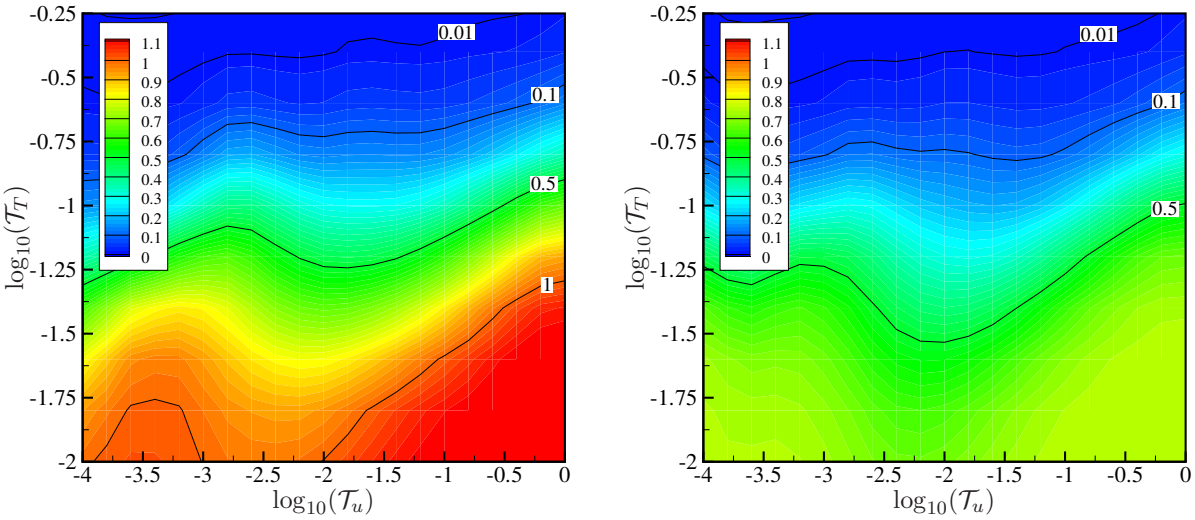

(a) Adiabatic condition.

(b) Non-adiabatic condition.

Figure 2.7: Ratio of the ignition delay times between LFP-model and homogeneous reactor solution, $\tau_{\mathrm{ig}}/\tau_{\mathrm{ig}}^{\mathrm{HR}}$, as function of turbulence intensity and temperature fluctuations: (a) adiabatic and (b) non-adiabatic conditions. The mixture composition is $H_2/O_2/CO_2/O_2/N_2 = 7.33/9.71/1.98/17.01/63.97$ and $\phi = 0.5$; pressure and temperature at the end of the compression phase are $\langle p_1^* \rangle = 20$ bar and $\langle T_1^* \rangle = 850$ K, respectively.

initialized from a beta-distribution [48]:

$$P(Z;\langle Z\rangle,\mathcal{T}_Z^2) = \frac{\Gamma(\alpha+\beta)}{\Gamma(\alpha)\Gamma(\beta)} Z^{\alpha-1}(1-Z)^{\beta-1} \tag{2.32}$$

in which the coefficients α, β, and γ are expressed in terms of $\langle Z\rangle$ and $\mathcal{T}_Z^2$:

$$\alpha = \langle Z\rangle\gamma\ , \qquad \beta = (1-\langle Z\rangle)\gamma\ , \qquad \gamma = \frac{\langle Z\rangle(1-\langle Z\rangle)}{\mathcal{T}_Z^2} - 1\ . \tag{2.33}$$

The progress variable for each particle is determined from the mixture composition for Z and the condition at the end of the compression phase.

Results for the temporal evolution of mean pressure and temperature are illustrated in Fig. 2.8. It can be seen that the LFP model agrees with the homogeneous reactor results (open symbols) for extremely small values of initial turbulence and scalar fluctuations, but deviates with increasing values of $\mathcal{T}_u$ and $\mathcal{T}_Z$. Higher turbulence levels lead to a successive reduction in ignition delay. For this particular mixture composition the reduction in ignition delay can reach an order of magnitude for $\mathcal{T}_u = 10^{-3}$. In this context it is noted that this value of $\mathcal{T}_u$ corresponds to rms velocity fluctuations of 0.4 m/s at the end of the compression phase, which is more than an order of magnitude smaller compared to the measurements by

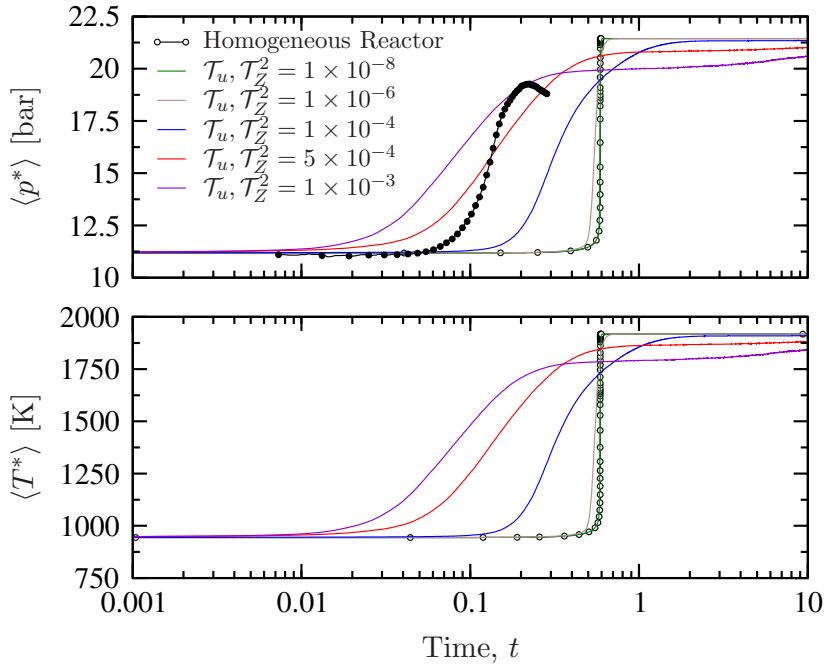

Figure 2.8: Evolution of mean pressure (top) and temperature (bottom) for different values of turbulence and scalar fluctuations. Open symbols correspond to homogeneous reactor results and the experimentally recorded pressure-history is shown by closed symbols [26] for qualitative comparisons. The mixture composition is $H_2/O_2/CO_2/O_2/N_2 = 6.7/4.5/12.2/18.7/57.9$ and $\phi = 0.3$; pressure and temperature at the end of the compression phase are $\langle p^* \rangle = 11.2$ bar and $\langle T^* \rangle = 944$ K, respectively.

Guibert *et al.* [34]. Such values appear to be reasonable, and belong to the lower turbulence regime for in-cylinder flows [36, 51].

From these results it is also evident that the turbulence not only affects the onset of the ignition but also the progress of reaction. Compared to the homogeneous reactor results, the rise in pressure and temperature reduces with increasing perturbation levels. This behavior is qualitatively similar to measurements, and is illustrated by the experimental data in Fig. 2.8 [26, 52]. The operating condition and mixture composition is identical to that used for the simulations, and the model results show a similar trend. Note that this allows only for a qualitative comparison since the degree of inhomogeneities in the test gas mixture was not measured, and effects other than compositional fluctuations could also be responsible for this ignition behavior.

4.1.4 Syngas Ignition and Combustion

The ignition analysis is further extended and effects of initial turbulence and equivalence ratio fluctuations on the ignition delay over a temperature range of $600\,\mathrm{K} \leq \langle \mathrm{T}^* \rangle \leq 1300\,\mathrm{K}$ are investigated.

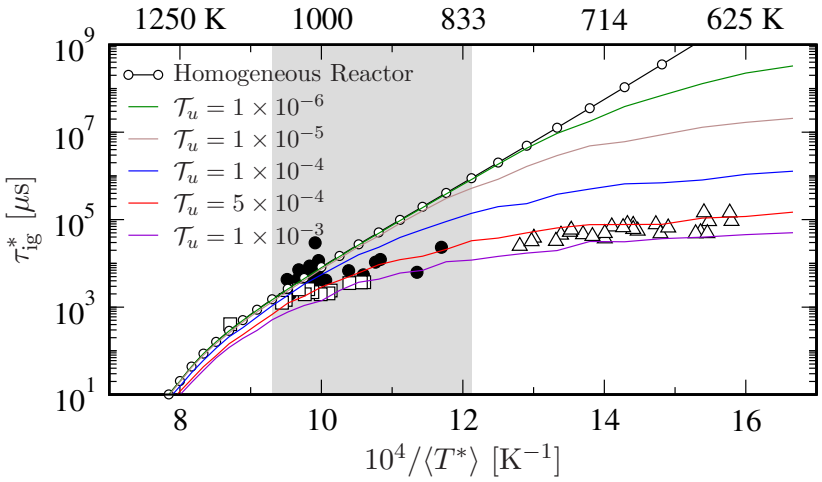

Figure 2.9: Ignition delay time of syngas/air mixtures. Experimental data are corrected to 20 atm assuming $1/\langle p^* \rangle$ proportionality [12]. Symbols correspond to: RCM • [26]; ST □ [12]; FR △ [53]. Mixture composition is $H_2/CO/CO_2/O_2/N_2 = 7.33/9.71/1.98/17.01/63.97$ and $\phi = 0.5$; pressure at the end of the compression phase is $\langle p^* \rangle = 20$ atm; gray area illustrates the typical RCM-operating range.

Modeling results and comparisons with experimental data for ignition delay times are shown in Fig. 2.9. Results from the RCM model (lines) show that effects of turbulence are mainly pronounced at low temperatures, which is evident from the results with $\mathcal{T}_u = \mathcal{T}_Z^2 = 1 \times 10^{-6}$ (green line in Fig. 2.9). However, with increasing levels of turbulence and mixture fluctuations, ignition delay times at higher temperatures become increasingly affected. This can be explained through a Damköhler number analysis, comparing the characteristic turbulence time scale with the ignition delay time:

$$\mathrm{Da}_{\mathrm{ig}} = \frac{\tau_0^*}{\tau_{\mathrm{ig}}^*} \propto \frac{1}{\xi^{3/2}} \frac{1}{\mathcal{T}_u} \frac{\tau^*}{\tau_{\mathrm{ig}}^*} \,. \tag{2.34}$$

Large values of $\mathrm{Da}_{\mathrm{ig}}$ identify ignition-dominated processes which are unaffected by turbulent mixing.

The Damköhler number is evaluated from the simulation results, and is illustrated in Fig. 2.10. Isocontours for three values of $\mathrm{Da}_{\mathrm{ig}}$ are shown. It can be seen that all ignition delay curves converge for $\mathrm{Da}_{\mathrm{ig}} \geq 100$ and asymptote to the homogeneous reactor results. This analysis suggests that Eq. (2.34) can be utilized as criterion to assess the significance of turbulent mixing and mixture fluctuations on the ignition process.

The RCM model parametrically captures the experimentally observed trend that the ignition delay time asymptotes to a constant value around 100 ms for low mixture temperatures (see Fig. 2.9). Although the data for $\langle T^* \rangle < 800$ K are obtained from flow reactor experiments, the proposed model predicts a similar behavior. This suggests that turbulence effects could also be of relevance in flow reactors, and further research is required to confirm this hypothesis.

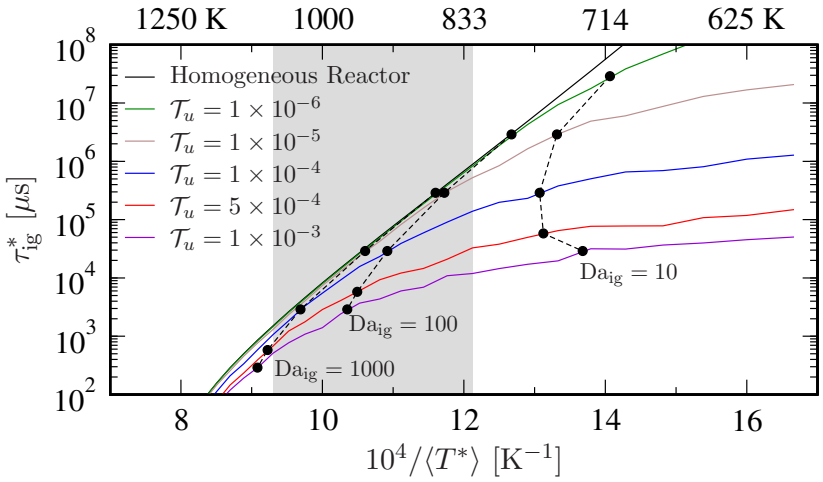

Figure 2.10: Damköhler number criterion for syngas ignition analysis. Mixture composition and operating conditions are the same as in Fig. 2.9. Dashed lines with symbols correspond to curves of constant Damköhler numbers, $\mathrm{Da_{ig}} = \{10, 100, 1000\}$.

5 Discussion

A parametric study was performed to investigate effects of turbulence, fluctuation in mixture composition and temperature, and wall heat transfer on the ignition dynamics of lean syngas mixtures in RCMs. The state of the test gas at the end of the compression phase was evaluated by considering the mean-strain induced amplification of turbulence and compositional perturbations during the piston compression. Turbulence-generating mechanisms and compositional variations of the test-gas mixture are parametrically represented by the turbulence intensity $\mathcal{T}_u$ and fluctuations in composition and temperature, $\mathcal{T}_{\boldsymbol{Y}}$ and $\mathcal{T}_T$, respectively. As such, this model can be used for investigating ignition sensitivities to relevant process parameters and operating conditions. The fidelity of this low-order model can be enhanced by injecting facility-specific information about turbulence levels and mixture inhomogeneities that are either obtained from measurements or detailed simulations.

The ignition of the syngas mixture is modeled as a stochastic process. This formulation, which reduces to the homogeneous reactor model in the absence of turbulence and perturbations in mixture composition and temperature, accounts for the micromixing among different ignition environments. The current model formulation considers the volumetric ignition regime, and only incompletely characterizes front-like combustion modes [26, 34, 35]. However, such effects can be incorporated in the RCM ignition model. In this regard it is noted that this model can also be of relevance for application to homogeneous and stratified charge compression ignition (H/SCCI) in internal combustion engines [54]. In these advanced engine concepts, thermal and mixture inhomogeneities are present, resulting in sequential ignition of the mixture and the presence of deflagrative and front-like combustion

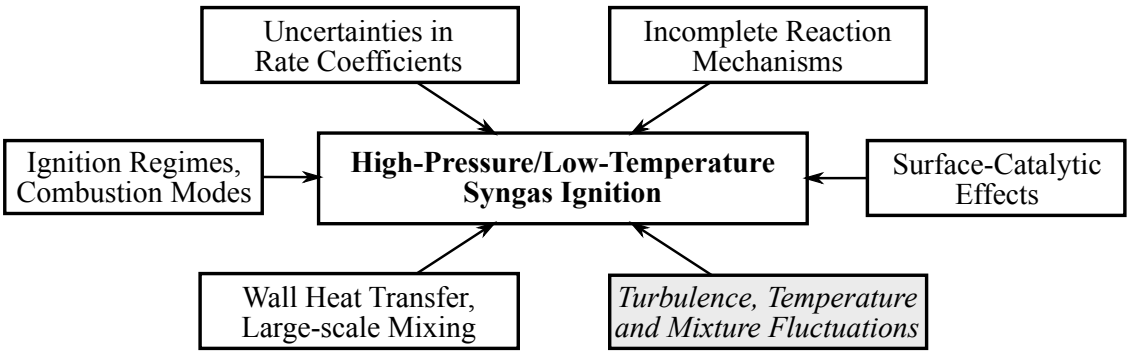

Figure 2.11: Chemical-kinetics and hydrodynamic processes affecting the syngas ignition at high-pressure/low-temperature conditions.

regimes [55, 56].

In the previous section, a Damköhler criterion was introduced to quantify the role of turbulence on the ignition process. It was shown that with decreasing values of Damköhler number (corresponding to decreasing temperature), turbulence and mixture fluctuations become increasingly effective in controlling the induction chemistry. This suggests that turbulence/chemistry interaction can become of equal importance as chemical-kinetics and hydrodynamics processes which have been previously identified as key mechanisms [1, 25] for the observed discrepancies between measured and computed ignition delay times. These mechanisms are schematically summarized in Fig. 2.11. The identified dependency of the low-temperature syngas ignition to turbulence and mixture inhomogeneities requires the careful control and characterization of RCM-operating conditions. With a few exceptions of measurements during the ignition process [34], the experimental characterization of turbulence and compositional perturbations before and during the compression phase have not been performed, and are of interest for future model comparison. Such measurements would also be helpful in delineating facility-specific turbulence contributions arising from the mixture-preparation and filling processes, boundary-layer generated turbulence, and corner-vortices.

Currently the significance of the turbulence on the ignition process in RCMs is not fully appreciated so that CFD studies have been typically performed under laminar conditions [30, 57]. Although an important first step, such simulations only provide an incomplete description of the flow field structure, and caution must be exercised when these results are compared with zero-dimensional models and measurements. In this context it is also noted that laminar or ensemble-averaged RANS (Reynolds-averaged Navier-Stokes) calculations in combination with equilibrium turbulence closure models appear to be inappropriate for RCM-simulations for at least two reasons. First, the strong mean strain, generated by the rapid piston motion, results in the generation of non-equilibrium turbulence. Since standard k–ε turbulence models are derived from equilibrium arguments, the Reynolds-stresses are considerably over-predicted. This represents a limitation of standard two-equation models, and

Reynolds-stress models will most-likely provide improved predictions for the non-equilibrium turbulence amplification in RCMs. The second concern addresses the description of the ignition and combustion processes. The ignition process in RCMs evolves on sub-millimeter scales and is typically not resolved in laminar/RANS CFD calculations. Because of these modeling challenges, it is speculated that detailed unsteady simulations with adequate resolution of small-scale ignition processes and turbulence/chemistry interaction are required to provide a quantitative description of the flow field structure and combustion in RCMs.

Although this study only considered an idealized RCM-facility and syngas-mixture, based on these modeling results the following recommendations can be made to further assess the relevance of nonidealities in rapid compression machines:

- Parametric studies identified turbulence and fluctuations in temperature and composition as potential sources for systematic errors in RCM-measurements. These errors are presumably dependent on operating conditions and facility-specific, and could exacerbate other non-idealities that arise from heat-transfer, mixture impurities, catalytic effects, among others.
- Different facility-specific sources of inhomogeneities were identified. Detailed measurements of turbulence and flow-field structure throughout the compression stroke and ignition phase are desirable to improve the quantitative understanding about these hydrodynamic processes. Such measurements are also helpful to further constrain the parameters in the RCM-model.
- Depending on the Damköhler criterion, the turbulence/chemistry interaction could add a stochastic component to the RCM-ignition process. This would require multiple experiments to obtain statistically significant results and quantify experimental uncertainties.
- Model results suggest that comparisons of global quantities, such as ignition delay and equilibrium composition, remain relatively insensitive to facility-induced perturbations. Therefore, time-resolved measurements for temperature, pressure, speciation, and wall-heat flux would be desirable to enable a systematic comparison with computational models and high-fidelity simulations.

Chapter 3

Development of a Regime Diagram for Rapid Compression Machines

1 Introduction

Rapid compression machines (RCMs) [58], like shock-tubes [59], and flow/jet reactors [60], are used to study fuel decomposition and ignition behavior at elevated temperature and pressure conditions that are representative of combustion engine environments. These different experimental devices are designed to isolate chemical kinetic phenomena from other complex processes that occur within the combustion chamber during engine operation such as spray breakup, fuel evaporation, and mixing. There is a long history of development of RCMs, and modern configurations are generally well-characterized over a range of conditions. Typical temperature and ignition delay ranges accessed by RCMs are depicted in Fig. 3.1, where it can be seen that regions of overlap exist between the different types of chemical reactors.

RCMs typically explore ignition behavior using realistic fuel loadings ($\phi \approx 0.5 - 2, \mathrm{O_2} \approx 5 - 21\,\%$), which is similar to what is employed in operating engines. Other devices, such as shock-tubes, are usually operated under lean or dilute conditions ($\phi < 0.5, \mathrm{O_2} < 1\,\%$) in order to minimize thermal feedback and inhomogeneities that can result from exothermic and endothermic processes, as well as other operational challenges such as excessive pressure rise rates. Complementary data can be acquired through the use of a variety of apparatuses towards the development of predictive reaction mechanisms and other combustion models.

Idealized reactors like RCMs can be influenced by physical processes which result in coupled chemico-physical phenomena, and this leads to non-ideal experimental conditions. Measurements and interpretation of datasets under these scenarios can be complicated. In RCMs such processes can include heat loss and complex fluid dynamics, as well as turbulent fluctuations and the development of non-uniform or deflagrative ignition.

Heat loss is particularly notable in RCMs since piston compression and test times can be long (e.g., τ_{comp} =15–80 ms, τ_{ign} = 10–100 ms), while the walls of the reaction chamber are substantially cooler than the reacting gas. During the test period, a boundary layer forms and

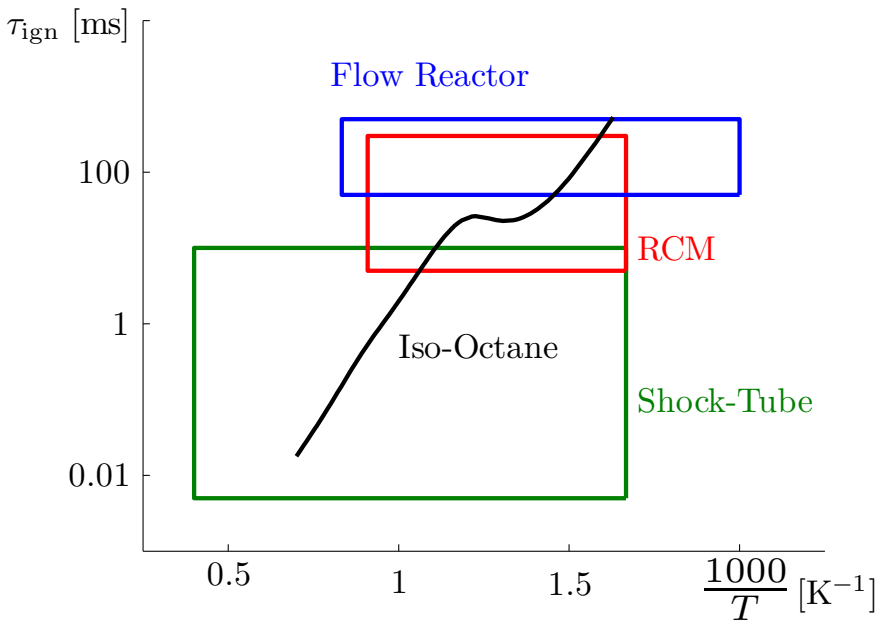

Figure 3.1: (Color online) Typical operational boundaries of shock-tubes, rapid compression machines, and flow reactors. A comparison to a representative ignition delay curve of iso-octane is included; ignition delay of iso-octane obtained from the reduced mechanism of Pepiot-Desjardins and Pitsch [61] at an equivalence ratio of 0.6 and a pressure of 20 bar.

diffuses into the test section such that a significant variation of temperature can be present throughout the RCM, and no definable core exists at very long test times. Additionally, at some point the reactivity can be quenched, and ignition does not occur.

Complex fluid dynamics can exist within RCMs, and their influence on ignition has been recognized for many years. A particular focus of late has been the generation of a toroidal vortex in the reaction chamber during piston compression, where this can occur even for mixtures that are initially quiescent [62]. The fluid dynamic structure that develops at the interface between the piston and the cylinder wall can evolve during the test period and mix the "adiabatic core" gas with cooler boundary layer gases leading to highly non-homogeneous conditions within the reaction chamber.

Park and Keck [62] first suggested the use of a crevice volume machined around the circumference of the piston to capture the boundary layer during compression and prevent the formation of this vortex. Lee and Hochgreb [30] expanded upon this idea and conducted computational fluid dynamics (CFD) simulations of the process to devise guidelines for an adequate crevice configuration.

Mittal and Sung [32] used CFD simulations and conducted experimental measurements with acetone planar laser induced fluorescence (PLIF) to better understand the evolution of

the fluid dynamic motion within the reaction chamber and verify the performance of their crevice design. Their measurements confirmed the capability of the crevice to suppress the roll-up vortex and achieve very uniform conditions across the "adiabatic core" for high pressure cases studied ($p = 40$ bar). Normalized root mean squared (RMS) temperatures under these conditions were near $T'/\langle T \rangle = 0.01$, which is within the experimental uncertainties of the PLIF measurements, while average gradients were on the order of $\mathrm{d}T/\mathrm{d}\xi = 2$ K/mm, with peak values near 5–10 K/mm. However, for the low pressure tests ($p = 12$ bar), the vortex formation was not suppressed due to the three times larger thermal diffusivity of the gas, and normalized RMS temperatures increased to $T'/\langle T \rangle = 0.02$ with mean gradients closer to $\mathrm{d}T/\mathrm{d}\xi = 4$ K/mm and peak values near 10–15 K/mm.

Turbulent fluctuations within the reaction chamber can generate or amplify inhomogeneities within the "adiabatic core" during piston compression, and interact with the chemical kinetic processes during the delay period including the main heat release process. The development of turbulent conditions however has not been investigated widely, especially outside of studies where bulk fluid motion is not suppressed (e.g., via piston crevices). Turbulence can be introduced into the RCM via a variety of means including latent turbulence from the filling process, turbulence generated by boundary layer instabilities, development of corner vortices during the compression stroke, and production of turbulence from the mean strain induced by the compression [63, 64].

Guibert *et al.* [34] studied the decay of the mean total kinetic energy during the delay period using particle image velocimetry (PIV) techniques. They noted that under short ignition delay times, the turbulence can interact with the chemical heat release. The configuration used for their investigation employed a mesh at the interface between the reaction chamber and compression cylinder to generate turbulent flow fields. As such, it is difficult to directly apply their findings to typical RCM configurations where the bulk flow field is suppressed.

Ihme [63] developed a stochastic multi-scale model to investigate the evolution of velocity and temperature fluctuations during piston compression and the ignition delay period, covering a range of geometric and operating conditions. This model indicated that increased compression ratios can significantly enhance local stratification, while the heat release profile and ignition timing can be substantially altered under low Damköhler conditions.

Deflagrative ignition, which is referred to as "mild ignition" in this work, occurs when flames develop within the reaction chamber. These develop from localized ignition kernels and can consume the entire mixture, or promote volumetric ignition of the remaining unburned charge. Ignition delay times are generally shortened during mild ignition events, while the rates of pressure rise are much slower than under uniform ignition conditions. The term "weak ignition" is not used here to describe these events, as this terminology has been used in past works to identify regimes where autoignition is not fully chemically branched, and is significantly influenced by chemical energy release, evolving from a relatively slow process and transitioning to rapid heat release at the point of main ignition.

Mild ignition phenomena were first documented in an RCM by Livengood and Leary [65] who employed Schlieren techniques and high speed photography using an optically accessible

configuration. They identified regions of thermal stratification along with the evolution of flame fronts during autoignition. By considering different fuels, they concluded that the stratification was primarily caused by the piston motion, where the piston scrapes the boundary layer from the cylinder walls, producing a turbulent region at the periphery of the chamber.

Many researchers, including Oppenheim and co-workers [66,67], Adomeit and co-workers [68, 69], Yamashita *et al.* [70] and Uygun *et al.* [71], subsequently investigated mild ignition processes within shock-tubes using Schlieren techniques. These groups studied influences of thermal and reactivity gradients generated by their configurations, and they explored the sensitivities of various fuels to these gradients.

Wooldridge and coworkers [26, 72–74] studied mild ignition phenomena in syngas and iso-octane mixtures using a RCM where a wide range of fuel loadings ($\phi = 0.1 - 0.7$ and $\phi = 0.2 - 1$, respectively) and pressures ($p = 3 - 20$ bar and $5 - 20$ bar, respectively) was covered in the intermediate temperature regime ($T = 800 - 1100$ K and $T = 900 - 1050$ K, respectively). They employed high speed chemiluminescence photography to distinguish between mild and uniform ignition events, and determined ignition front velocities for some of their non-uniform ignition data. They also developed sensitivity diagrams for some of their mixtures in order to identify thermodynamic regimes where mild ignition can be observed. An assumed thermal gradient near $\mathrm{d}T/\mathrm{d}\xi = 5 - 10$ K/mm was employed to help delineate the different regions of ignition.

Strozzi *et al.* [75] investigated mild ignition of methane/air mixtures using a square cross-section, flat piston configuration. They employed toluene PLIF measurements to characterize thermal inhomogeneities within the reaction chamber, and PIV to ascertain the characteristics of the velocity fields. Their measurements showed regions of high RMS temperature and thermal gradients ($T'/\langle T\rangle > 0.07$ and $\mathrm{d}T/\mathrm{d}\xi > 100$ K/mm). The data were used to explore differences between spontaneous ignition front propagation and deflagration within the mixtures, and found that under the conditions examined, most of the heat release occurred via heterogeneous ignition.

Figure 3.1 is representative of the test conditions explored by three categories of chemical reactors; however, it is an incomplete description of the capabilities of a given facility. A more thorough description incorporates the relevant physical time scales of the system; hence, it is the ambition of this paper to elucidate these physical processes for rapid compression machines as was done for flow reactors [76]. Specifically, by employing essential scaling analysis of processes involving hydrodynamics, turbulence, heat transfer, ignition, and combustion, a regime diagram is developed to delineate relevant ignition regimes in RCMs. The utilization of this regime diagram can lead to better experimental designs as well as operating protocol, which can more confidently target ignition regimes of interest. For instance, studies focused on chemical kinetics of fuel decomposition should be conducted in a regime where thermal quenching will not occur and ignition is absent of deflagrative and detonative processes.

2 Ignition regime diagram for rapid compression machines

RCMs typically seek to operate in regimes with simple gas dynamics for chemical kinetic studies. However, the action of compressing the test gas induces perturbations to the flow field, which can have a significant effect on the character of the ignition event. Additionally, heat loss to the walls complicates the interpretation of RCM measurements and can lead to thermal quenching.

To decipher the governing parameters within an RCM at the test conditions, consider the energy equation:

$$\rho c_v \frac{\partial T}{\partial t} = -\rho c_v \underline{u} \cdot \nabla T - \sum_{i=1}^{N_s} e_i \dot{\omega}_i + \nabla \cdot (\lambda \nabla T) \ , \tag{3.1}$$

where work and mass diffusion terms are ignored. Work terms are considered negligible outside of the compression stage, and inhomogeneities in species concentration are likely small since the boundaries are non-catalytic. Non-dimensionalizing Eq. (3.1) with respect to the condition at the end of compression or top dead center (TDC), the energy equation becomes

$$\frac{\partial T^*}{\partial t^*} = -\underline{u}^* \cdot \nabla^* T^* - \frac{\gamma \mathrm{Da_t}}{\mathcal{A}} \sum_{i=1}^{N_s} e_i^* \dot{\omega}_i^* + \frac{\gamma}{\mathrm{PrRe_t}} \nabla^* \cdot (\lambda^* \nabla^* T^*) \ , \tag{3.2}$$

where the superscript "*" indicates a non-dimensionalized variable, $\mathrm{Da_t}$ is the turbulent Damköhler number, γ is the specific heat ratio, and $\mathcal{A}$ is the Arrhenius factor. The Arrhenius factor is discussed more extensively in Sec. 2.2.1. The Prandtl number is defined as $\mathrm{Pr} = \nu/\alpha$, and $\mathrm{Re_t}$ is the turbulent Reynolds number. The turbulent Damköhler number is defined as [63]:

$$\mathrm{Da_t} = \frac{\tau_t}{\tau_{\mathrm{ign}}} \ , \tag{3.3}$$

where τ_t is the turbulent time scale defined as the ratio of the integral length scale to the turbulent velocity fluctuation ($\tau_t = l/u'$), and τ_{ign} is the ignition delay time for the mixture. The ignition delay is the chemical kinetics time and is considered to be unaffected by turbulence and heat transfer in this definition. Additionally, this paper defines all relevant variables in algebraic expressions with respect to the conditions at TDC unless otherwise noted. Hence, the turbulent Damköhler number compares the turbulent mixing time scale to the chemical time scale of the mixture.

The turbulent Reynolds number is defined as

$$\mathrm{Re_t} = \frac{u' l}{\nu} \ , \tag{3.4}$$

where ν is the kinematic viscosity. The turbulent Reynolds number can be interpreted as a

competition between a viscous dissipation time scale and a turbulent mixing time scale:

$$\mathrm{Re_t} = \frac{\tau_\nu}{\tau_\mathrm{t}} \ , \tag{3.5}$$

where the viscous time scale is defined as $\tau_\nu = l^2/\nu$. Equation (3.2) assumes that the heat transfer time scale is linearly related to the viscous time scale through the Prandtl number: $\tau_Q = \mathrm{Pr}\tau_\nu$.

The non-dimensional energy equation governing the ignition process given by Eq. (3.2) is shown to be parameterized by the turbulent Damköhler number and the turbulent Reynolds number. Considering both parameters, a combustion regime diagram for RCMs was developed and is presented in Fig. 3.2. The subsequent sections derive the demarcations shown in Fig. 3.2 starting with the demarcations pertaining to the turbulence levels in Sec. 2.1, then the demarcations associated with the characterization of the ignition events (i.e., strong, mixed, mild, or pre-ignition) in Sec. 2.2, and finally, the demarcations primarily associated with heat transfer effects in Sec. 2.3.

2.1 Turbulence

Turbulence can have a substantial effect on the quality of ignition and can lead to erroneous assessments or predictions of ignition delay. Turbulence is a highly nonlinear and dimensional process which cannot be easily incorporated into models of RCMs with high accuracy. Hence, regimes in which turbulence substantially affects the ignition process in a chemical kinetic experiment should be avoided.

A schematic of the turbulent flow field at TDC is shown in Fig. 3.3. The turbulent flow field in an RCM consists of a diversity of length scales including the integral length scale l, the Taylor microscale λ_T, and the Kolmogorov length scale η. Ignition kernel formation occurs at an intermediate scale between the integral length scale and the Kolmogorov scale, and Peters *et al.* [77] showed through dissipation element theory that kernel formation occurs at length scales similar to the Taylor microscale. Additionally, a boundary layer of cold fluid, with length scale δ, develops at the wall of an RCM. As discussed in the Introduction, the dynamics of this boundary layer has a significant effect on the temperature field within the RCM.

2.1.1 Quiescent ignition

When studying chemical kinetics, a quiescent flow would be desirable for RCM experiments. Quiescent ignition occurs when the reaction proceeds uniformly within the test section, and there is no turbulence in the flow. When the flow is quiescent and ignition is not quenched due to heat loss to the walls, the mixture ignites uniformly. As demonstrated by Eq. (3.5), the turbulent Reynolds number is the ratio of the viscous and turbulent time scales. Hence, for short viscous time scales compared to the turbulent mixing time scale, the mixture homogenizes throughout the test section leading to a uniform ignition event. Therefore, the

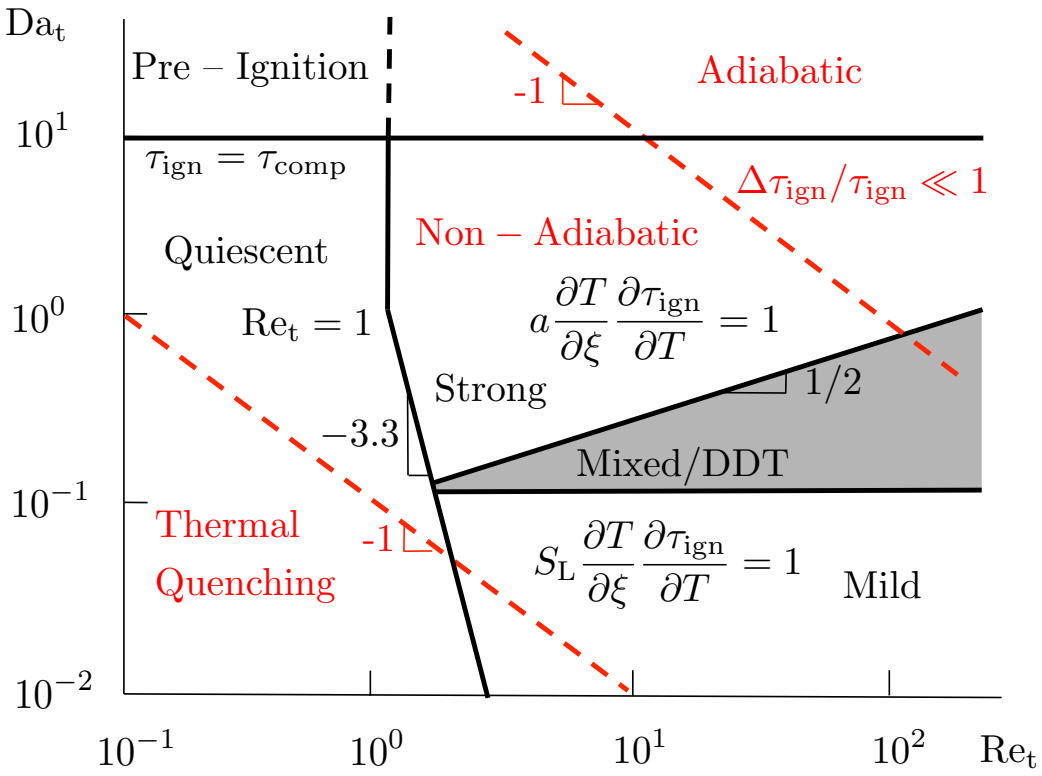

Figure 3.2: (Color online) Diagram illustrating the combustion regimes occurring in RCM experiments. The abscissa is the turbulent Reynolds number given by Eq. (3.4) and the ordinate is the turbulent Damköhler number given by Eq. (3.3). The black lines indicates demarcations of the quality of ignition, and the **RED** lines show demarcations relevant to heat transfer. The gray area for the mixed/DDT region is meant to emphasize that this is a transitional regime.

quiescent region is demarcated by the line $Re_t = 1$. This scaling is included as a vertical line bounding the quiescent regime in Fig. 3.2. However, the quiescent regime is rather difficult to achieve experimentally without other non-idealities dominating; the piston velocity would be such that appreciable radical and boundary layer build-up would occur during the compression stroke. Additionally, homogeneous ignition can also occur when the mixture is turbulent, and the delineation for this regime is examined in a Sec. 2.2.1.

2.1.2 Turbulence decay

For long ignition delay times, the turbulence within an RCM may decay to a level where it has no effect on the quality of the ignition. In these cases, the core fluid ignites uniformly without a flame or detonation front forming. Assuming homogeneous turbulence at the end of the compression stroke, the decay of the turbulence can be modeled with the following

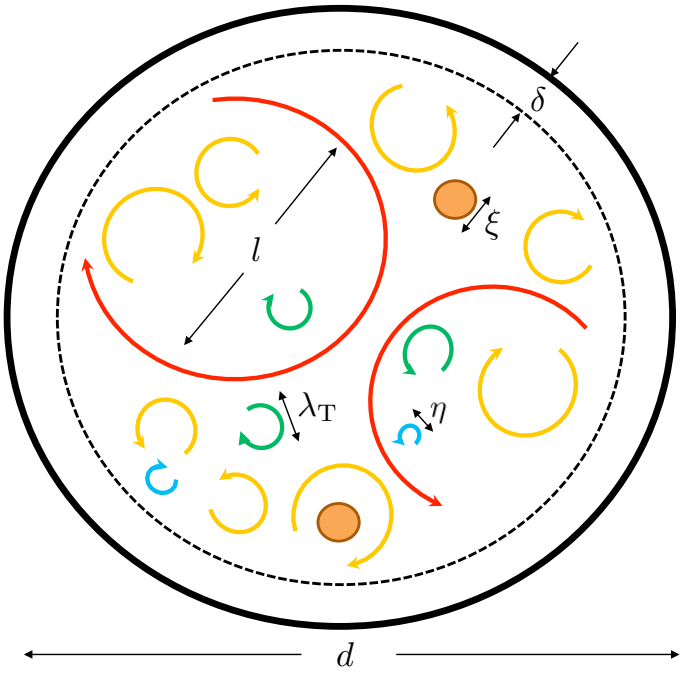

Figure 3.3: (Color online) Schematic of the turbulent field within a rapid compression machine at the time at the end of compression. l is the integral length scale, λ_{T} is the Taylor microscale, η is the Kolmogorov scale, d is the diameter of the RCM, δ is the length of the thermal boundary layer, and ξ is the characteristic length scale of an ignition kernel.

power laws [46]:

$$\frac{k_{\mathrm{ign}}}{k} = \left(1 + \frac{\tau_{\mathrm{ign}}}{\tau_{\mathrm{t}}}\right)^{-n} , \tag{3.6a}$$

$$\frac{\varepsilon_{\mathrm{ign}}}{\varepsilon} = \left(1 + \frac{\tau_{\mathrm{ign}}}{\tau_{\mathrm{t}}}\right)^{-(1+n)} , \tag{3.6b}$$

where k is the turbulent kinetic energy, ε is the turbulent dissipation rate, the subscript "ign" indicates the state at the time of ignition, and the exponent n is taken to be 1.3 from Pope [46]. By reformulating the turbulent and viscous time scales in terms of k and ε using dimensional analysis, the turbulent Reynolds number given in Eq. (3.4) can be rewritten as

$$\mathrm{Re}_{\mathrm{t}} = \frac{k^2}{\varepsilon \nu} . \tag{3.7}$$

Dividing Eq. (3.6b) by the square of Eq. (3.6a), assuming that viscosity does not vary appreciably during the induction period, and substituting the turbulent Reynolds number given

in Eq. (3.7), Eqs. (3.6) can be expressed as

$$\frac{\mathrm{Re_t}}{\mathrm{Re_{t,ign}}} = \left(1 + \frac{\tau_{\mathrm{ign}}}{\tau_{\mathrm{t}}}\right)^{n-1} . \tag{3.8}$$

The flow becomes quiescent at the time of ignition when $\mathrm{Re_{t,ign}} = 1$. Applying this criterion, substituting the definition of the turbulent Damköhler number, and rearranging, Eq. (3.8) becomes

$$\mathrm{Da_t} = \frac{\mathrm{Re_t^{-m}}}{1 - \mathrm{Re_t^{-m}}} , \tag{3.9}$$

where $m = (n-1)^{-1} \approx 3.3$. For $\mathrm{Re_t} \gg 1$, Eq. (3.9) reduces to the following:

$$\mathrm{Da_t} = \mathrm{Re_t^{-m}} . \tag{3.10}$$

If the Damköhler number is below the demarcation given in Eq. (3.10), the flow becomes quiescent before the time of ignition, and therefore, the core fluid is likely to ignite uniformly. The delineation given by Eq. (3.10), is shown in Fig. 3.2 as having a slope of -3.3.

2.1.3 Estimation of turbulence statistics

Since turbulence statistics are rarely measured in RCMs, the turbulent time scale can be estimated assuming the following relations:

$$\mathcal{T}_u = \frac{u'}{U_{\mathrm{P}}} , \tag{3.11a}$$

$$\mathrm{C}_l = \frac{l}{d} , \tag{3.11b}$$

where $\mathcal{T}_u$ is the turbulence intensity, and U_{p} is the characteristic velocity of the piston in the RCM (either known or estimated by stroke length and compression time), C_l is a proportionality constant, and d is the diameter of the RCM. The turbulence intensity is used to relate the piston velocity to the RMS velocity. This quantity is most likely machine-dependent and can be affected by other factors including crevice, piston, compression chamber, and reaction-chamber design. However, the ratio of the integral length scale to the diameter is unlikely to vary appreciably between machines.

As discussed in the introduction, much work has been undertaken to minimize the hydrodynamic fluctuations through the insertion of optimized crevices in RCMs [30, 32, 62]. The present analysis incorporates the effects of geometric complexity of crevice design through the turbulent intensity, $\mathcal{T}_u$. For highest accuracy, this is a quantity that would need to be measured for a particular RCM.

Using Eqs. (3.11), the turbulent time scale can be estimated as:

$$\tau_{\mathrm{t}} = \left(\frac{\mathrm{C}_l}{\mathcal{T}_u}\right) \frac{d}{U_{\mathrm{p}}} . \tag{3.12}$$

Hence, the turbulent time scale is dependent on the geometry of the RCM as indicated by $\mathcal{T}_u$ and d, and the speed of the piston U_{P}.

2.2 Chemistry

Manifestly, the chemistry of the test gas is of great importance in all regimes of chemical kinetic experiments. However, within regimes that delineate the quality of ignition, the chemical sensitivities of the test mixture dominate. Mild ignition is a chemico-physical phenomenon driven by turbulence and chemical sensitivity. Mild ignition differs from strong ignition phenomena due the inhomogeneous nature of the ignition event, which is characterized by ignition kernel formation. The ignition kernels form from turbulent fluctuations in temperatures in the test gas. From the presumption of a turbulent flow field, several regime demarcations can be postulated to segregate homogeneous and mild ignition regimes in RCMs.

First, the regime demarcation for the strong ignition will be discussed, and subsequently, the delineation for the mild ignition regime will be examined.

2.2.1 SWACER and the strong ignition limit

Shock Wave Amplification by Coherent Energy Release (SWACER) [78, 79] is a mechanism that explains the transition of isolated ignition kernels to detonation. SWACER theory predicts a spontaneous transition into a detonation wave if there is a coherent coupling of pressure waves and heat release at the ignition kernel [80]. The transition criterion is given as

$$\frac{a}{u_{\mathrm{RF}}} = 1 \ , \tag{3.13}$$

where a is the speed of sound in the mixture, and u_{RF} is the speed of the reaction front. Using Zeldovich's relation for the speed of the ignition front [55], the following criterion is obtained:

$$a \frac{\partial T}{\partial \xi} \frac{\partial \tau_{\mathrm{ign}}}{\partial T} = 1 \ , \tag{3.14}$$

where ξ is the spatial coordinate normal to the reaction front. Gu *et al.* [81] studied the transition of a flame kernel to a detonation wave in one-dimensional simulations and found acceptable agreement between Eq. (3.14) and the computed transition. The SWACER mechanism has been found to be relevant in inhomogeneous ignition phenomena [82]. Additional mechanisms for deflagration-to-detonation transition (DDT), including kernel-wall-interaction and kernel-kernel-interaction, are discussed by Blumenthal *et al.* [83] in the context of shock-tube systems.

Assuming an Arrhenius form, the ignition delay is given by

$$\tau_{\mathrm{ign}} = B \exp\left(\frac{E_{\mathrm{A}}}{\mathcal{R}T}\right) \ , \tag{3.15}$$

where B is an exponential prefactor that is generally a function of density, E_A is the activation energy, and $\mathcal{R}$ is the universal gas constant. Taking the partial derivative of Eq. (3.15) with respect to temperature and defining the Arrhenius factor as $\mathcal{A} = E_\mathrm{A}/\mathcal{R}T$, the partial derivative of the ignition delay is given as

$$\frac{\partial \tau_\mathrm{ign}}{\partial T} = -\frac{\mathcal{A}}{T}\tau_\mathrm{ign} \ . \tag{3.16}$$

Following Peters *et al.* [77], the Taylor microscale, λ_T, is employed as the characteristic dimension of a flame kernel. From this, the temperature gradient is approximated as

$$\frac{\partial T}{\partial \xi} \approx -\frac{T'}{\lambda_\mathrm{T}} = -\mathcal{T}_T \frac{T}{\lambda_\mathrm{T}} \ , \tag{3.17}$$

where $\mathcal{T}_T$ is the temperature fluctuation level. Substituting Eqs. (3.16) and (3.17) into Eq. (3.14) the following relation is obtained:

$$a\mathcal{T}_T \tau_\mathrm{ign} \frac{\mathcal{A}}{\lambda_\mathrm{T}} = 1 \ . \tag{3.18}$$

Using homogeneous turbulence theory [46], the Taylor microscale is given by

$$\lambda_\mathrm{T} = \sqrt{10\nu\tau_\mathrm{t}} \ . \tag{3.19}$$

Defining the relevant Mach number as

$$\mathrm{M} = \frac{U_\mathrm{p}}{a} \ , \tag{3.20}$$

and substituting the definitions of the turbulent Reynolds number and the turbulent Damköhler number, given in Eqs. (3.4) and (3.3), respectively, the SWACER criterion is found to be

$$\mathrm{Da_t} = \left(\frac{\mathcal{T}_T}{\mathcal{T}_u}\right) \frac{\mathcal{A}}{\mathrm{M}\sqrt{10}} \mathrm{Re_t}^{1/2} \ . \tag{3.21}$$

This equation shows the influence of compressibility and chemistry by the appearance of the Mach number and the Arrhenius factor, respectively; however, independence of the SWACER criterion to the design of the RCM is shown since it is likely that $\mathcal{T}_T \propto \mathcal{T}_u$. This criterion designates the propensity of a mixture to ignite either as a detonation or as a supersonic autoignition wave. The latter is interpreted in the context of an RCM as a strong ignition event. The demarcation between mixed and strong ignition, given by Eq. (3.21), is shown in Fig. 3.2 and has a slope of 1/2.

2.2.2 Sankaran criterion

Sankaran *et al.* [84] postulated that a comparison between the velocity of the reaction front of an ignition kernel to the laminar flame speed yields a demarcation that indicates the propensity of a mixture towards mild ignition. This criterion is given as

$$\frac{S_{\mathrm{L}}}{u_{\mathrm{RF}}} = 1 \ , \tag{3.22}$$

where S_{L} is the laminar flame speed, and u_{RF} is the speed of the ignition front. The Sankaran criterion is qualitatively similar to the SWACER criterion. However, the Sankaran criterion is meant to demarcate the regime in which the mixture forms flame kernels, and the SWACER criterion is meant to indicate the propensity of a flame kernel to transition to a detonation. Hence, the region bounded by these criteria is a transitional regime where a flame kernel readily transitions into a detonation wave or experiences mixed ignition. A mixed ignition event is characterized as a transient ignition state where flame fronts are produced before the mixture undergoes uniform ignition, as discussed in the Introduction.

The evaluation of the speed of the reaction front is the same as that for the SWACER criterion. Using a two-zone model for a laminar premixed flame [85], the laminar flame speed is approximated as

$$S_{\mathrm{L}}^2 \approx 2\alpha \frac{\dot{\omega}_{\mathrm{F}}(T_{\mathrm{f}})}{\rho_{\mathrm{F}}} \ , \tag{3.23}$$

where α is the thermal diffusivity, $\dot{\omega}_{\mathrm{F}}$ is the consumption rate of the fuel, and ρ_{F} is the initial density of the fuel in the mixture. The consumption rate of the fuel is evaluated at the flame temperature of the fuel since the high temperature kinetics in the reaction zone dominates. For an autoignition event, a linear relationship between the ratio of fuel density to fuel consumption rate and ignition delay is assumed:

$$\frac{\rho_{\mathrm{F}}}{\dot{\omega}_{\mathrm{F}}(T_{\mathrm{f}})} = \mathrm{C}_{\mathrm{ign}} \tau_{\mathrm{ign}} \ , \tag{3.24}$$

where $\mathrm{C}_{\mathrm{ign}}$ is a proportionality constant.

Using the high activation energy asymptotics for a thermal explosion, given in Law [10], and comparing it to Eq. (3.24), the coefficient $\mathrm{C}_{\mathrm{ign}}$ is deduced to be

$$\mathrm{C}_{\mathrm{ign}} = \gamma\beta\mathcal{A}\ Y_{\mathrm{F}} \exp\left(-\mathcal{A}\frac{\beta}{\beta+1}\right), \tag{3.25}$$

where γ is the heat capacity ratio, β is the heat release parameter, and Y_{F} is the mass fraction of the fuel. The heat release parameter, $\beta = \Delta H_{\mathrm{C}}/c_p T \approx (T_{\mathrm{f}} - T)/T$, compares the heat of combustion, ΔH_{C}, to the initial enthalpy of the mixture, $c_p T$.

Equation (3.24) implicitly assumes that a thermal explosion is the mechanism for ignition. For dilute strong ignition events in RCMs, chain branching is more likely the impetus for

ignition. However, since temperature is the primary inhomogeneity due to heat loss to the walls and radical concentrations are assumed to vary negligibly throughout the mixture, flame kernels likely result from thermal explosion. Hence, the scaling given in Eq. (3.24) is considered appropriate for this demarcation.

Using Eq. (3.22) and substituting the Zeldovich relation for the speed of the ignition front and the turbulent Damköhler number in the same manner as discussed in Sec. 2.2.1, the Sankaran criterion is found to be

$$\mathrm{Da_t} = \frac{\mathcal{T}_T^2 \mathcal{A}}{5\mathrm{Pr}\gamma\beta Y_\mathrm{F}} \exp\left(\mathcal{A}\frac{\beta}{\beta+1}\right) . \tag{3.26}$$

Hence, the Sankaran criterion is independent of the Reynolds number. However, additional dependence on the chemical kinetics beyond that encapsulated by the turbulent Damköhler number appears in explicit form via the Arrhenius factor. This indicates a potential difficulty with the regime demarcation in the region of negative temperature coefficient (NTC) for a given fuel. As the Arrhenius factor becomes less in the NTC region, the critical Damköhler number for mild ignition correspondingly lessens and potentially becomes negative. A negative Damköhler limit implies that mild ignition could occur from cold-spots; however in these cases, non-ideal ignition is more likely to occur within the thermal boundary layer. Hence, this demarcation should be viewed as a conservative estimate of where fuels show evidence of non-ideal ignition. Additionally, a compositional dependence is shown by the fuel mass fraction; however, for narrow ranges of equivalence ratio for a given fuel, this factor is not expected to appreciably affect the demarcation. The boundary given by Eq. (3.26) is shown in Fig. 3.2 and separates mild and mixed regimes.

2.2.3 Pre-ignition

Radical build-up during the compression stroke constrains RCMs to long test times [58]. Hence, a straight-forward demarcation of the regime where radical build-up and pre-ignition appreciably affect the measurement of ignition delay is a comparison of the compression time to the ignition delay:

$$\frac{\tau_\mathrm{comp}}{\tau_\mathrm{ign}} = 1 . \tag{3.27}$$

The compression time is related to the speed of piston by $\tau_\mathrm{comp} = L/U_\mathrm{P}$, where L is the stroke length. Substituting the relations for the turbulent Damköhler number, compression time, turbulent intensity, and C_l, Eq. (3.27) can be rewritten as

$$\mathrm{Da_t} = \frac{\mathcal{T}_u L}{\mathrm{C}_l d} . \tag{3.28}$$

For simple cylindrical geometry, this equation can be reformulated in terms of the aspect ratio, AR, and the compression ratio, CR:

$$\mathrm{Da_t} = \frac{\mathcal{T}_u}{\mathrm{C}_l}\mathrm{AR}(\mathrm{CR}-1) , \tag{3.29}$$

where the aspect ratio is the ratio of the length to the diameter of the test section, and the compression ratio is the ratio of the initial to the final volume of the test gas.

Considering the typical operational range of RCMs, this criterion is likely somewhat conservative. Also, much like heat transfer, the effect of radical build-up can be incorporated in modeling efforts to extend the operational range of facilities. However, the facility is ultimately limited by the occurrence of pre-ignition during the compression stroke. The boundary given by Eq. (3.29) is shown in Fig. 3.2. Damköhler numbers above this delineation indicate that radical build-up likely becomes a significant effect, and ultimately, where pre-ignition may occur during the compression stroke.

2.3 Heat transfer

RCMs operate in a long ignition delay time regime, which is amenable to measuring low-temperature chemical kinetics. Hence, heat loss to the walls of an RCM can significantly affect the measured ignition delay time due to an appreciable decrease in pressure and temperature. Heat loss is taken into account in the majority of models of RCM experiments via the "adiabatic core hypothesis" as discussed in the Introduction. Heat loss is typically deduced a posteriori through a non-reactive pressure-trace and the isentropic relation

$$\rho(t) = \rho_0 \left[\frac{p(t)}{p_0}\right]^{\frac{1}{\gamma}} , \tag{3.30}$$

where the subscript "0" indicates the time at TDC to avoid confusion in this subsection. Integrating Eq. (3.1) over the adiabatic core and incorporating the isentropic relation, given by Eq. (3.30), the model equation for RCMs with heat loss is thus

$$\rho c_v \frac{\mathrm{d}T}{\mathrm{d}t} + \sum_{i=1}^{N_\mathrm{s}} e_i \dot{\omega}_i = \frac{1}{\gamma}\frac{\mathrm{d}p(t)}{\mathrm{d}t} , \tag{3.31}$$

where the term on the right-hand-side is interpreted as the isentropic pressure work done by the expansion of the adiabatic core.

2.3.1 Thermal quenching

A reactive mixture may not ignite in an RCM experiment due to heat loss. A reactive mixture's propensity for thermal quenching can be estimated by first assuming an exponential decay of temperature in a representative mixture:

$$T = T_0 \exp\left(-\frac{t}{\tau_Q}\right) , \tag{3.32}$$

where τ_Q is the heat loss time constant, which in general can be estimated from the initial slope at the end of the compression of a pressure-trace from an RCM experiment. Equation (3.32) may be derived from the transient heat equation using isothermal walls and

truncating the resultant infinite series. Assuming simplified chemistry and the evolution of the temperature profile given by Eq. (3.32), Eq. (3.31) becomes

$$\frac{\mathrm{d}T}{\mathrm{d}t} = \frac{\Delta H_\mathrm{C}}{c_v} B Y_\mathrm{F} \exp\left(-\frac{E_\mathrm{A}}{\mathcal{R}T}\right) - \frac{T_0}{\tau_Q}\exp\left(-\frac{t}{\tau_Q}\right) \ . \tag{3.33}$$

Since the heat loss term is monotonically decreasing with temperature and the chemical source term is a decreasing function of temperature, it can be deduced that ignition is guaranteed to occur when the initial slope of the temperature derivative is zero. Using this criterion and evaluating Eq. (3.33) at the initial time, we have the following condition:

$$0 = \frac{\Delta H_\mathrm{C}}{c_v} B Y_\mathrm{F} \exp\left(-\frac{E_\mathrm{A}}{\mathcal{R}T_0}\right) - \frac{T_0}{\tau_Q} \ . \tag{3.34}$$

Noting that $\rho B Y_\mathrm{F} \exp\left(-E_\mathrm{A}/\mathcal{R}T_0\right) = \dot{\omega}_\mathrm{F}$, applying Eq. (3.24), and rearranging, Eq. (3.34) becomes:

$$\frac{\tau_Q}{\tau_\mathrm{ign}} = \mathcal{A} \ . \tag{3.35}$$

Assuming the relationship $\tau_Q = b^2/\alpha$, where b is the characteristic heat transfer length scale (taken to be the volume of the test section divided by its surface area), and applying the definition of the turbulent Reynolds number and the Prandtl number to Eq. (3.35), the thermal quenching limit is found to be:

$$\mathrm{Da_t} = (\mathrm{C}_l \mathrm{C}_Q)^2 \mathcal{A} (\mathrm{Pr Re_t})^{-1} \ , \tag{3.36}$$

where C_Q is a constant that relates the characteristic heat transfer length scale to the diameter of the RCM: $d = \mathrm{C}_Q b$. For example, C_Q for a right circular cylinder with a height equal to its diameter would be 1/6. The line given by Eq. (3.36) segregates the quenched and non-adiabatic regimes in Fig. 3.2 and has a slope of -1.

2.3.2 Loss of adiabaticity

A delineation of the regime where heat transfer effects become appreciable can be derived by examining the effect that the change in temperature has on the ignition delay. Assuming an Arrhenius form for the ignition delay, the following relation holds for small changes in temperature during the ignition process due to heat loss

$$\frac{\Delta \tau_\mathrm{ign}}{\tau_\mathrm{ign,0}} = -\mathcal{A}\frac{\Delta T}{T_0} \ , \tag{3.37}$$

where $\Delta\tau_\mathrm{ign}$ denotes the change in the ignition delay due to a change in temperature ΔT. Using the temporal change in temperature during an ignition process, given by Eq. (3.32),

to estimate the characteristic ignition temperature with heat loss, the change in temperature is given by

$$\Delta T = T_0 \exp\left(-\frac{\tau_{\text{ign}}}{\tau_Q}\right) - T_0 \ . \tag{3.38}$$

Substituting Eq. (3.38) into Eq. (3.37), the following is obtained:

$$\frac{\Delta\tau_{\text{ign}}}{\tau_{\text{ign},0}} = -\mathcal{A}\left[\exp\left(-\frac{\tau_{\text{ign}}}{\tau_Q}\right) - 1\right] \ . \tag{3.39}$$

Realizing that the heat loss time scale must be much larger than the ignition delay in cases where heat loss is negligible, the exponential term in Eq. (3.37) is approximated by the first two terms in the Taylor expansion giving

$$\frac{\Delta\tau_{\text{ign}}}{\tau_{\text{ign},0}} = \mathcal{A}\frac{\tau_{\text{ign}}}{\tau_Q} \ . \tag{3.40}$$

Using the same scaling as before for the heat transfer time scale, the demarcation for significant heat loss in RCM experiments is given by

$$\text{Da}_{\text{t}} = \frac{(\text{C}_l\text{C}_Q)^2}{\epsilon}\mathcal{A}(\text{PrRe}_{\text{t}})^{-1} \ , \tag{3.41}$$

where $\epsilon = \Delta\tau_{\text{ign}}/\tau_{\text{ign}}$, and is necessarily small for the aforementioned assumptions to hold. Hence, the division between the adiabatic and non-adiabatic regimes shows the same scaling as the thermal quenching demarcation. However, the former requires much larger Damköhler numbers than the latter since $\epsilon \ll 1$. Equation (3.41) separates the adiabatic and non-adiabatic regimes in Fig. 3.2, and has a slope of -1.

3 Discussion

A summary of the scaling relations is compiled in Table 3.1. This table confirms that the primary non-dimensional groups affecting the turbulent Damköhler number are the turbulent Reynolds number and the Arrhenius factor.

An interpretation of the turbulent Reynolds number is a ratio of viscous to turbulent time scales as shown in Eq. (3.5). Since the turbulent Damköhler number is proportional to the turbulent time scale, a slope of -1 in the regime diagram indicates an independence to turbulence of the demarcation. Hence, the turbulent Reynolds number shows substantial influence in determining the ignition character delineations.

3.1 Influence of the Arrhenius factor

The Arrhenius factor influences all of the demarcations besides the boundary for the quiescent regime. Assuming simplified chemistry, the logarithmic sensitivity of the species production

Demarcation	a	b	c	d	e
Quiescent/Turbulent	∞,-3.3	0	0	0	0
Pre-Ignition/Strong	0	0	0	0	0
Strong/Mixed	1/2	1	0	0	-1
Mixed/Mild	0	1	-1	1	0
Ignition/Quenching	-1	1	-1	0	0
Adiabatic/Non-Adiabatic	-1	1	-1	0	0

Table 3.1: Summary of the scaling relations found for the non-dimensional groups for the regime demarcation. Damköhler scaling has the form $\mathrm{Da_t} \sim \mathrm{Re_t}^a \mathcal{A}^b \mathrm{Pr}^c \beta^d \mathrm{M}^e$.

rate to temperature is given by

$$\frac{\partial \ln \dot{\omega}_\mathrm{F}}{\partial \ln T} = \mathcal{A} \ . \tag{3.42}$$

Hence, the Arrhenius factor is a parameter that indicates the sensitivity of the reaction chemistry to a perturbation in temperature. As discussed in the Introduction, the effect of the sensitivity of a mixture was studied by Meyer and Oppenheim [66] where it was found that strong-to-mild transition was delineated by an isopleth of ignition delay sensitivity. This criterion is given by

$$\frac{\partial \tau_\mathrm{ign}}{\partial T} = \mathrm{C_S} \ , \tag{3.43}$$

where $\mathrm{C_S}$ is determined from experiment for a given mixture. Rewriting the Sankaran criterion, given in Eq. (3.22), and applying Zeldovich's relation for the speed of the reaction front, the following relation results:

$$\frac{\partial \tau_\mathrm{ign}}{\partial T} = \left(\frac{\partial T}{\partial \xi} S_\mathrm{L} \right)^{-1} \ . \tag{3.44}$$

The qualitative similarity between Eqs. (3.43) and (3.44) is apparent. However, the two are distinct since the laminar flame speed of a mixture varies significantly with temperature and pressure. Mansfield *et al.* assumed a constant temperature gradient within RCMs; however, using the analysis outlined in Sec. 2.2.1 , the temperature gradient is found to have the following thermodynamic scaling:

$$\frac{\partial T}{\partial \xi} \sim (p T^{2-g})^{1/2} \ , \tag{3.45}$$

where the parameter g accounts for the scaling of the kinematic viscosity with temperature, which is typically between 1.5-2. Hence, the temperature gradient shows significant dependence on the thermodynamic conditions at top dead center in addition to the piston speed and the design of the RCM.

3.2 Comparison of the regime diagram to experiments

A comparison of the ignition quality demarcations derived in Sec. 2.2 is presented in Fig. 3.4. All ignition delay data except for the University of Michigan syngas data were taken directly from experiments. For this data, adiabatic, isochoric reactors using the Li *et al.* [50] C_1-mechanism at the specified thermodynamic conditions were used since significant deviation in the experimental ignition delay time from the reactor model is found for the mixed/DDT and the mild ignition cases. Additionally, the turbulent Reynolds and Damköhler numbers were computed using the relations specified in Sec. 2.1.3. The parameters $\mathcal{T}_u$ and C_l were taken to be 2% and 10%, respectively. Table 3.2 gives the machine-dependent parameters used to create Fig. 3.4.

Machine	d [cm]	U_P [m/s]	$\mathcal{T}_u^*$ [%]	C_l^* [%]	τ_t [ms]
Michigan [41]	5.08	30.0	2	10	8.47
Tsinghua [86]	5.08	16.7	2	10	15.2
Case Western [87]	5.08	6.64	2	10	38.2
NUI Galway [88, 89]	3.81	10.1	2	10	18.8

Table 3.2: Summary of the relevant machine-dependent parameters used to create Fig. 3.4. The turbulent time scale was estimated using Eq. (3.12). The piston velocity was either taken directly or calculated by dividing the stroke length of the RCM by the compression time. Quantities with an (*) were estimated.

Considering the highly stochastic nature of inhomogeneous ignition events, the regime diagram shows favorable agreement with the experimental data. The transition between the regimes is quite evident in the syngas data. However, the iso-octane data shows robustness in the mixed ignition regime; this is expected since two-stage ignition phenomena tend to homogenize the mixture, which decreases the propensity towards mixed or mild ignition [90]. Additionally, fuels such as iso-octane exhibit a decreasing Arrhenius factor as it approaches the NTC region; hence, the static demarcations with respect to the Arrhenius factor become increasingly conservative. The character of the ignition event is not reported for the NUI Galway and Case Western Reserve machines, but both are within the regimes where strong or mixed ignition is likely.

3.3 Mild ignition demarcation

The demarcation of mild ignition can be interpreted as the competition between heat dissipation and heat addition due to the reaction. For an ignition kernel, the competition between heat dissipation and chemistry is given by

$$\frac{\text{Dissipation}}{\text{Chemistry}} = \frac{\rho c_p \alpha \frac{\mathrm{d}^2 T}{\mathrm{d}\xi^2}}{\Delta H_C \dot{\omega}_F} = 1 \ , \tag{3.46}$$

where it can be seen that values of less than one lead to thermal ignition. Assuming symmetry at the center of the ignition kernel, $\mathrm{d}^2T/\mathrm{d}\xi^2 \approx 2T'/\lambda_T^2$ for small kernel sizes. Rearranging

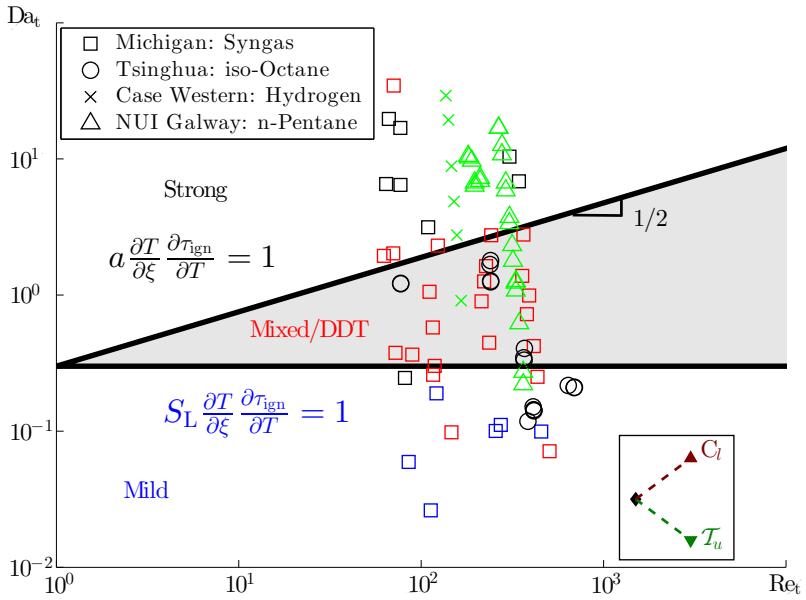

Figure 3.4: (Color online) Comparison of the demarcations of ignition quality to experiment. **BLACK** symbols indicate strong ignition, **RED** symbols indicate mixed/DDT ignition, **BLUE** symbols indicate mild ignition, and **GREEN** symbols indicate that the quality of ignition was not reported. □ taken from Mansfield *et al.* [73], ○ taken from Mansfield *et al.* [74], × taken from Mittal [87], and △ taken from Marks *et al.* [89]. The sensitivity of each point to a factor of two increase in the assumed parameters $\mathcal{T}_u$ and C_l is illustrated in the lower right corner.

Eq. (3.46) and expressing in terms of a turbulent Damköhler number, the following is obtained:

$$\mathrm{Da_t} = \frac{\gamma \mathcal{T}_T \mathcal{A}}{5\mathrm{Pr}} \ . \tag{3.47}$$

Hence, Eq. (3.47) shows that kernel formation is independent to the turbulent Reynolds number as in the Sankaran criterion. Additionally, Eq. (3.47) indicates that turbulence within the RCM has an ameliorating effect, reducing the propensity towards kernel formation. However, this demarcation would be present for turbulent Damköhler numbers low enough that heat transfer effects would likely dominate in the operational ranges of RCMs.

3.4 Adiabatic core hypothesis

The adiabatic core hypothesis is presumed to be valid in the modeling of heat transfer effects in RCMs. The adiabatic core hypothesis relies on the supposed isentropic expansion of the test gas within an RCM. However, it is shown that diffusive losses will cause this hypothesis to break down at long test times. Hence, there should be a critical thermal

boundary layer thickness, δ, in relation to the characteristic heat transfer dimension, b, such that this hypothesis is valid. Again, b is taken to be the combustion chamber's ratio of volume to surface area. For this critical value of the boundary layer thickness, the relationship to the ignition delay time is

$$\delta = \delta_0 + \sqrt{\alpha \tau_{\text{ign}}} \ , \tag{3.48}$$

where δ_0 is the size of the thermal boundary layer at TDC. Dividing through by b, squaring, and substituting the definitions of the turbulent Damköhler and Reynolds numbers, the criterion becomes

$$\text{Da}_\text{t} = \left(\frac{\delta - \delta_0}{b} \right)^{-2} (\text{C}_Q \text{C}_l)^2 (\text{PrRe}_\text{t})^{-1} \ , \tag{3.49}$$

where the ratio, $(\delta - \delta_0)/b$, is determined from experiments or more advanced heat-transfer models. Comparing this to the thermal quenching criterion given by Eq. (3.36), it appears that the invalidation of the adiabatic core hypothesis is unlikely to be a significant effect since mixtures without an NTC region will likely quench before this effect is appreciable. Therefore, this demarcation is not included in the representative comparison depicted in Fig. 3.2 since it is primarily designed for syngas mixtures. However, for mixtures within the NTC region, the adiabatic core hypothesis may break down before thermal quenching due to the decreased Arrhenius factor.

3.5 The operational range of a rapid compression machine

A comparison of the operational range of a representative RCM with a lean iso-octane mixture at several pressures is depicted in Fig. 3.5. The test duration is shown to be limited by the mild-ignition demarcation given by the Sankaran criterion and the prevalence of radical build-up during the compression stroke. The Sankaran criterion may be computed precisely using Eq. (3.22), substituting the Zeldovich relation for the speed of the ignition front, and estimating the temperature stratification; however for simplicity, a critical turbulent Damköhler number, $\text{Da}_{\text{t,crit}}$, of 0.3 is used since this value corresponded well to the experimental data given in Fig. 3.4. Additionally, the radical build-up limit illustrated in Fig. 3.5 may be computed more precisely using a realistic piston speed profile in conjunction with a variable volume reactor model, and estimating the error incurred in the ignition delay measurement by neglecting the compression stroke.

Within this operational range, heat transfer effects are expected to be significant, and the upper limit of the test times may approach the regime where the break down of the adiabatic core hypothesis and thermal quenching could occur. Also, the ejection of corner vortices into the core fluid may be present as well.

From Fig. 3.5 it is evident that the operational range of a rapid compression machine is dependent on the operating conditions of the machine; there is an implicit trade-off with respect to the piston speed; higher piston speeds allow for an increased operational range at higher temperatures due to the reduction of the compression time; however, higher piston

speeds can increase the gas dynamic fluctuations in the test gas [63, 64], which can lead to non-ideal ignition at lower temperatures. Hence, an effective test strategy could be to tailor the compression stroke with respect to the desired test-time to increase the operational range of the RCM.

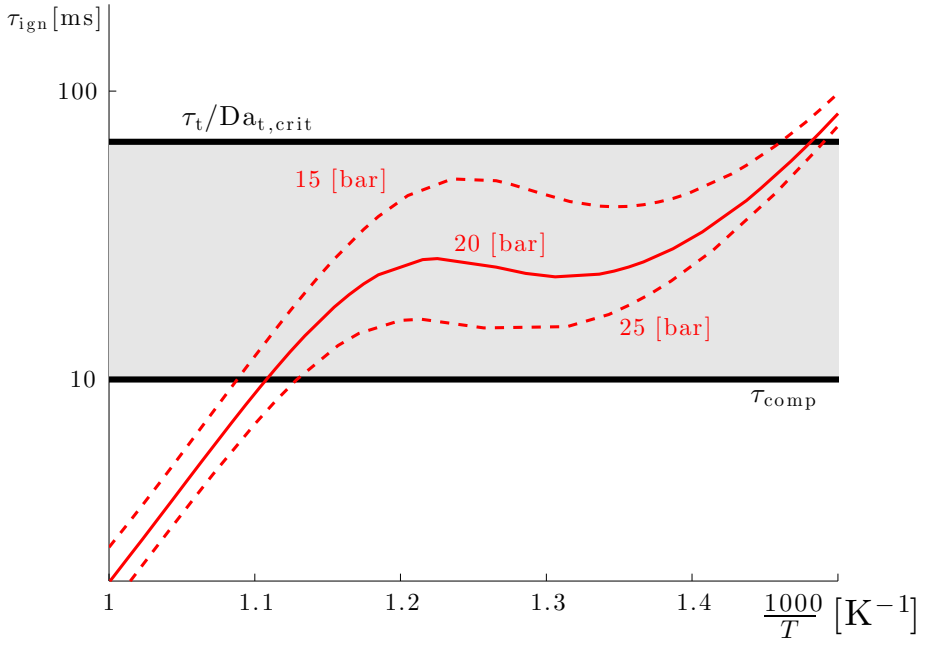

Figure 3.5: (Color online) Operational range of a representative RCM with respect to the mild ignition and radical build-up limits. The gray area highlights the operational limits for a machine with a compression time of $\tau_{\mathrm{comp}} = 10$ ms and a turbulence time scale of $\tau_{\mathrm{t}} = 20$ ms. The critical Damköhler number for the onset of mild ignition, $\mathrm{Da}_{\mathrm{t,crit}}$, is taken to be 0.3. The ignition delay curves of iso-octane are obtained from the reduced mechanism of Pepiot-Desjardins and Pitsch [61] at an equivalence ratio of 0.6.

Chapter 4

Effects of Flow-field and Mixture Inhomogeneities on the Ignition Dynamics in Continuous Flow Reactors

1 Introduction

The integrated gasification combined cycle (IGCC) process has been considered as viable technology for the syngas combustion in advanced power plants. In coal-based IGCC power plants, syngas – containing hydrogen (H_2) and carbon monoxide (CO) as primary fuel components – is generated through a coal gasification process [91]. After sulfur oxides and other pollutants are removed, the syngas is combusted in a gas turbine cycle, and excess heat is converted in a subsequent steam turbine cycle. Compared to conventional coal-fired power plants, IGCC-systems offer advantages for precombustion carbon capture and sequestration, significant reductions of emissions of pollutants and particulates, and the potential for higher thermal efficiencies.

However, despite the opportunities to achieve higher efficiencies and to reduce pollutant emissions, the stable operation of HHC-fuels in IGCC power plants introduces significant technological and scientific challenges. These challenges are primarily attributed to the lower density and higher diffusivity of hydrogen compared to conventional hydrocarbon fuels. These different thermo-diffusive properties lead to higher flame speeds, extended flammability limits, and lower ignition temperatures, which can adversely affect combustion stability and fuel conversion [7]. In addition, high flame temperatures associated with hydrogen combustion make NO_x emissions a concern, so that premixing and dilution strategies are required to reduce these emissions to acceptable levels [92].

Additional challenges arise from IGCC operating conditions that lie in the intermediate

temperature range (600–1000 K) and high-pressure regime (up to 30 bar). Recent experimental and computational investigations identified considerable discrepancies between measured and predicted ignition delay times at these conditions [12, 25, 93, 94]. Several reasons have been proposed to explain these discrepancies [1, 12, 25, 63], including (i) sensitivity of rate coefficients at high-pressure/low-temperature conditions, (ii) effects of inhomogeneities in the mixture composition and flow-field structure on the ignition characteristics in experimental facilities, (iii) catalytic effects of HHC-fuel mixtures due to contaminations with metal carbonyls and nitric oxides, (iv) the significance of thermo-viscous boundary layers, wall-heat-transfer, and (v) turbulent mixing. While many of these non-idealities are often specific to a particular experimental facility, it remains a major challenge to experimentally isolate and systematically quantify individual contributions.

Ignition delay measurements are commonly conducted in shock tubes (STs), rapid compression machines (RCMs), and continuous flow reactors (FRs). Flow reactors are of particular interest for ignition studies at gas-turbine relevant operating conditions, since these facilities provide access to extended test-times beyond 500 ms. Currently employed FR-facilities share a similar setup [53, 94–96]. In its simplest form, a flow reactor consists of a long pipe that is separated by a fuel injector module into a flow conditioner and a test section. Air is supplied from a pressurized tank through the flow conditioner in which the air is preheated. The fuel is subsequently injected via a mixing module, and different mixing strategies [97] are utilized to achieve an approximately homogeneous mixture prior to ignition. Following the mixing, the test-gas mixture passes down the test section in which autoignition takes place. To minimize heat losses and other secondary effects, the test section is commonly heated and thermally insulated. Thermocouples, photo-diodes, and pressure sensors are employed to detect the ignition location. The ignition location, x_{ig}, is then related to an ignition delay time, τ_{ig}, using the theoretical bulk flow velocity U_{b} [53, 98]:

$$\tau_{\mathrm{ig}} = \frac{x_{\mathrm{ig}}}{U_{\mathrm{b}}} \, . \tag{4.1}$$

To guarantee that the mixture ignites within the finite-length test section, mass flow rate and bulk velocity are adjusted, depending on the pressure and temperature conditions of the test gas mixture.

Flow-reactor studies of HHC-fuels at gas-turbine-relevant operating conditions [53, 94, 96] have shown that the ignition delay is primarily controlled by the hydrogen-content of the syngas-mixture and is linked to the H_2/O_2 explosion limit. These measurements also revealed that the ignition exhibits a pronounced sensitivity to initial conditions. Often, ignition could only be observed in some cases for nominally identical initial conditions [94] or ignition events occurred at different locations in the test section [96]. In the case of a successful ignition, the ignition event occurred earlier than predicted from homogeneous isobaric reactor simulations. These observations suggest that the ignition is not deterministic and most-likely dependent on facility-specific non-idealities that are present in the flow reactor. In particular, Beerer & McDonell [94] pointed out that the sources for these sporadic ignition events could be linked

to incomplete mixing between fuel and oxidizer, temperature variations in the preheater, turbulent mixing in the test-section, and the influence of the boundary layer in affecting the induction time and the ignition process. Therefore, a better understanding of the effects of inhomogeneities in temperature and mixture composition, and the role of the aerodynamics in affecting the ignition process is crucial towards the characterization of ignition properties of HHC-fuels.

The objective of this chapter is to assess the sensitivity of turbulent mixing and inhomogeneities in temperature and mixture composition on the observed ignition dynamics of HHC-mixtures. To this end, an idealized flow reactor configuration is considered that has the same geometric dimensions as the UTRC flow reactor facility [53]. The flow-field inside the flow-reactor is described by considering two different modeling approaches. In the first part, the spatio-temporal evolution of the mixture is represented by a particle method, and the high-pressure H_2/O_2 kinetic mechanism by Burke *et al.* [99] is used to describe the reaction chemistry. Effects of laminar and turbulent velocity profiles on the ignition are investigated. Motivated by previous experimental observations, the significance of inhomogeneities in temperature and mixture composition is then investigated, and results of this study are presented in Sec. 3. Because of the computational complexity of the particle method, a parabolized Eulerian model is developed in Sec. 4. This model assumes a stationary ignition-combustion process, which is described using a Reynolds-averaged approach. A tabulation method is used to describe the reaction chemistry. The computational efficiency of this model enables the consideration of an extended parameter space that is not accessible with the particle model. A time-scale analysis is performed, and three different ignition regimes are identified that can be associated with the competition between homogeneous ignition, flame-deflagration, and turbulent diffusion. Qualitative comparisons with experimental results, presented in Sec. 4.3, provide some evidence for the presence of premixed ignition regimes that are most prominent at low-temperature conditions.

2 Diagnostics and Ignition Criterion

The autoignition process in flow reactors is affected by the unsteady velocity field and the turbulent mixing. To analyze this stochastic ignition process, a statistical approach is considered. To this end, we define the probability density distribution (PDF), $\mathcal{P}(\psi; x, t)$, which is evaluated from a scalar field variable ψ and is a function of axial location x and time t. A cross-sectionally averaged quantity is then evaluated as:

$$\{\psi\}(x,t) = \int \psi \mathcal{P}(\psi; x, t) \mathrm{d}\psi \ . \tag{4.2}$$

By introducing the cumulative distribution function $\mathcal{C}$, the following ignition criterion can be defined:

$$\mathcal{C}(\psi_{\mathrm{ig}}; x, t) \equiv \int_{-\infty}^{\psi_{\mathrm{ig}}} \mathcal{P}(\psi; x, t) \mathrm{d}\psi \leq \mathcal{C}_{\mathrm{ig}} \ , \tag{4.3}$$

where

$$\psi_{\mathrm{ig}} = \alpha\psi \tag{4.4}$$

(with α being a parameter) is an ignition threshold – for instance a certain temperature increase at the thermocouple or the detected light-absorption at a photo-multiplier. The ignition location, x_{ig}, is then defined as the most-upstream location at which Eq. (4.3) is fulfilled. In this study, we consider the temperature ($\psi \equiv T$) to characterize the ignition location. In a separate investigation, OH and OH* were also considered as ignition markers, giving very similar results.

3 Lagrangian Flow Reactor Model

3.1 Mathematical Model

In this section, a particle-field method is employed to describe the autoignition of the fuel/air mixture inside the flow reactor test section. This method describes the spatio-temporal evolution of an ensemble of statistically independent notional particles through a three-dimensional flow-field. The spatial location and composition of the nth notional particle in this ensemble is, respectively, denoted by $\boldsymbol{x}^{(n)}$ and $\boldsymbol{\Phi}^{(n)} = (\boldsymbol{Y}^{(n)}, T^{(n)})^T$, with $\boldsymbol{Y}$ being the vector of all species mass fractions and T is the temperature. The particle position $\boldsymbol{x} = (x, y, z)^T$ is obtained from the solution of the following stochastic differential equation [47, 100]:

$$\mathrm{d}\boldsymbol{x}^{(n)} = \overline{\boldsymbol{u}}^{(n)}\mathrm{d}t + \sqrt{2\alpha_T^{(n)}}\,\mathrm{d}\boldsymbol{W}^{(n)}\,, \tag{4.5}$$

where $\mathrm{d}W^{(n)}$ is a Wiener process, $\alpha_T^{(n)}$ is the turbulent diffusivity, and $\overline{\boldsymbol{u}}^{(n)}$ is the time-dependent filtered velocity vector, which is obtained from a three-dimensional unsteady large-eddy simulation. The evolution of the particle composition is described by the following Lagrangian equation:

$$\mathrm{d}_t\boldsymbol{\Phi}^{(n)} = \Omega_{\mathrm{m}}\left[\langle\boldsymbol{\Phi}\rangle - \boldsymbol{\Phi}^{(n)}\right] + \boldsymbol{\omega}(\boldsymbol{\Phi}^{(n)})\,. \tag{4.6}$$

The first term on the right-hand-side (RHS) of this equation describes the mixing and is modeled using an IEM (interaction by exchange with the mean) model [47]. The mixing frequency is evaluated as [101]:

$$\Omega_{\mathrm{m}} = \frac{C_\Phi}{2}\frac{C_\Omega(\alpha + \alpha_T)}{\Delta^2}\,, \tag{4.7}$$

where Δ is the filter-size of the underlying LES-computation, and C_Φ and C_Ω are modeling constants that take values of 2 and 3, respectively. The second term on the RHS of Eq. (4.6) represents the vector of source terms of reaction rates and heat-release, which are evaluated from a detailed chemical mechanism.

In this context it is noted that the homogeneous reactor model is recovered by setting Ω_m to zero in Eq. (4.6). Furthermore, by using $\overline{\boldsymbol{u}} = U_\mathrm{b}\widehat{\boldsymbol{e}}_x$ (with $\widehat{\boldsymbol{e}}_x$ being the unit-vector in stream-wise direction) and omitting the stochastic particle motion in Eq. (4.5) the canonical flow reactor formulation of Eq. (4.1) is obtained.

The objective of this work is to characterize effects of the unsteady flow field and inhomogeneities in mixture composition and temperature on the ignition dynamics of the test gas mixture. Notional particles are advected by an irrotational velocity field, which is obtained from the solution of a three-dimensional large-eddy simulation (LES). This unsteady turbulent flow-field is passive and not affected by density changes. This, however, appears to be an appropriate assumption since this investigation is concerned with studying the ignition onset for which density changes and heat-release remain small. As such, the present study is consistent with experimental investigations, in which dilatational effects are also neglected. The error that is introduced by neglecting these effects can be estimated by considering a control volume $V_0 = \pi R^2 x_0$ over which the temperature increases linearly from T_0 to $T_\mathrm{ig} = \alpha T_0$. By assuming homogeneous species composition, the difference in the ignition location can then be evaluated as:

$$\frac{x_\mathrm{ig}}{x_0} = \frac{\alpha - 1}{\ln(\alpha)} \,. \tag{4.8}$$

In the following parametric investigation we consider $\alpha = 1.1$, resulting in a shift in the ignition location by less than 5%. While this analysis does not account for other thermochemical processes, it can be assumed that the constant-density approximation has no first-order effect on the predicted ignition-delay.

In this context it is noted that this model requires extensions for studying the post-ignition behavior or flame-structure. For these conditions the coupling of heat-release-induced density changes to the flow-field cannot be neglected and localized mixing models should be used in favor of the IEM-closure that is employed in the present study.

3.2 Flow Reactor Configuration

In the present investigation a generic flow reactor configuration is considered that has comparable geometric dimensions than the UTRC flow reactor facility [53]. The computational model consists of a pipe with a length of 2 m and a constant-area cross section, having a radius of $R = 2.2$ cm. The simulation domain includes the flow reactor test section, and begins a short distance downstream of the fuel injector.

The mixing characteristics of different fuel injectors has been investigated experimentally and computationally [53, 95, 96]. Santoro [96] performed acetone PLIF-measurements for different fuel/air momentum ratios. These measurements showed a nearly homogeneous mixture composition in the FR-core, and stratification in the wall-near region. From these PLIF-measurements a mixture distribution was evaluated that is used to specify the scalar composition at the inlet of the computational domain. The experimentally-determined PDF, which is shown in Fig. 4.1, is approximated by a mapped beta-distribution, having the

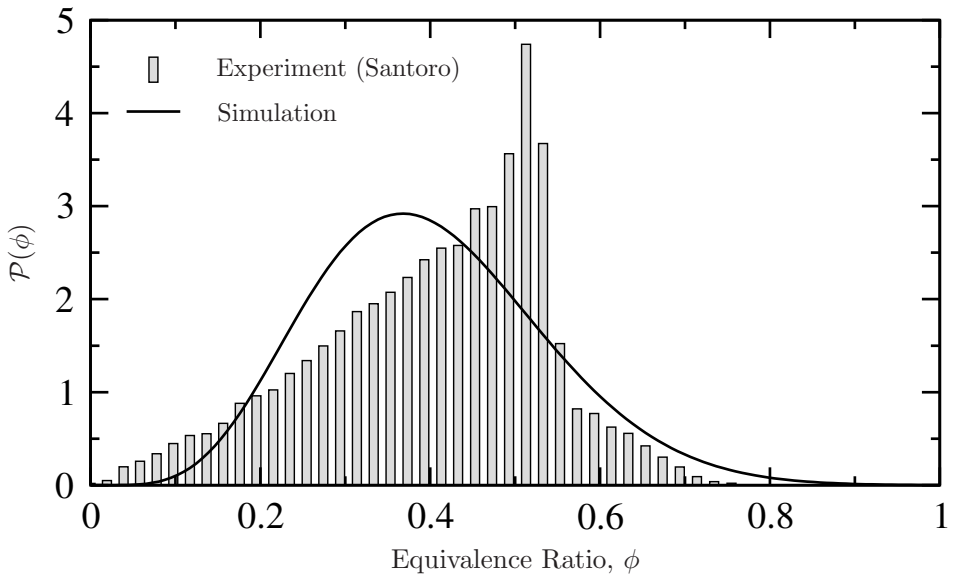

Figure 4.1: Mixture distribution downstream of the fuel-injector. The PDF is evaluated from acetone PLIF-measurements by Santoro [96] and approximated by a mapped beta-distribution; experiments were performed with hot air and a preheated mixture of N_2, He, and vaporized acetone at ambient pressure, and a momentum ratio of nine.

same mean and variance with $\{\phi\} = 0.4$ and $\{\phi'^2\} = 1.82 \times 10^{-2}$ as evaluated from these measurements. The composition of the particles entering the flow reactor test section are then sampled from this distribution. Note that in the absence of quantitative experimental data, the selection of these inflow conditions ignores the radial dependence of the scalar distribution. Measurements are necessary to provide qualitative information about boundary conditions, which are expected to be facility-specific.

Apart from few exceptions, flow reactors are commonly operated in a turbulent flow-regime with Reynolds numbers of the order of $\mathcal{O}(10^5)$. To accurately represent this flow-regime, two Reynolds-numbers with $\mathrm{Re} = 10^4$ and 10^5 are considered in this study. Here, the Reynolds number is defined with respect to the radius and bulk-velocity: $\mathrm{Re} = U_\mathrm{b} R/\nu$. The three-dimensional turbulent flow field is obtained from the time-dependent solution of a wall-resolved LES. In addition, results from flow reactor simulations will be presented, in which the velocity-field is prescribed by a Hagen-Poiseuille flow and an idealized constant plug-flow profile. Comparisons of the different mean velocity profiles that are used for the following simulations are presented in Fig. 4.2, showing the normalized mean axial velocity as function of radius r/R. Reported experimental data by Beerer & McDonell [94] are shown for comparison.

Since the experimental investigations showed that the ignition of syngas is primarily controlled by the hydrogen-content, we consider a lean H_2/air mixture. The reaction chemistry is described using the updated H_2/O_2 kinetic model of Burke *et al.* [99]. The mean equiv-

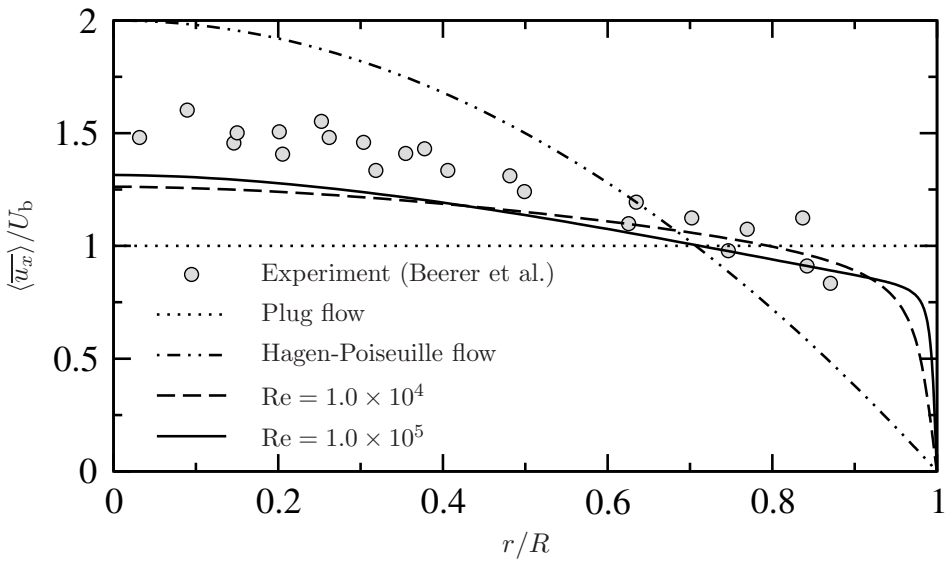

Figure 4.2: Mean axial velocity profiles as function of normalized radius in the flow reactor. Velocity-fields for two different Reynolds numbers are obtained from three-dimensional large-eddy simulations; measurements by Beerer & McDonell [94] and stationary profiles for plug-flow and laminar pipe-flow are shown as reference.

alence ratio of the mixture is $\{\phi\}_0 = 0.4$, the initial mean temperature of the mixture is $\{T\}_0 = 850$ K, and the pressure is $\{p\}_0 = 20$ bar. More than 5 million particles are used in the simulation to ensure that the results are insensitive to the particle density.

3.3 Results

In the following, a parametric study is conducted to investigate how the velocity field, turbulence intensity, and initial perturbations in mixture composition and temperature affect the ignition of the test-gas mixture in the flow reactor. These results are analyzed using the diagnostics that was introduced in Sec. 2.

3.3.1 Effect of Velocity Field

The effect of the unsteady velocity field on the ignition process is studied by considering four different flow-fields, namely a plug-flow, a parabolic mean flow, and two fully developed turbulent pipe-flow profiles at Reynolds numbers of 10^4 and 10^5. For all cases, the initial mixture composition and temperature are kept constant and identical to the nominal values that were given in the previous section.

Cross-sectionally averaged temperature profiles for these four configurations at different times are presented in Fig. 4.3. In these figures, the red curves indicate the ignition-state that is defined through the ignition criterion of Eq. (4.3) with $\mathcal{C}_\mathrm{ig} = 0.99$ and $T_\mathrm{ig} = 950$ K.

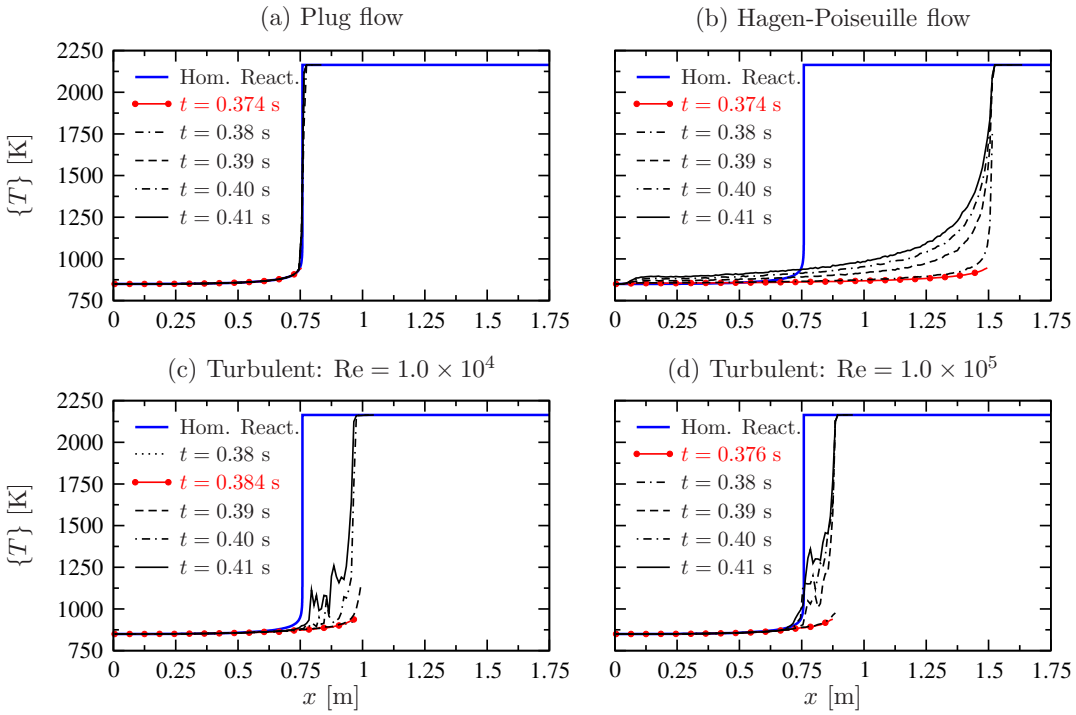

Figure 4.3: Cross-sectionally averaged temperature profiles at different time-instances for (a) plug flow, (b) laminar-parabolic mean flow, and fully developed turbulent pipe flow at (c) Re $= 1.0 \times 10^4$ and (d) Re $= 1.0 \times 10^5$; red curves indicate the ignition state, and blue curves correspond to results of an idealized homogeneous reactor simulation; H_2/air-mixture with $\{\phi\}_0 = 0.4$, $\{T\}_0 = 850$ K, and $\{p\}_0 = 20$ bar.

The black lines correspond to results at later time-instances that are separated by 10 ms. For comparison, results from a homogeneous isobaric reactor simulation are shown in blue. Results for the plug-flow velocity profile are in very good agreement with the homogeneous reactor model, and time and location of the ignition matches the zero-dimensional simulation results. The ignition behavior obtained from the laminar-parabolic mean-flow exhibits a distinctly different behavior. The ignition location is shifted downstream. This is attributed to the higher centerline velocity, which is a factor of two larger than the bulk-velocity. Profiles at slightly later time-instances show a rapid temperature increase upstream of the primary ignition location. Reason for this is the extended residence time that increases quadratically with the distance to the wall. After the ignition in this wall-near region is initiated the flame propagates away from the wall towards the FR core-region, resulting in the rapid temperature increase. A snap-shot of the instantaneous particle field at $t = 0.4$ s is shown in the upper part of Fig. 4.4. Less than 5 % of all particles are shown, and the particles are scaled and colored by the instantaneous particle temperature. From the mean temperature profiles of Fig. 4.3(b) it is also evident that the induction prior to the ignition – even in the absence of mixture and temperature inhomogeneities – is affected by the flow-field. This provides

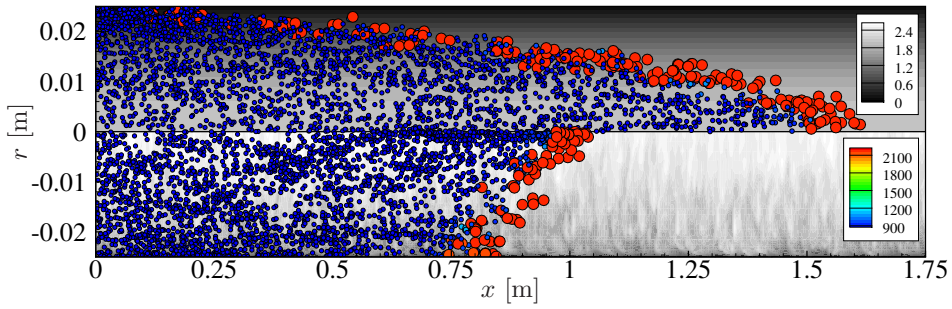

Figure 4.4: Instantaneous particle-distribution at $t = 0.4$ s for the laminar-parabolic mean flow (top) and fully-developed turbulent flow at $\mathrm{Re} = 1.0 \times 10^4$ (bottom); axial velocity is shown in gray-scale, and particles are scaled and colored by temperature.

computational support of previous mixing-investigations by Gokulakrishnan *et al.* [102].

Results for the particle ignition in a fully developed turbulent flow at two Reynolds numbers are shown in the bottom panels of Fig. 4.3, and the instantaneous particle temperature field for the configuration with $\mathrm{Re} = 1.0 \times 10^4$ is presented in the bottom of Fig. 4.4. A comparison with the homogeneous reactor-results shows that the ignition location is extended downstream by approximately 25 %, and x_{ig} moves upstream with increasing turbulence level. From Fig. 4.4 it is also evident that the ignition front is narrower than seen for the parabolic mean-flow solution. The cross-sectionally averaged temperature profiles also suggest the presence of localized autoignition events upstream of the primary ignition front. These localized ignition events rapidly increase in number as time progresses.

3.3.2 Effect of Composition and Temperature Variations

In this section, effects of initial inhomogeneities in mixture composition and temperature on the ignition process are investigated. The fully developed turbulent pipe-flow with $\mathrm{Re} = 1.0 \times 10^4$ is considered as velocity field. The initial species composition is sampled from the mapped PDF that is derived from the experimental data and shown in Fig. 4.1.

It was pointed out by Peschke & Spadaccini [53] that the ignition exhibits a pronounced sensitivity to the mixture temperature. Electric heaters are commonly used for preheating the air. Some facilities also employ a separate heater for preheating the fuel [94]. To prevent the decomposition of the fuel prior to ignition the temperature of the injected fuel is typically lower than that of the incoming air-stream [94].

Although Santoro [96] performed temperature measurements in the FR-test section – reporting a uniformity of the *mean*-temperature within ±5 K – the *instantaneous* temperature field at the fuel injector exit has so far not been measured. To assess the influence of potential temperature perturbations that, for instance, can be induced by unsteady heating, turbulent heat-transfer from the heater to the air-stream, or localized hot-spots or heat-losses, a series of simulations is conducted in which different levels of temperature perturbations are

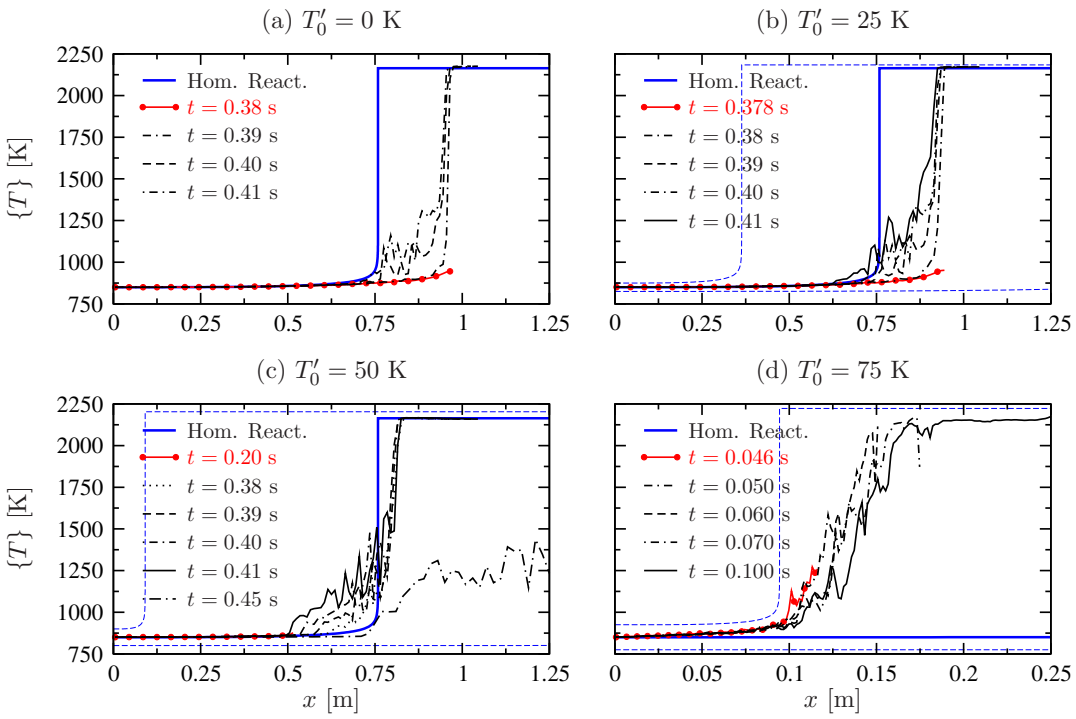

Figure 4.5: Cross-sectionally averaged temperature profiles at different time-instances for (a) $T_0' = 0$ K, (b) $T_0' = 25$ K, (c) $T_0' = 50$ K, and (d) $T_0' = 75$ K; red curves indicate the ignition state, and blue curves correspond to results of an idealized homogeneous reactor simulation; blue dashed lines represent homogeneous reactor results in which the initial temperature is set to $\{T\}_0 \pm T_0'$; H_2/air-mixture with $\{\phi\}_0 = 0.4$ and $\phi_0' = 0.135$, $\{T\}_0 = 850$ K, and $\{p\}_0 = 20$ bar.

prescribed at the inlet of the computational domain. In the following, five configurations are considered that differ only by the initial particle temperature distribution. The particle temperature is sampled from a Gaussian PDF with a mean temperature of 850 K, and temperature fluctuations between 0 and 100 K are considered.

Results for the spatio-temporal evolution of cross-sectionally averaged temperature profiles for different initial values of temperature fluctuations are illustrated in Fig. 4.5. To provide a qualitative comparison of these simulation results with homogeneous reactor simulations, we also present results in which the initial temperature is specified as $\{T\}_0 \pm T_0'$ (corresponding to one standard deviation). These results are shown by blue dashed curves in Fig. 4.5. From this comparison it can be seen that the ignition process is unaffected by temperature inhomogeneities below approximately 25 K. However, with increasing levels of temperature fluctuations the ignition location moves upstream. An analysis of the temperature PDF and instantaneous particle trajectories showed that this is caused by stochastic ignition events that are initiated from hot particles near the boundary layer. This is further illustrated in Fig. 4.6, showing the temperature PDF at the time $t = 0.4$ s. The black solid

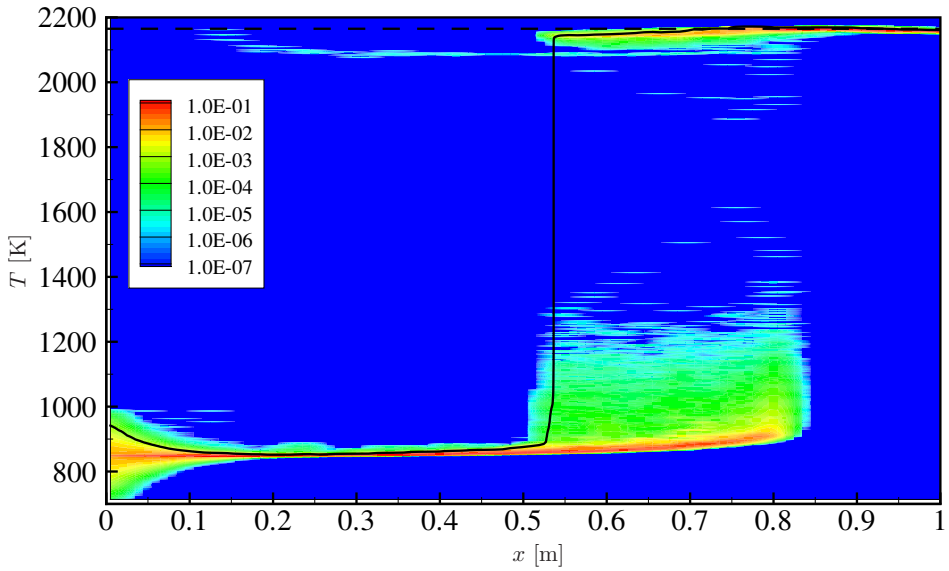

Figure 4.6: Temperature PDF, $\mathcal{P}(T;x,t)$, at $t = 0.4$ s for the case with $T_0' = 50$ K; the black solid line identifies the ignition criterion (Eq. (4.3)) and the dashed line shows the equilibrium temperature.

line identifies the ignition location via the criterion of Eq. (4.3) and the dashed line corresponds to the equilibrium temperature. From this figure it can be seen that within the first 15 cm the initial temperature inhomogeneities decay due to the enhanced turbulent mixing. However, high-temperature particles that are located in the boundary-layer are less affected by the turbulent mixing process, and therefore retain their enthalpy and act as localized ignition spots. This can be seen from Fig. 4.7, comparing the instantaneous particle temperature field for the cases with $T_0' = 0$ K (top view) and $T_0' = 75$ K (bottom view). From these results the presence of ignition kernels upstream of the reaction front and in the vicinity of the boundary layer for the case with strong temperature perturbations is evident. This figure also shows a nearly planar flame-front for the case with $T_0' = 75$ K, which is a result of the turbulent mixing and reduced ignition delay, moving the ignition location closer to the fuel injector.

The suppressed mixing process in the boundary layer can also explain why spontaneous ignition is typically observed in the wall-near region. This observation would also suggest that, in the presence of large temperature-perturbations, an active cooling of the reactor-wall (as utilized in Ref. [53]) might mitigated these spontaneous ignition events.

These parametric studies also show that the reduction in the ignition delay becomes increasingly sensitive to temperature perturbation above $T_0' = 50$ K. This is illustrated in Fig. 4.5(d), showing results for a case with inlet temperature perturbations of 75 K. For this case, the ignition time and location is reduced by a factor of four compared to the case with $T_0' = 50$ K. The cross-sectionally averaged temperature profiles exhibit pronounced temperature variations, which can be attributed to the distributed ignition region and localized

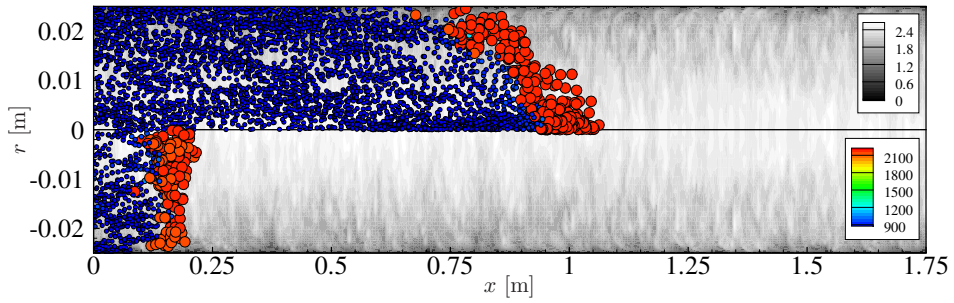

Figure 4.7: Instantaneous ignition process in flow reactor, showing (top) particle-distribution at $t = 0.4$ s for a homogeneous temperature field and (bottom) distribution at $t = 0.08$ s for the case with $T_0' = 75$ K, showing the presence of stochastic ignition events upstream of the main flame front; turbulent velocity field at $\mathrm{Re} = 10^4$ is shown in gray-scale, and particles are scaled and colored by temperature.

ignition events.

3.4 Discussion

The Arrhenius plot in Fig. 4.8 summarizes the main results from this investigation, showing the ignition delay time as function of the initial temperature. Measurements are shown by black symbols, and the simulation results obtained from the particle method are presented by the colored symbols. The dashed line corresponds to homogeneous reactor results. These results show that, in the case of an initially homogeneous mixture, the particle ignition process is fairly insensitive to the underlying flow-field. Under these conditions the ignition location can directly be related to the particle residence time, and is therefore only dependent on the particle velocity. By considering initial temperature fluctuations, the results indicate that the ignition process exhibits a strong sensitivity to temperature perturbations. For the operating conditions that are investigated in this study, it was observed that ignition is initiated in the boundary layer.

In a separate study, the effect of compositional variations was investigated by considering the special case of a homogeneous mixture (that is $\mathcal{P}(\phi) \rightarrow \delta(\phi - \{\phi\}_0)$) and $T_0' = 50$ K. For this limiting case, we did not observe any significant changes in the ignition location, indicating that the ignition point exhibits a greater sensitivity to temperature perturbations. As such, the ignition behavior of this weakly perturbed mixture composition is different from autoignition in non-premixed and partially-premixed flames [103], in which ignition is initiated at conditions corresponding to the most-reactive equivalence ratio (or mixture fraction) and local strain.

The present study is limited to a single mean-temperature condition due to the computational expenses of the particle method. Furthermore, this study only provides indirect insight in relevant time-scales of competing physical processes that are associated with scalar and turbulent mixing, induction chemistry, and flame-propagation. These aspects will be

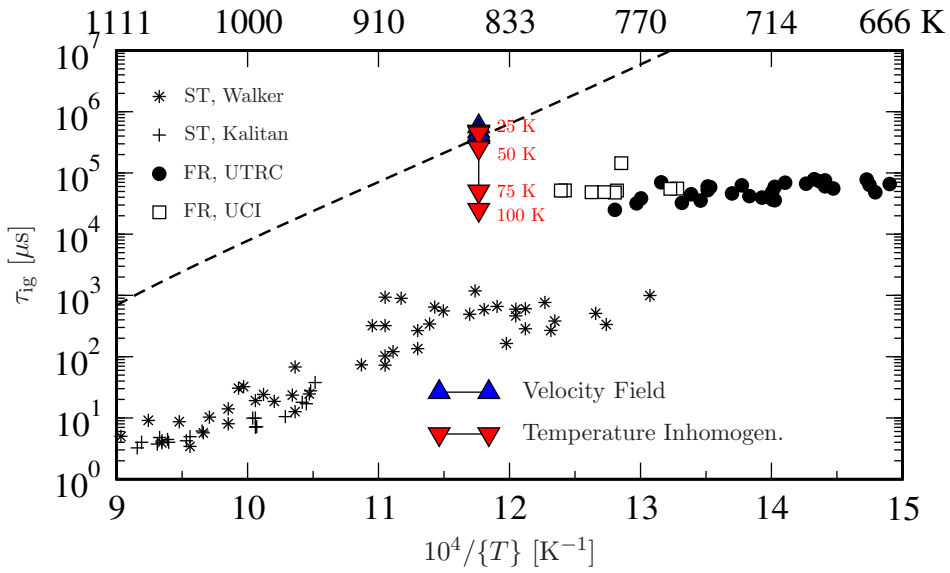

Figure 4.8: Comparison of computed and measured ignition delays for hydrogen/air mixtures. Measured ignition delays from shock tubes (ST) and flow reactors (FR) are adjusted to a pressure of 20 bar; the dashed line shows results of homogeneous reactor computation.

addressed in the following section by considering a computationally efficient parabolized model-formulation.

4 Parabolized Eulerian Flow Reactor Model

This section complements the Lagrangian analysis and a parabolized Eulerian model is developed to describe the flow-reactor ignition behavior over a wider range of operating conditions. Compared to the Lagrangian approach this method utilizes a three-scalar statistical approach, resulting in a computationally efficient model that can be employed for engineering design analyses of flow-reactors. This model enables the exploration of a larger parameter space that is not accessible using the Lagrangian formulation. This model exploits the fact that diffusive transport along the upstream axial direction is negligible due to the intrinsic reactor design [53]. The turbulence/chemistry coupling and compositional inhomogeneities are presented using a PDF-closure in conjunction with a tabulated chemistry formulation, and the reaction rates are obtained from homogeneous reactor simulations. The turbulent velocity field is evaluated from the large-eddy simulation that was also used in the Lagrangian model.

4.1 Mathematical Model

The following model considers the spatial evolution of a stationary flow-field inside a flow-reactor. The governing equations, describing the conservation of mean and variance of mixture fraction Z, reaction progress variable C, and chemical and sensible enthalpy h, are approximated in the high Reynolds number limit so that molecular transport and diffusion along the stream-wise direction can be omitted (since $\partial_x^2 \sim \mathrm{Re}\,\partial_r^2$). Written in cylindrical coordinates, the resulting parabolized equations can then be written as:

$$\overline{\rho}\widetilde{u}\partial_x\widetilde{Z} = \frac{1}{r}\partial_r\left(r\alpha_T\partial_r\widetilde{Z}\right), \tag{4.9a}$$

$$\overline{\rho}\widetilde{u}\partial_x\widetilde{C} = \frac{1}{r}\partial_r\left(r\alpha_T\partial_r\widetilde{C}\right) + \overline{\rho\omega_C}, \tag{4.9b}$$

$$\overline{\rho}\widetilde{u}\partial_x\widetilde{h} = \frac{1}{r}\partial_r\left(r\alpha_T\partial_r\widetilde{h}\right), \tag{4.9c}$$

$$\overline{\rho}\widetilde{u}\partial_x\widetilde{Z''^2} = \frac{1}{r}\partial_r\left(r\alpha_T\partial_r\widetilde{Z''^2}\right) + 2\alpha_T\left(\partial_r\widetilde{Z}\right)^2 - C_\phi\frac{\mu_T}{\Delta^2}\widetilde{Z''^2}, \tag{4.9d}$$

$$\begin{aligned}\overline{\rho}\widetilde{u}\partial_x\widetilde{C''^2} =& \frac{1}{r}\partial_r\left(r\alpha_T\partial_r\widetilde{C''^2}\right) + 2\alpha_T\left(\partial_r\widetilde{C}\right)^2 - C_\phi\frac{\mu_T}{\Delta^2}\widetilde{C''^2} \\ &+ 2\overline{\rho}\widetilde{\omega_C''C''},\end{aligned} \tag{4.9e}$$

$$\overline{\rho}\widetilde{u}\partial_x\widetilde{h''^2} = \frac{1}{r}\partial_r\left(r\alpha_T\partial_r\widetilde{h''^2}\right) + 2\alpha_T\left(\partial_r\widetilde{h}\right)^2 - C_\phi\frac{\mu_T}{\Delta^2}\widetilde{h''^2}, \tag{4.9f}$$

where α_T is the turbulent diffusivity, which is assumed to be equal for all scalars, and determined from the Schmidt-number relation: $\alpha_T = \mu_T/\mathrm{Sc}_T$ with $\mathrm{Sc}_T = 0.7$. The scalar-to-mechanical time scale is set to the standard numerical value of $C_\phi = 2$, and Δ is the filter-size. The turbulent viscosity $\mu_T(r)$ and the axial velocity-component $\widetilde{u}(r)$ are obtained by averaging the three-dimensional unsteady LES-results over homogeneous directions. The unclosed chemical source term $\widetilde{\omega_C}$ and the progress-variable/source-term correlation $\widetilde{\omega_C''C''}$ are described using a presumed joint PDF:

$$\widetilde{\omega_C} = \iiint \omega_C(Z,C,h)\widetilde{P}(Z,C,h)dZdCdh, \tag{4.10a}$$

$$\begin{aligned}\widetilde{C''\omega_C''} =& \iiint\left[C-\widetilde{C}\right]\left[\omega_C(Z,C,h)-\widetilde{\omega_C}\right] \\ &\times\widetilde{P}(Z,C,h)dZdCdh,\end{aligned} \tag{4.10b}$$

and ω_C is precomputed from constant-pressure homogeneous reactor (HR) simulations. The progress variable is defined from the water mass fraction, resulting in a unique parameterization of the HR-ignition trajectories.

Since Z, C, and h are independent, the joint PDF can be represented in terms of marginal PDFs for each scalar. In the following, it is assumed that each scalar is represented by a

beta-distribution, so that the presumed PDF can be written as:

$$\widetilde{P}(Z,C,h) = \frac{\overline{\rho}^2}{\rho^2}\beta(Z;\widetilde{Z},\widetilde{Z''^2})\beta(C;\widetilde{C},\widetilde{C''^2})\beta(h;\widetilde{h},\widetilde{h''^2}) \;, \tag{4.11}$$

for

$$Z \in [0,1] \;, \qquad C \in [0,C_{\mathrm{eq}}] \;, \qquad h \in [0,1.5\widetilde{h}] \;, \tag{4.12}$$

and

$$\beta(\phi;\widetilde{\phi},\widetilde{\phi''^2}) = \frac{\Gamma(a+b)}{\Gamma(a)\Gamma(b)}(\phi-\phi^-)^{a-1}(\phi^+-\phi)^{b-1}(\phi^+-\phi^-)^{1-a-b} \;, \tag{4.13}$$

where $\phi \in [\phi^-,\phi^+]$, Γ is the Gamma function, and

$$a = \frac{\widetilde{\phi}-\phi^-}{\phi^+-\phi^-}\gamma \;, \quad b = \frac{\phi^+-\widetilde{\phi}}{\phi^+-\phi^-}\gamma \;, \quad \gamma = \frac{(\widetilde{\phi}-\phi^-)(\phi^+-\widetilde{\phi})}{\widetilde{\phi''^2}} - 1 \;. \tag{4.14}$$

The system of parabolic partial differential equations represents an initial value problem that is solved by integration along the axial direction. The computational domain in radial direction is discretized using a second-order central differencing scheme, and the radial mesh is identical to that of the LES-computation (consisting of 400 grid-points with $\Delta r/R = 1.0\times10^{-2}$ at the centerline and $\Delta r/R = 3.4\times10^{-4}$ at the wall). A splitting scheme is used to integrate the non-stiff radial diffusion operators and the chemically stiff reaction source term. For storage-reasons, the computational source-terms are directly evaluated during the computation, and the turbulent diffusivities and mean velocity are obtained from the LES-mean-flow results. Comparisons with homogeneous reactor results and grid-convergence studies have been performed to confirm grid-independence of the simulation results.

4.2 Results

The following section extends the analysis of Sec. 3.3 by considering a wider range of operating conditions. The initial mean temperature and its fluctuation vary between 700 and 1200 K and between 0 and 100 K, respectively. The mean and the variation of the scalars at the inlet follow uniform profiles in radial-direction without the consideration of mixture inhomogeneities. The results are analyzed using the diagnostics that was introduced in Sec. 2, with $\mathcal{C}_{ig} = 0.99$ and $T_{ig} = 1.1T_0$.

Profiles of the spatial evolution of the progress variable for four different initial temperature conditions are illustrated in Fig. 4.9. For these simulations, a homogeneous mixture composition without fluctuations are prescribed at the inlet. Using the expression $t = x/U_{\mathrm{b}}$, the axial distance is transformed into a temporal coordinate, and t is normalized by the ignition delay of the 0D homogeneous reactor simulation, τ_{HR}. The solid curve denotes the ignition front of the homogeneous reactor simulation in the absence of radial transport, $\tau_{\mathrm{ig}} = x_{\mathrm{ig}}(r)/\widetilde{u}(r)$. With increasing temperature, the chemical time-scale decreases so that

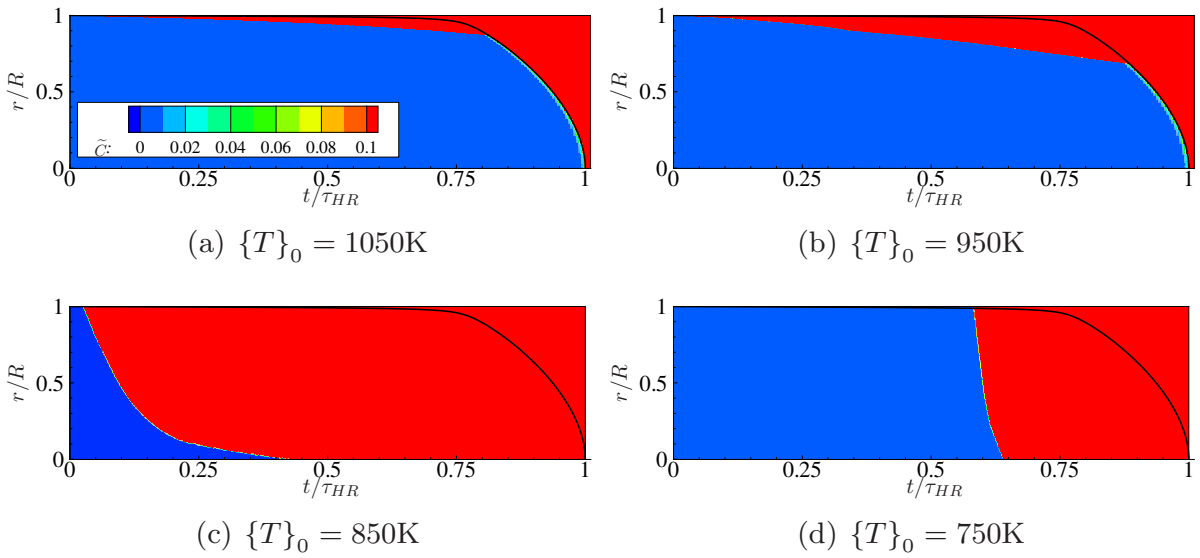

Figure 4.9: Mean profile of the progress variable for (a) $\{T\}_0 = 1050\,\mathrm{K}$, (b) $\{T\}_0 = 950\,\mathrm{K}$, (c) $\{T\}_0 = 850\,\mathrm{K}$, and (d) $\{T\}_0 = 750\,\mathrm{K}$; initial temperature fluctuation is set to zero; black curves indicate the ignition front of the homogeneous reactor and the time is normalized by the ignition-delay time of the homogeneous reactor under the corresponding condition; $\mathrm{Re} = 1.0 \times 10^5$, H_2/air-mixture with $\{\phi\}_0 = 0.4$, and $\{p\}_0 = 20$ bar.

turbulent transport becomes insignificant. In this high-Damköhler limit, the flow-reactor can be adequately represented by an assembly of isolated plug-flow reactors that evolve with the local velocity $\widetilde{u}(r)$. This can be seen in Fig. 4.9(a), showing that the predicted ignition front agrees with the plug-flow reactor results (solid curve). However, with reduced initial temperature, the importance of the turbulent transport increases, resulting in a reduction in the ignition location as shown in Figs. 4.9(b)–4.9(d). The competition between convection, diffusion, and reaction progress will be further investigated in the context of a time-scale analysis in the following section.

Effects of initial temperature fluctuations and Reynolds-number on the ignition delay are presented in Fig. 4.10. These simulations are performed without considering inhomogeneities in mixture composition. Initial conditions for enthalpy are evaluated from the prescribed temperature condition. In agreement with the results from the Lagrangian particle method, the parabolized Eulerian model shows that the initial temperature perturbation can significantly accelerate the ignition process and the ignition delay becomes more sensitive to the temperature perturbation as T_0' increases. Effects of the Reynolds number are only prominent at low temperature fluctuations, and differences decrease with increasing level of T_0' due to the enhanced turbulent mixing and early ignition onset. However, it is expected that the impact of the Reynolds number on the ignition onset would be more pronounced for turbulent premixed combustion, which is only incompletely represented with this model formulation. This will be further investigated in the next section.

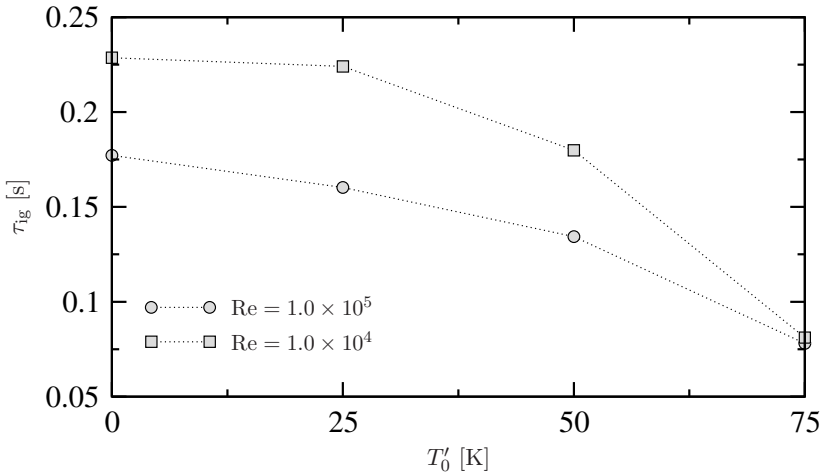

Figure 4.10: Comparison of ignition delay times predicted by the parabolized Eulerian flow reactor model for different initial temperature fluctuations at Re = 10^4 and Re = 10^5; the initial mean temperature is $\{T\}_0 = 850$ K, H_2/air-mixture with $\{\phi\}_0 = 0.4$, and $\{p\}_0 = 20$ bar.

A parametric study is performed to investigate effects of the temperature fluctuations on the ignition delay for $775\,\mathrm{K} \leq \{T\}_0 \leq 1200\,\mathrm{K}$. Due to the extended computational domain and run-time limitations, lower temperature conditions have not been considered in the present study. In agreement with the results from the particle method is the observation that with increasing initial temperature fluctuations the ignition delay continuously decreases. This trend is most prominent for initial mean-flow temperatures above 900 K. For lower temperatures, the ignition-curves show a plateau, and the time-scale analysis that is presented in the following section indicates that this can be attributed to the presence of deflagrative ignition regimes.

The effect of initial mixture inhomogeneities on the ignition behavior is investigated by treating the initial temperature and mixture fraction fluctuations as uncorrelated quantities. A parametric study is performed for $\{T\}_0 = 850$ K and $0\,\mathrm{K} \leq \{T'\}_0 \leq 100\,\mathrm{K}$, and the range of mixture fraction fluctuations that are imposed at the inlet of the flow reactor is $Z_0'/\{Z\}_0 \leq 0.3$. Such values are comparable with experimental data (see Fig. 4.1 and Ref. [96]). Simulation results obtained from this parametric investigation are presented in Fig. 4.12. The results show that the ignition delay exhibits only a moderate sensitivity to mixture-fraction fluctuations, and inhomogeneities in temperature have a more pronounced effect on the ignition. Only for conditions of $T_0' \leq 50$ K is an effect of mixture perturbations on τ_{ig} observable. Interestingly, the results for $T_0' = 0$ K indicate that the ignition is delayed for $0.025 \leq Z_0'/\{Z\}_0 \leq 0.15$ is delayed. An analysis showed that this behavior is a result of the nonlinear competition between ignition and deflagration (see Fig. 4.11).

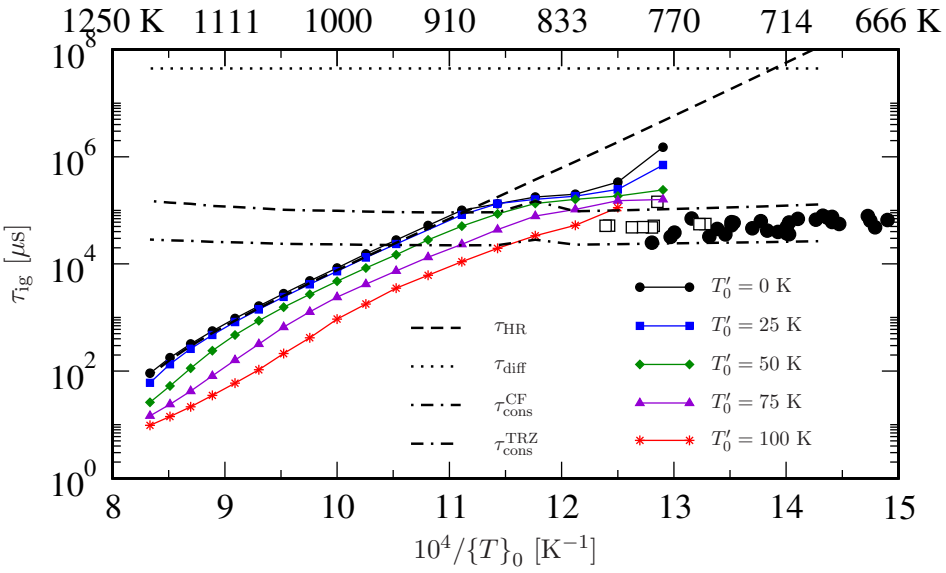

Figure 4.11: Parametric study of ignition delay times for different levels of initial temperature perturbations, and illustration of characteristic time scales. Measured ignition delays from flow reactors [94,104] are adjusted to a pressure of 20 bar. Please refer to Fig. 4.8 for legend.

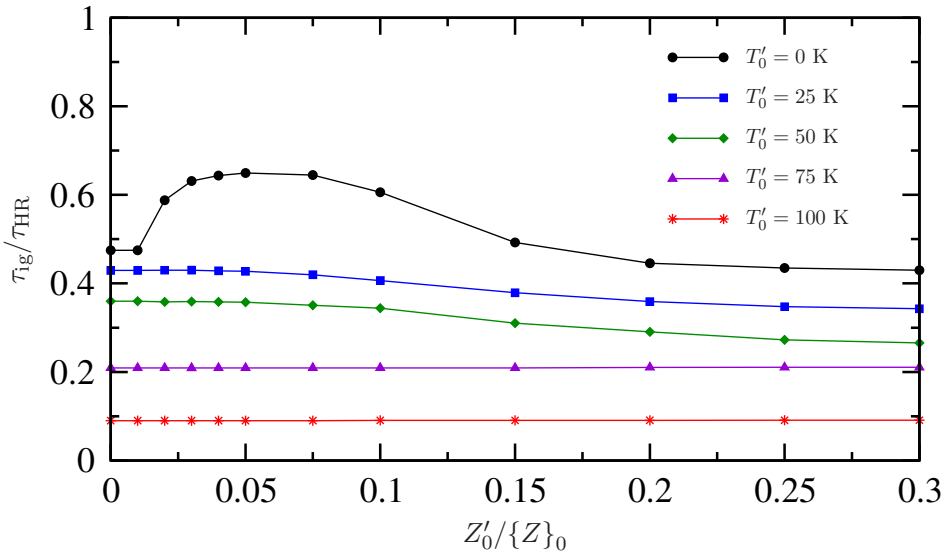

Figure 4.12: Parametric study of ignition delay times for different levels of initial temperature and mixture fraction perturbations at Re = 10^5; the initial mean temperature is $\{T\}_0 = 850$ K, H_2/air-mixture with $\{\phi\}_0 = 0.4$, and $\{p\}_0 = 20$ bar. Ignition delay is normalized by homogeneous reactor results.

4.3 Discussion

To further examine effects of the competing combustion-physical processes on the ignition behavior in flow reactors, a time-scale analysis is performed. Five relevant time-scales can be identified that require consideration in flow reactors. The first time scale is the convective time-scale, which is defined as

$$\tau_{\text{conv}} = \frac{x}{U_{\text{b}}} \, . \tag{4.15}$$

For ideal flow reactors τ_{conv} is in balance with the characteristic chemical time-scale, τ_{HR}, which is determined from a homogeneous reactor simulation using the ignition criterion discussed in Sec. 2:

$$\tau_{\text{HR}} = \text{argmin}_t(T_{\text{HR}}(t) \geq \alpha\{T\}_0) \, , \tag{4.16}$$

where $\alpha = 1.1$. The third relevant time-scale is the turbulent diffusion time-scale,

$$\tau_{\text{diff}} = \frac{\delta^2 \text{Sc}}{\nu_T} \, , \tag{4.17}$$

which is here defined with respect to the characteristic boundary-layer thickness δ since the turbulent mixing is controlled by velocity-gradients in the near-wall region. In addition to the chemical time-scale that is evaluated from the homogeneous reactor simulation, a chemical time-scale associated with the reactant consumption can be identified. This time scale can be evaluated from the turbulent flame-speed s_T:

$$\tau_{\text{cons}} = \frac{R}{s_T} \, , \tag{4.18}$$

where R is the radius of the flow-reactor, which is here taken as the characteristic length-scale. To define s_T, we consider the regimes of corrugated flamelets (CF) and thin reaction zones (TRZ). Peters [105] developed models for turbulent flame-speed for both regimes. To the limit of the corrugated flamelets regime,

$$\frac{s_T^{\text{CF}}}{s_L^0} \approx 1 + \left(\frac{u'}{s_L^0} \right)^{1/2} \, , \tag{4.19}$$

where s_L^0 is the laminar flame speed and u' is the root-mean-square of the turbulent velocity. To the limit of the thin reaction zones regime [106],

$$\frac{s_T^{\text{TRZ}}}{s_L^0} \approx \left(\frac{\alpha_T}{\alpha} \right)^{1/2} \, , \tag{4.20}$$

where α is the molecular diffusivity. The laminar flame speed can be estimated by the following expression [85]:

$$s_L^0 \approx \left[2 \frac{\nu}{\text{Sc}} \omega_C(\overline{T}) \right]^{1/2} \quad \text{with} \quad \overline{T} = \frac{1}{4} \left(3T_{\text{ad}} + \{T_0\} \right) \, , \tag{4.21}$$

where T_{ad} is the adiabatic flame temperature.

Among these different time-scales, τ_{HR} exhibits the strongest sensitivity to the initial temperature, while the consumption time-scales τ_{cons} that are evaluated from s_T^{TRZ} and s_T^{CF} have considerably weaker temperature-dependencies. The turbulent diffusion time-scale τ_{diff} is only a function of Reynolds number. To assess the competition between these different scales, we estimates all time-scales from the simulation-results. Results from this analysis are presented in Fig. 4.11. From the ratio between these different time-scales the following three regimes can be identified, namely (i) the *fast-chemistry regime* for which $\tau_{\mathrm{HR}} \ll \tau_{\mathrm{cons}} \ll \tau_{\mathrm{diff}}$, (ii) the *slow-chemistry regime* with $\tau_{\mathrm{cons}} \ll \tau_{\mathrm{diff}} \ll \tau_{\mathrm{HR}}$, and (iii) the *intermediate ignition regime*, where $\tau_{\mathrm{cons}} \ll \tau_{\mathrm{HR}} \ll \tau_{\mathrm{diff}}$.

In the fast-chemistry regime, the thermal run-away and ignition process are so rapid that turbulent diffusion cannot effectively stir the reactive mixture so that the mixture ignites homogeneously. On the other hand, if the flow-reactor is in the slow-chemistry regime, the mixture is locally well stirred by turbulence transport so that ignition and deflagration kernels are suppressed, and the reaction progress resembles a plug flow reactor. In the intermediate ignition regime, τ_{HR} is shorter than τ_{diff}, which facilitates the formation of localized ignition kernels. The propagation of the resulting ignition front will accelerate the ignition elsewhere since $\tau_{\mathrm{cons}} \leq \tau_{\mathrm{HR}}$. The Arrhenius plot of Fig. 4.11 summarizes the predicted ignition delays and their relationship with respect to the three characteristic ignition regimes. This plot shows that two distinct mechanisms are capable of accelerating the ignition process: the initial temperature perturbation and the deflagration mode. It can be seen that the simulations predict the transition between homogeneous ignition and propagation regime, as evident by the reduces ignition-slope for $750\,\mathrm{K} \leq \{T\}_0 \leq 850\,\mathrm{K}$. In this regime, the predicted ignition delay deviates from the homogeneous reactor results. This deflagrative ignition mode also explains the discrepancy of the Eulerian combustion model and the particle method observed in Fig. 4.8. Specifically, at low T_0', the ignition-process falls in the intermediate regime, and with increasing temperature perturbation, the ignition process transitions to the fast-chemistry regime.

Comparisons with experimental data [94, 104] show that the model-predictions are in qualitative agreement for the temperature range between 750 K and 825 K. Most notable is that all the experimental data fall in the range bounded by $\tau_{\mathrm{cons}}^{\mathrm{CF}}$ and $\tau_{\mathrm{cons}}^{\mathrm{TRZ}}$. Although this observation does not provide sufficient evidence for the presence of a deflagrative ignition modes, these results motivate the need for further experimental and computational confirmation. In particular, spatial measurements of the ignition process in conjunction with the characterization of the inflow-condition could assist in delineating the transient ignition dynamics and potential correlations with mixture and temperature inhomogeneities. Modeling assumptions associated with the description of the flow-field, and the omission of dilatational effects and turbulence/chemistry coupling have been introduced to enable a parametric analysis of the ignition process in flow-reactors. By improving the model-fidelity, for instance by providing an improved description of the interaction between turbulence and heat-release, specific flow-reactor geometries, and experimentally informed input conditions, quantitative

predictions of ignition processes in flow-reactors can be obtained.

5 Conclusions

The influence of hydrodynamic effects and fluctuations in temperature and mixture composition on the autoignition of a lean H_2/air mixture in flow-reactors was investigated. Two different modeling approaches were developed to represent the turbulent mixing and ignition in these low-temperature flow-reactor environments, which are of interest to gas-turbine applications. The reaction chemistry was described using the high-pressure H_2/O_2-mechanism of Burke *et al.* [99]. Different velocity profiles were considered, including laminar, plug-flow, and two fully-developed turbulent profiles that cover the range of conditions found in flow reactors. The investigated parameter space is extended by also considering fluctuations in temperature and mixture composition. From the results, obtained from these parametric investigations, the following conclusions can be drawn:

- In the case of an initially homogeneous mixture, the particle ignition process is fairly insensitive to the underlying flow-field. Under these conditions the ignition location can directly be related to the particle residence time, and is therefore only dependent on the particle velocity.

- A Hagen-Poiseuille mean-flow profile leads to a spatially extended reaction zone, which is due to the parabolic velocity profile. Compared to the plug-flow velocity profile, a turbulent velocity field slightly delays the location at which ignition is observed; with increasing Reynolds-number the ignition location converges to the plug-flow reactor results. Following the ignition process, the turbulent mixing leads to a broadening of the reaction front.

- Simulation results confirm that the spatial extent of the induction period depends on the underlying reactor flow-field, and should not be considered in flow reactor studies. This result is consistent with findings from previous investigations [102].

- It was found that for the operating conditions considered the ignition delay exhibits a stronger dependence on initial temperature fluctuation than mixture inhomogeneities.

- A time-scale analysis identified the significance of three different processes, which are associated with the turbulent mixing, the homogeneous ignition, and flame-propagation. Qualitative comparisons with measurement support the presence of deflagrative ignition modes at low-temperature conditions, motivating the need for further experimental investigations to confirm this observation.

- Simulation results suggest that temperature perturbations play a critical role in flow reactors. To further substantiate these findings it is therefore necessary to experimen-

tally quantify the magnitude and distribution of the temperature fluctuations in flow reactors. To our knowledge, such measurements have so far not been conducted.

Chapter 5

Experimental Effort: Characterization and Analysis of Combustion Instabilities and its Assessment using Kilohertz Laser Diagnostics in a Gas Turbine Model Combustor

1 Introduction

1.1 Combustion instability in gas turbine engines

Combustion instability is characterized by the large oscillations of heat release and flame location, coupled with an exponentially growing pressure oscillation amplitude or a limit cycle of pressure oscillations sustained at a large amplitude. The relationship between combustion instability and acoustic instability was investigated by Lord Rayleigh [107], who stated that acoustic oscillations are amplified by heat release when the latter is in phase with pressure oscillations. This is called the Rayleigh criterion. Instabilities represent a major obstacle to implementation of low-NO_x lean-premixed technology in gas turbine engines, and they may lead to the catastrophic failure of the engine components. Zinn and Lieuwen [108] and Mongia et al. [109] explained that anchoring a premixed flame within an engine can be difficult. If the flame base is not adequately anchored, it can move in phase with the pressure oscillations and thus cause amplification. Heat release oscillations can be caused by equivalence ration oscillations [110] as well as flame surface area oscillations [111].

This work focuses on geometries that lead to a Helmholtz-type instability. It is noted that within a full-scale engine, instability is usually caused by either a standing wave or by a Helmholtz resonance. The latter occurs when a relatively short volume of fluid is connected to a small orifice. For example, Krebs et al. [112] state that in Siemens engines

Helmholtz resonances are called "breathing modes" and may occur in the 100 – 400 Hz range. Full-scale injector studies at Pratt and Whitney by Cohen and Banaszuk [113] and by Cohen et al. [114] found that their instability was due to a Helmholtz resonance at 200 Hz. Previous laboratory-scale experiments also have shown that a Helmholtz resonance occurs when a combustion instability is detected; these findings were reported by Temme et al. [115], Zähringer et al. [116], Uhm and Acharya [117], and Durox et al. [118]. General reviews of the many possible types of instabilities are given by McManus et al. [119], Ducruix et al. [120], Zinn and Lieuwen [108], and Mongia et al. [109].

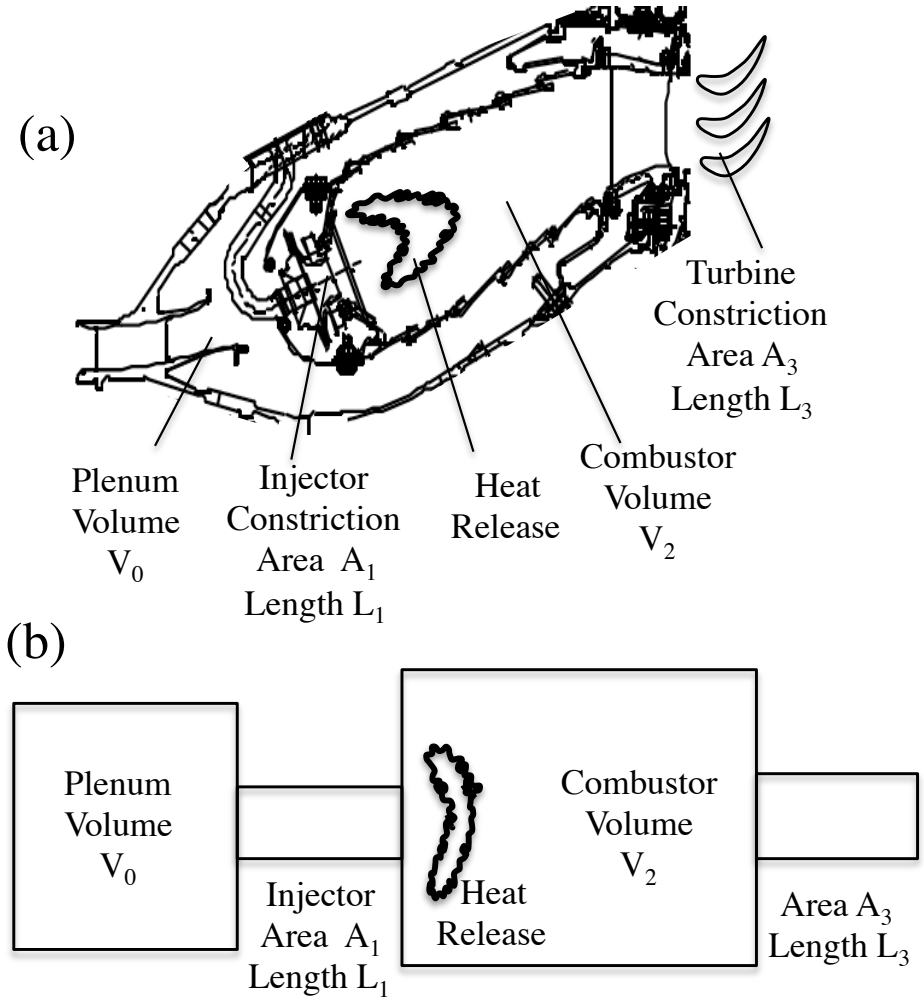

Figure 5.1: Schematic of the combustor of a gas turbine engine

The combustion chamber of a gas turbine engine can be considered to be a seres of connected chambers, as shown in figure 5.1a. Just Downstream of the combustor is an exit orifice that is the first stage of the turbine, where the flow is usually choked. Figure 5.1b

illustrates two chambers and two orifices. Based on this simplifying idea, the DLR (German Aerospace Center) gas turbine model combustor (GTMC) was designed by Meier and colleagues at DLR Stuttgart [121]. As shown in figure 5.3, the GTMC features a ring of fuel injectors surrounded dual swirling air injectors, in a plenum-injector-combustor-chimney configuration. It contains the basic feature of a practical combustor within a geometrically simple and optically accessible setup. The experimental measurements and reduced order modeling of combustion instabilities in this work will be based on the GTMC.

1.2 Previous research on the GTMC

Published literature of investigations on GTMC date back as far as 2003 [122, 123]. Meier and colleagues [121, 124–131] made extensive imaging measurements in their GTMC. One of their main interests was the flame-flow interaction. In particular, they studies how the vortex-like motion of the helical Precessing Vortex Core (PVC) interacts with the flame. They found that the PVC-flame interaction occurs in both cases: when an instability is present [124–127] as well as when it is absent [121, 128–131]. They imaged the flame using kilohertz OH PLIF and they imaged the PVC with kilohertz PIV. They found that the PVC rotation causes flow and flame oscillations at frequencies of 400∼500 Hz, while the pressure oscillations associated with the combustion instability occur at a lower frequency around 300 Hz. The fact that the PVC rotation and the combustion instability occur at different frequencies causes complications in the understanding of the physical mechanism of the heat release. They showed that the PVC-flame interaction affects where the heat is released, and it affects the time delay between pressure oscillations and the heat release rate oscillations.

Steinberg et al. [124, 126] found that the pressure fluctuations in the plenum of GTMC are 60°∼80° out oh phase with those in the combustor and they inferred that the acoustic resonance is of the Helmholtz type. Their measured phase difference is reasonable for a Helmholtz resonator and is likely due to acoustic damping at the injector. Their results indicate that the pressure field and the acoustic resonance may be relatively simple, as the Helmholtz resonator has uniform pressure fluctuations. However the heat release that drives the instability may be complex and due to PVC-flame interactions.

Allison et al. [132] operated a GTMC burner at Michigan that is identical to the DLR design. They investigated the effect of varying geometry parameters, flow rates, and equivalence ratio for various fuels. Figures 5.2a and 5.2b shows that the measured frequency decreases with an increase in plenum volume and with an increase in exhaust tube length. Figure 5.2 indicates that frequency increases with increasing mass flow rates for different fuels. The fact that instability frequency depends on both the geometries of plenum and chimney indicates that the observed combustion instability is caused by a multi-chamber resonance.

In later works, Allison et al. investigated those parameters on a DME flame [133, 134]. The results show that DME flames behave similar to other fuels in terms of dependency of frequency on equivalence ratio and mass flow rates. The instability frequency of all fuels is shown to be mostly proportional to the air mass flow rate, as shown in figure 5.2c. Another

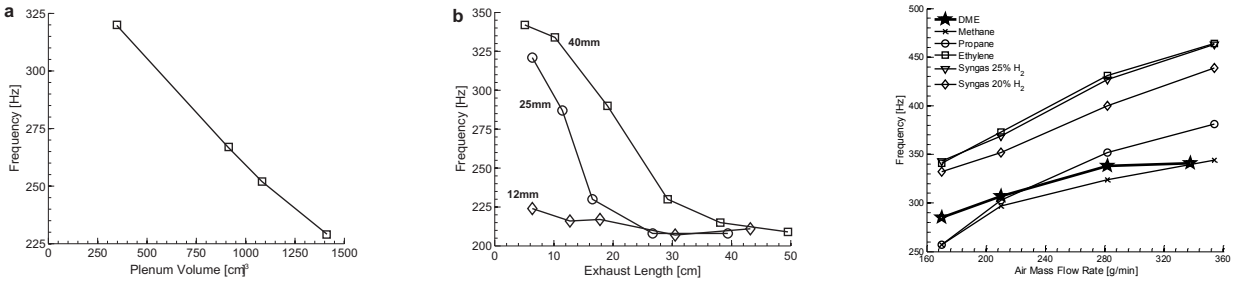

(a) (b) (c)

Figure 5.2: Frequency response to burner configuration variations in Allison et al.'s work [132, 133].(a) Effect of varying plenum volume; (b) effect of varying exhaust tube length with varies tube diameters: 40 mm, 25 mm, and 12 mm; (c) effect of varying air flow rates for various fuels

important aspect of this later work is the investigation of a quiet flame at $\phi = 0.75$ and a resonating flame at $\phi = 1.2$. This is detailed in table 5.1. At $\phi = 0.75$ the pressure oscillation amplitude is very small that an accurate determination of instability was not quite possible.

Table 5.1: Flame surface response at different equivalence ratios [133]

Fuel Type	DME	DME	DME
Air flow rate [g/min]	282	282	282
ϕ	0.75	1	1.2
Instability present	No	Yes	Yes
Acoustic Frequency [Hz]	N/A	310	320
FSD Frequency [Hz]	10	310	320

1.3 Previous models of combustion instability

Combustion instability encountered in the GTMC is caused by the interactions between turbulent combustion, fluid dynamics, and non-linear acoustics. Each of these processes are challenging to model, hence modeling combustion instability in the GTMC with high fidelity model is particularly difficult. See and Ihme [135] used the Flamelet Progress Variable (FPV) model in the context of Large Eddy Simulation to model the GTMC at stable operating conditions, but the unstable conditions have yet been tackled.

In view of the obstacles in the high fidelity models, another approach to model combustion instability has been developed. This approach is to use reduced order models to represent the basic physics and ignore the high order effects involved. Such approach have been taken by several research groups on various experimental geometries. Notably, Hathout et al. [136] studied the case where a combustion chamber with an inlet and an outlet acts as a Helmholtz resonator. Heat release rate of the combustion chamber was related to flame surface area,

which was determined by local flame speed and inlet velocity, with the latter being the deciding factor. Pressure and velocity were correlated in the inlet pipe through conservation of momentum. In this way a second-order ordinary differential equation was then derived for the pressure fluctuations. Through stability analysis of the equation, the stable operating envelop was determined.

Researchers from Laboratoire EM2C at École Centrale Paris studied another set of setups [137, 138]. Specifically, Schuller et al. [139] studied the acoustic coupling effects of a plenum-injector-combustor system using a reduced order model through matrix eigenvalue analysis. Palies et al. [140] studied the same setup with fluctuating heat release rate, using the Flame Describing Function (FDF) framework. Furthermore, this analysis was compared to a Helmholtz solver by Silva et al. [141], with good agreements.

1.4 Motivation and outline of this work

Despite the many previous works on the GTMC burner, there were several unanswered questions about the combustion instability that needs to be addressed. For example, an explanation is needed to explain the dependence of instability frequency on burner geometries and mass flow rates as shown in figure 5.2. The previous model by Hathout et al. is a useful concept but it is not adequate for the present geometry because it only considers one combined volume (the combustion chamber and injector), hence it can not explain the effect of chimney geometry. To develop a new model to provide the necessary explanation, further experimental measurements on the frequency spectrum of velocity, heat release, and pressure oscillations are needed. In addition to the frequencies, the relative phase shift between these quantities are also very important quantities to validate the model predictions.

Therefore, the scope of this chapter is to perform a set of diagnostic experiments to extract information relevant to thermo-acoustic instabilities in the GTMC at different operating conditions and to develop a reduced order model based on the experimental observations to provide an explanation to current and previously obtained data.

2 Experimental characterizations of combustion instability in the GTMC

2.1 Experimental setup

A schematic drawing of the gas turbine model combustor (GTMC) is shown in figure 5.3. The injector of the GTMC consists of a central air nozzle, an annular fuel nozzle, and a co-annular air nozzle. Both air nozzles supply swirling dry air at atmospheric pressure and temperature from a common plenum. The inner air nozzle has an outer diameter of 15 mm and the annular nozzle has an inner diameter of 17 mm and an outer diameter of 25 mm. The measured swirl number is approximately 0.55. Non-swirling fuel is provided through

three exterior ports fed through the annular nozzle which is subdivided into 72 channels of dimension 0.5 mm × 0.5 mm. The width of the fuel annulus is less than 0.5 mm. The exit plane of the central air nozzle and fuel nozzle lies 4.5 mm below the exit plane of the outer air annulus. The exit plane of the outer air annulus will be referred to as the burner surface. The combustion chamber has a square cross section of 85mm in width and 110 mm in height. The exit of the burner has a tapered lid which leads to an exhaust chimney with a diameter of 40 mm and a height of 50 mm. The burner is operated with fused silica windows, with a thickness of 1.5 mm, for flame visualization. The burner was fired with dimethyl ether (DME) fuel. An external cylindrical chamber was used for the equal division of the fuel flow into three separate lines which lead to the fuel ports on the burner. Mass flow rates for air and fuel lines were controlled by sonically choked orifices.

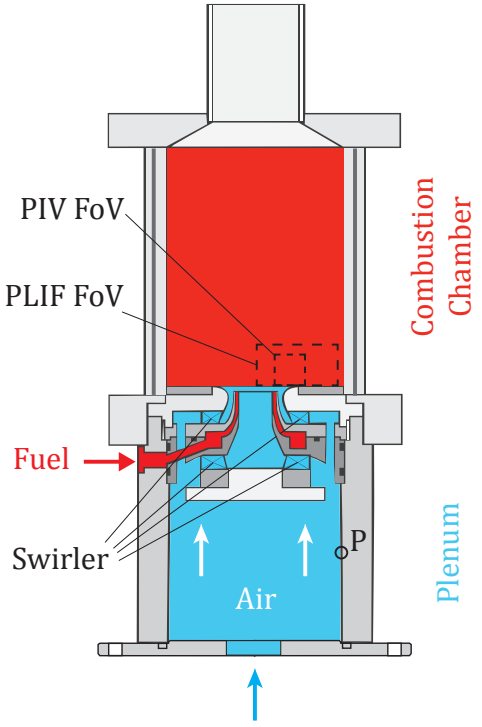

Figure 5.3: Schematic of the GMTC [121]

The diagnostic system consists of a PIV-PLIF-pressure measurement setup operated at a sustained frequency of 4 kHz. The PIV system operates a 532 nm beam generated from the high speed diode-pumped Nd:YAG laser while the PLIF system operates a 355 nm beam from a similar laser. Before reaching the burner, the 532 nm beam is merged with the 355 nm beam at a dichroic mirror (CVI BSR-35-2025) that transmits 532 nm light and reflects 355 nm light. When the laser beams reach the burner surfaces, the beam height is 20 mm.

Two sets of filters are placed in front of the cameras. For the PIV camera, the filter is

a narrow-band pass 532 nm filter (Andover 532FS02-50) that only lets the PIV signal (at 532 nm) passes through. For the PLIF camera, the filter set consist of a CG-385 filter that blocks light below 380 nm and another BG-3 filter that blocks light in the range of 480 nm to 680 nm. Because the majority of the CH_2O PLIF signal is in the range of 400 nm to 500 nm [142], such a combination of filters for PLIF camera can block the incident laser light at 355 nm and black body radiation at high wavelengths while retaining the PLIF signal.

The lens on both cameras are Nikkor 105mm f2.8 macro lens. The field of view (shown in figure 5.3 for both systems) of the PIV system is 15 mm × 15 mm while that of the PLIF system is 20 mm × 40 mm. The PIV image is represented by 384 × 384 pixels, yielding a scale of 39 μm per pixel. The PLIF image is represented by 508 × 1016 pixels (cropped from a 720 × 1280 raw image), yielding a scale of 39 μm per pixel as well. Both systems are tested with a standard 1951 USAF target for resolving power. The PIV camera returns a revolving power of 9 lpmm (line pairs per millimeter), which means that it can resolve a line no thinner than 56 μm. And the intensified PLIF camera (Phantom v711 + LaVision HS-IRO) has a resolving power of 7 lpmm (70 μm resolution). The resolving power of the PLIF camera (Phantom v711) itself is impaired after its coupling with the intensifier. This coupling between camera and intensifier has been manually adjusted to obtain the best resolving power possible.

As shown in figure 5.3, the PIV field of view is positioned at the exit of the swirler. In this way we can capture a fairly uniform flow field in our PIV frame. After processing the PIV images in LaVision Davis software with a 64 × 64 pixels window and 50% overlapping ratio, we obtained a matrix of 12 × 12 vectors per frame. After averaging through all 144 vectors in their axial and radial velocity component, we can estimate the average axial and radial velocity as well as the average velocity magnitude in our field of view.

Pressure measurement is conducted by a piezoelectric microphones (PCB 378C10) mounted on the plenum of the GTMC. From previous measurements [126,143] we know that the combustion chamber pressure fluctuation is at the same frequency as that of the plenum with a phase lag. Hence the combustion chamber pressure information can be obtained without obstructing the optical measurements. The pressure signal is related by a signal conditioner (PCB 482C05) to an oscilloscope (LeCroy Waverunner 6100A) at 1 MHz.

2.2 Heat release rate measurement with CH_2O PLIF

Previous measurements [144–146] have shown the relationship between flame surface density, chemiluminescence, and heat release rate. We assume that the integral of the flame surface area within each frame is proportional to the total heat release rate:

$$\dot{Q} \sim \sum_{A} l_{\mathrm{FS}} \tag{5.1}$$

where $\dot{Q}$ is the total heat release rate in a frame, l_{FS} is the flame surface length, and A is the area of the entire frame. Hence the fluctuations of heat release rate can be calculated from

the fluctuations of the total flame surface area in each frame. In this study we extract the flame surface information from the CH_2O PLIF images. In these images, the edge of CH_2O signal with larger gradients are identified as the flame.

The information of flame surface length inside a local region can also be used to calculate flame surface density (ρ_{FS}), which represents the average flame length inside a volume (or a region in 2D images) by:

$$\rho_{fs} = \lim_{\Delta x \to 0} \frac{\sum_{\Delta A} l_{fs}}{(\Delta x)^2} \tag{5.2}$$

where Δx is the length of the region (bin size) and ΔA is the area of the region (bin area). The importance of flame density is that it not only indicates where the flame wrinkling is most intense, it is also believed to be directly related to local volumetric heat release rate $\dot{q}$:

$$\rho_{fs} \sim \dot{q} \ . \tag{5.3}$$

Hence the flame surface density indicates the spatial distribution of heat release intensity.

2.3 Test case matrix

As shown in table 5.2, we consider four test cases in the present study. At the air flow rate of 282 g/min (which corresponds to case "B" in DLR experiments [121]), we have three cases: R1 (R:rich), S1 (S:stoichiometric), and L1 (L:lean) with equivalence ratio of 1.2, 1.0, and 0.75 respectively. In a reduced flow rate of 226 g/min (80% of standard case), we repeat the experiment for the rich case (R2).

Table 5.2: Test case matrix

Case	$\phi = 1.2$	$\phi = 1.0$	$\phi = 0.75$
$\dot{m}_{\mathrm{o}}$=282g/min	R1	S1	L1
$\dot{m}_{\mathrm{o}}$=226g/min	R2	–	–

The test case matrix is designed in such a way to explore: *i*) the differences in spatial and temporal structure of a unstable (R1) and a stable (L1) flame; *ii*) investigate the intermittent instability case at stoichiometric condition (S1); *iii*) explore the effect of reducing mass flow rates (between R1 and R2).

2.4 Experimental results

Thermo-acoustic instability is characterized by a large pressure fluctuation in the combustion system. So we start our presentation with the pressure spectrum to characterize the four cases in this study. First row of figure 5.4 shows the power spectrum of all four cases, normalized by a reference power in arbitrary unit. We can see from the first row that the pressure

spectrum between a unstable case (R1) and a stable case (L1) is very distinct. Whereas R1 has a single peak in 310∼320 Hz range, L1 has no prominent peak that is visible in the current scale. The spectrum of S1 (stoichiometric) is similar to that of R1, with a peak at the thermo-acoustic instability frequency of 310 Hz at a smaller magnitude. The single peak in R2 is smaller than R1, its frequency also shift into around 290 Hz range. This means that as mass flow rates decreases, the instability becomes weaker and shifts to a lower frequency.

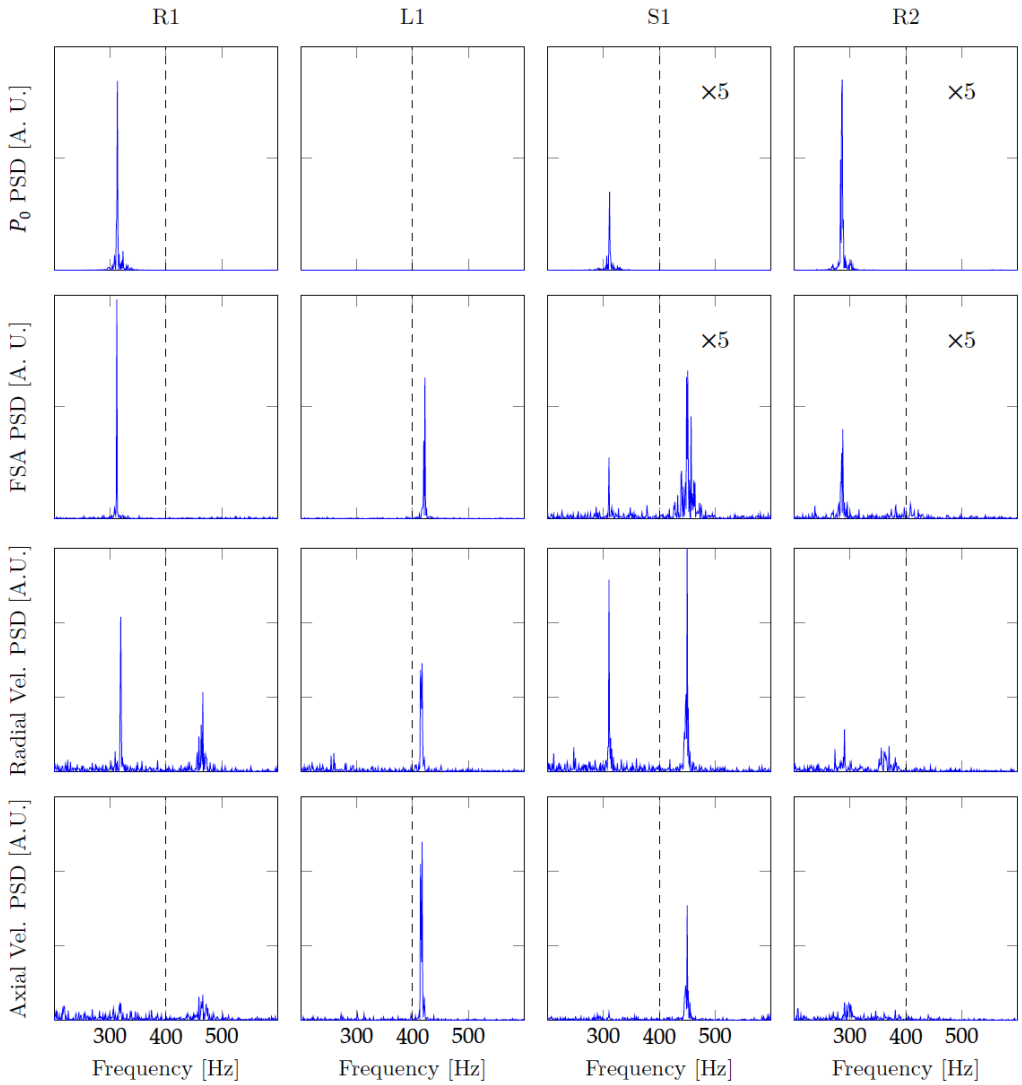

Figure 5.4: Normalized velocity power spectrum for all cases in arbitrary unit. First row: radial velocity PSD, second row: axial velocity PSD.

During an earlier and separate experiment [143], the pressure spectrum of both combustion chamber and plenum were also measured when there is no flame, as shown in figure 5.5.

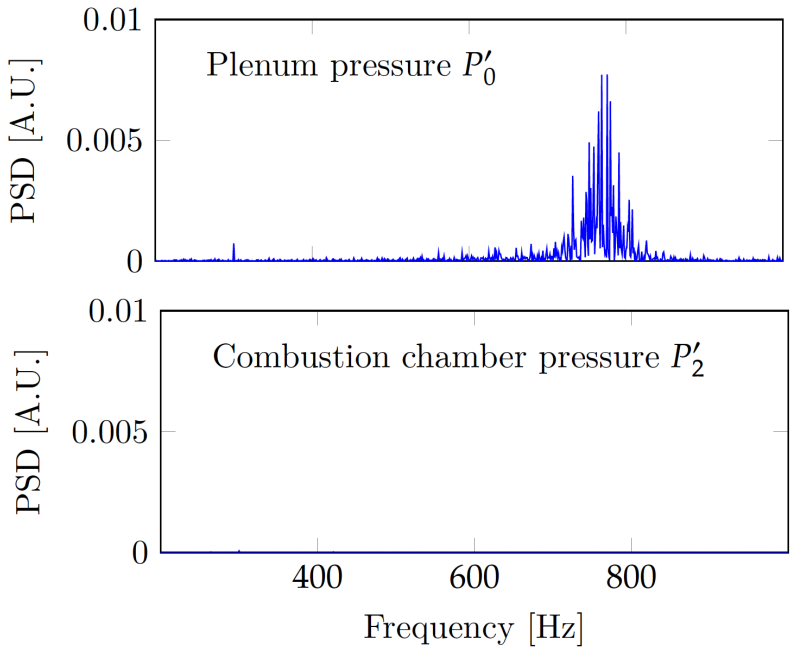

Figure 5.5: Power spectrum density of plenum and combustion chamber pressure with no flame.

It should be noted that the amplitude of pressure fluctuation when there is no flame is much smaller than those cases with flames. Furthermore, there is a dispersed peak in the plenum pressure PSD in the range of 700∼800 Hz whereas the combustion chamber pressure shows no visible peak. The observed peak may correspond to one of the system natural mode, and the mode corresponding to combustion instability is not excited in this case. In second row of figure 5.4 we present the power spectrum of the fluctuations of the total flame surface area as identified by our edge detection algorithm. We can see that the power spectrum of flame surface area gives us a series of new information. In the case of R1, flame surface area fluctuates at a single frequency, same as the pressure. We did not see any peaks in the pressure spectrum of L1, but the flame surface area has a very strong peak at 420 Hz. This is caused by the helical PVC that is rotating around the swirler. This flow feature has been well characterized by literature [125, 126]. The proof of the existence of PVC can be found in the velocity analysis later. While PVC rotates in the combustion chamber, it takes reactants and products with it. Hence there will be a overall fluctuation of CH_2O signal strength in the frame. Whether this is a artifact of image processing routine or it indicates actual heat release fluctuation has to be verified with velocity and pressure data. We see that the pressure spectrum of L1 is almost flat in this range, hence it is very unlikely that we are having a strong heat release oscillation at 420 Hz at the same time. Hence the fluctuation of flame surface area is unlikely to be linked to fluctuation of heat release rate. The effect of PVC is also evident in S1, albeit with a smaller magnitude. R2 on the other hand only shows a single peak at the themo-acoustic instability frequency of 290 Hz. This is similar to

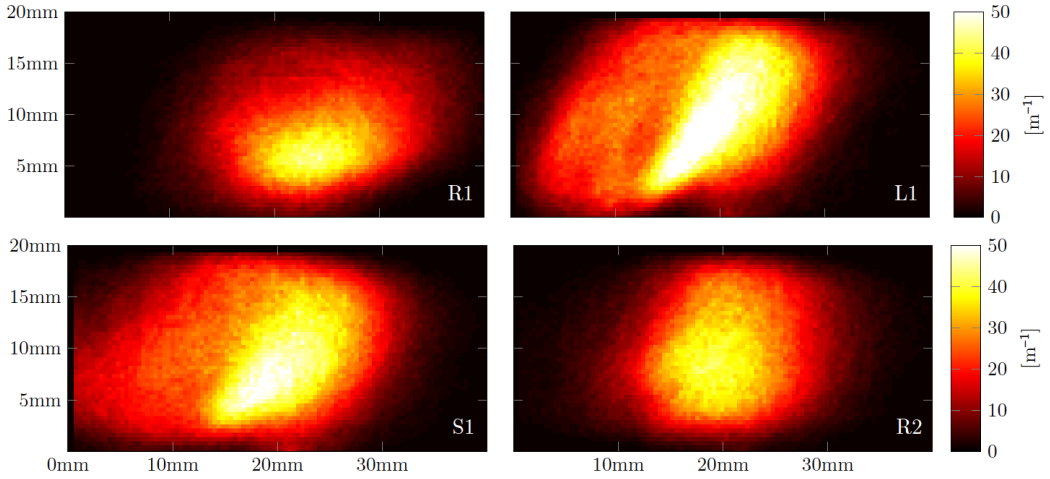

Figure 5.6: Flame surface density (FSD) for all four cases, in $[m^{-1}]$.

R1, only at a smaller magnitude.

Figure 5.6 shows the flame surface density of all four cases in the present work.We can see that the spatial distributions of R1 and L1 are quite different. The flame in R1 is distributed and flat, near the burner surface. The flame in L1 is more lifted, showing a "V" shape. This observation agrees with previous chemiluminescence measurements made by Allison et al. [132]. This is because L1 flame is stable, hence its flame surfaces are concentrated at a fixed location. Whereas R1 flame locations undergoes large oscillations, hence its flame surface density tends to be more dispersed. The shape of S1 is a combination of those of R1 and L1, again indicating that S1 is in the transition process. Lastly R2 is also concentrated like R1, but the average flame surface density is lower and its more lifted, both indicating that the flame in R2 is not as intense as that in R1.

A FFT analysis is carried out to explore the frequency spectrum of both velocity components, as shown in third and fourth rows of figure 5.4. The third row shows the power spectrum of radial velocity for all cases. There are two peaks in R1 radial velocity spectrum, which correspond to the thermo-acoustic instability frequency (∼320 Hz) and PVC frequency (∼460 Hz). This shows that the pressure fluctuation in the unstable case affects the velocity fluctuations. In L1 we only have one peak for the PVC above 400 Hz because of the absence of combustion instability. This PVC frequency is also the frequency of the peak in flame surface area spectrum of L1. This supports our claim that the observed peak for L1 is an artifact of image processing. The radial velocity fluctuations in S1 are stronger than R1 and L1 in at both instability frequency and PVC frequency. This not only indicates that S1 is a spectral/temporal superposition of R1 and L1, it also shows that the velocity fluctuations are large during the frequent flame re-position when it switches between the stable mode and unstable mode. Lastly, the spectrum of R2 radial velocity resembles that of R1 with a much smaller magnitude.

The fourth row of figure 5.4 shows the power spectrum of axial velocity for all cases. Compared to its radial velocity spectrum, the axial velocity spectrum of R1 shows little distinct features. This shows that the interaction between instability and velocity happens mostly in the radial directions. The axial velocity spectrum for L1 is very similar to its radial velocity spectrum, only with a larger magnitude. This again shows that PVC is a very prominent flow feature in L1 in spite of the lack of pressure fluctuations. The spectrum of S1 in the axial direction only shows one peak for the PVC. This reaffirms our previous observation that the instability dynamics affects mainly the velocity in the radial directions. The axial velocity spectrum of R2 shows a small peak at 290 Hz, but the PVC is absent. The difference between R2 and all other cases is that the PVC is represented by a dispersed and low magnitude modes in the frequency spectrum, meaning that the PVC is very weak in R2.

2.5 Discussion of experimental results

The experimental investigations above encompasses pressure, velocity, and heat release (with flame surface as a proxy) measurements for four different operating conditions. A wide range of differences between each case have been observed, from which we have the following findings.

Table 5.3: Summary of frequency spectrum of thermo-fluid variables for all four case in Hz, rounded to the nearest 10 Hz.

Case	R1	L1	S1	R2
P_0	320	–	310	290
FSA ($\dot{q}$)	320	420	310	290
Radial Vel.	320/460	420	310/450	290
Axial Vel.	–	420	450	–
PVC	460	420	450	–

i) The PLIF data provided spatially-resolved contours of the flame surface density, which are indicators of the contours of heat release rate. Thus PLIF provides better-resolved information about the spatial variation of the heat release rate than chemiluminescence. Table 5.3 gives a summary of the frequency spectrum of thermo-fluid variables in all four cases, which is made available by the high-repetition rate system. The PLIF data showed that the spectrum of flame surface density oscillations has a sharp spike at the same frequency as the spike in the pressure spectrum. This proves that the heat release rate is coupled to the pressure fluctuations. The kilohertz PIV data showed that the velocity field also has a peak at the instability frequency in unstable flames. This allows us to measure the relative phases between these quantities if proper spectral filtering is applied.

ii) From previous studies by Allison et al. [133] we already know that pressure fluctuation magnitude and flame surface density distribution are different between an unstable (R1)

an stable (L1) flame. Velocity spectrum analysis in this study revealed that the effect of combustion instability would change the axial and radial velocity distribution as well. In an unstable flame the major dynamics happened in the radial direction, with velocity undergoing a large oscillation radially. In a stable flame the velocity oscillation was more evenly distributed between axial and radial directions. Considering that the flame in an unstable case sits in the outer recirculation zone, it's the radial velocity component of the swirler jet that is being "pushed" by the flame back and forth. We are not arguing whether the velocity re-distribution is the cause or the effect in this process, but we do find the links between velocity and heat release.

iii) We also gained some insights on the relationship between PVC and combustion instability. As summarized in table 5.3, PVC was present in both R1 and L1 flame. In the meantime, in flame R2, we did not see evidences of PVC, but we still saw a peak in pressure oscillation. Additionally, from L1, S1 to R1 the frequency of PVC was increasing almost linearly, which corresponds to the increase of mass flow rate. This means that the presence of combustion instability did not quite affect PVC. This means that while instability and PVC do work together in determining the velocity distribution, physically the two are quite independent phenomena in nature.

iv) The pressure spectrum of S1 (intermittent instability) and R2 (weak instability) were very similar, but they represented two very different kinds of flame. The former, as transitional state at the stability limit, always possessed the features of both R1 (unstable) and L1 (stable) flame. S1 can be thought of as a temporal average of R1 and L1. R2 represented a different physical process. At a lower flow rate, the instability frequency is lower. And from flame surface density we saw that the flame was more lifted off and less intense. The velocity magnitude fluctuation was also fairly small compared to R1, L1, or S1. This leads us to believe that a reduced flow rate made the flame "milder" even though equivalence ratio still determines the characteristics of the instability.

3 Reduced Order Modeling of Combustion Instability in the GTMC

To understand the phenomena observed in our experiment, we propose a reduced order model to describe the system instability in the GTMC. In this chapter we will first derive the governing equations of the model, and then apply this model to the GTMC and compare the predictions with experimental data.

From previous studies [124, 143] it has been concluded that the combustion instability presently observed is dominated by a Helmholtz mode. Hence our proposed reduced order model has to be based on a Helmholtz resonator analysis. Similar analysis have also been carried out previously on several different setups [136, 139]. The differences between the aforementioned models are that: *i*) our model is based on a multi-chamber analysis instead of the single chamber analysis done by Hathout et al. [136]; *ii*) our model does not need

experimental calibration, whereas the Flame Describing Function (FDF) proposed by Palies et al. [140] requires an experimentally determined flame transfer function; *iii*) the geometry considered in our model is a close resemblance of the GTMC, which in turn is similar to that of a real jet engine combustor chamber.

3.1 Single chamber Helmholtz analysis – extension of previous models

Before we proceed to establish the governing equations for the present model, we need to build it upon a single Helmholtz resonator analysis. This analysis is based on the model proposed by Hathout et al. [136] with new extensions. Figure 5.7 shows the schematics of single chamber Helmholtz resonator.

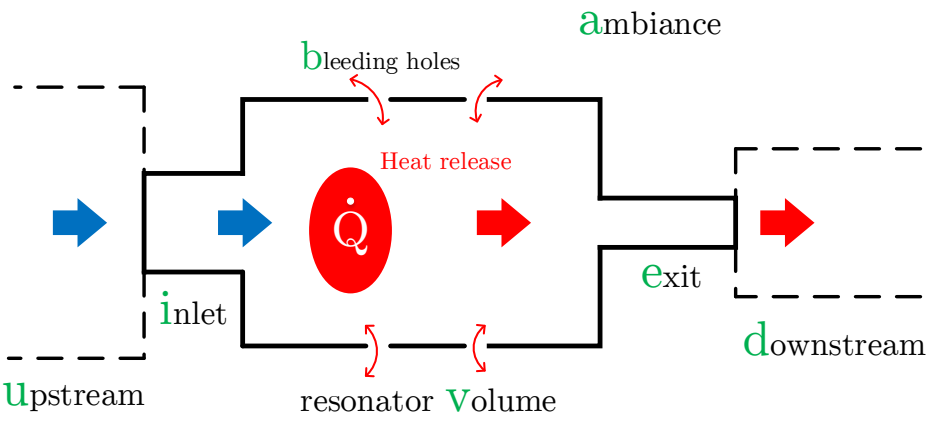

Figure 5.7: Schematic of a single chamber Helmholtz resonator

Suppose we have large volume "v" connected with an inlet and an outlet (labeled as "i" and "e" respectively). There is a mean flow flowing from inlet to outlet. Additionally, there are small bleeding holes on the walls of the volume (labeled as "w"), but the size of these holes are small so that the mass flow rate is much smaller than that of either inlet or exit. Inside the volume there is heat source with an unsteady heat release rate of $\dot{Q}_\mathrm{v}$. There is also heat loss from the wall into the surroundings, whose rate is $\dot{Q}_\mathrm{w}$. The pressure of the upstream of the inlet is P_u, the pressure of the downstream of the outlet is P_d, and the pressure outside the bleeding holes is P_a. All components are axisymmetric, and it is assumed that all thermodynamic and fluid variables are uniform in each component. The meanings of the variables used below can be referenced to the nomenclature.

Applying the first law of thermodynamics to volume v, we have:

$$V_\mathrm{v}\frac{d\rho_\mathrm{v}e_\mathrm{v}}{dt} = \dot{m}_\mathrm{i}h_\mathrm{i} - \dot{m}_\mathrm{e}h_\mathrm{e} - \dot{m}_\mathrm{w}h_\mathrm{v} + \dot{Q}_\mathrm{v} - \dot{Q}_\mathrm{w}\ . \tag{5.4}$$

If we neglect the temperature dependence of $c_{\rm V}$ and $c_{\rm P}$ for simplicity, then $e = c_{\rm V}(T - T_{\rm ref})$ and $h = c_{\rm P}(T - T_{\rm ref})$. Reference temperature $T_{\rm ref}$ is taken as 0 here. Along with the relationships $c_{\rm V} = R/(\gamma - 1)$, $c_{\rm P} = R\gamma/(\gamma - 1)$, and $P = \rho RT$, Eq.(5.4) can be written as:

$$\frac{V_{\rm v}}{\gamma_{\rm v} - 1}\frac{dP_{\rm v}}{dt} = \dot{m}_{\rm i}\frac{\gamma_{\rm i}}{\gamma_{\rm i} - 1}R_{\rm i}T_{\rm i} - \dot{m}_{\rm e}\frac{\gamma_{\rm e}}{\gamma_{\rm e} - 1}R_{\rm e}T_{\rm e} - \dot{m}_{\rm w}\frac{\gamma_{\rm v}}{\gamma_{\rm v} - 1}R_{\rm v}T_{\rm v} + \dot{Q}_{\rm v} - \dot{Q}_{\rm w} \quad . \tag{5.5}$$

Now substitute speed of sound $C = \sqrt{\gamma RT}$ into Eq.(5.5) and assume C to be constant, then take time derivative of Eq.(5.5), we will have:

$$\frac{d^2P_{\rm v}}{dt^2} = \frac{\gamma_{\rm v} - 1}{V_{\rm v}}\left(\frac{C_{\rm i}^2}{\gamma_{\rm i} - 1}\frac{d\dot{m}_{\rm i}}{dt} - \frac{C_{\rm e}^2}{\gamma_{\rm e} - 1}\frac{d\dot{m}_{\rm e}}{dt}\right) - \frac{C_{\rm v}^2}{V_{\rm v}}\frac{d\dot{m}_{\rm w}}{dt} + \frac{\gamma_{\rm v} - 1}{V_{\rm v}}\left(\frac{d\dot{Q}_{\rm v}}{dt} - \frac{d\dot{Q}_{\rm w}}{dt}\right) \quad . \tag{5.6}$$

Equation (5.6) relates the pressure fluctuation inside the volume to the fluctuation of the mass flow rates in and out from the volume as well as the heat release and loss rate fluctuation. The fluctuation of mass flow rates in the inlet and outlet can be related to the velocity fluctuation inside them. The axial momentum equation inside the inlet can be written as:

$$\rho_{\rm i}\frac{dU_{\rm i}}{dt} + \rho_{\rm i}U_{\rm i}\frac{dU_{\rm i}}{dx} = -\frac{dP_{\rm i}}{dx} + \nabla \cdot \sigma_{\rm v} \; . \tag{5.7}$$

As aforementioned, we assume the fluid mechanics variables to be uniform in each component. If we assume a constant pressure gradient across the inlet and neglect surface shear stress, then Eq.(5.7) can be written as:

$$\rho_{\rm i}\frac{dU_{\rm i}}{dt} = -\frac{dP_{\rm i}}{dx} = \frac{P_{\rm u} - P_{\rm v}}{l_{\rm i}} \; . \tag{5.8}$$

Therefore the time derivative of mass flow rate through inlet can be obtained:

$$\frac{d\dot{m}_{\rm i}}{dt} = A_{\rm i}\rho_{\rm i}\frac{dU_{\rm i}}{dt} = \frac{A_{\rm i}}{l_{\rm i}}(P_{\rm u} - P_{\rm v}) \; . \tag{5.9}$$

Similarly, the mass flow rate fluctuation inside outlet can be written as:

$$\frac{d\dot{m}_{\rm e}}{dt} = \frac{A_{\rm e}}{l_{\rm e}}(P_{\rm v} - P_{\rm d}) \; . \tag{5.10}$$

The mass flow rates of bleeding from volume v depends on the specific configurations of the chamber. Assume that the size of the bleeding hole is a small fraction ($\epsilon_{\rm A}$) of the total area of the walls of the volume $A_{\rm w}$ and the fluid inside the chamber is quiescent in radial direction, then the ideal discharge velocity through the bleeding holes is given by Bernoulli's equation as:

$$|U_{\rm w}| = \sqrt{\frac{2|P_{\rm v} - P_{\rm a}|}{\rho_{\rm v}}} \; . \tag{5.11}$$

Now taking the friction loss into consideration, the mass flow rate of the leakage is given by:

$$\begin{aligned}\dot{m}_{\mathrm{w}} =& \mathcal{C}_{\mathrm{d}}\epsilon_{\mathrm{A}}A_{\mathrm{w}}\rho_{\mathrm{v}}U_{\mathrm{w}} \\ =& \mathcal{C}_{\mathrm{d}}\epsilon_{\mathrm{A}}A_{\mathrm{w}}\sqrt{\frac{2\rho_{\mathrm{v}}}{|P_{\mathrm{v}}-P_{\mathrm{a}}|}}\left(P_{\mathrm{v}}-P_{\mathrm{a}}\right),\end{aligned}$$

where $\mathcal{C}_{\mathrm{d}}$ is the discharge coefficient that depends on the shape and size of the hole. If the ambient conditions are steady, then taking the time derivative of Eq.(5.12) would yield:

$$\frac{d\dot{m}_{\mathrm{w}}}{dt} = \mathcal{C}_{\mathrm{d}}\epsilon_{\mathrm{A}}A_{\mathrm{w}}\sqrt{\frac{\rho_{\mathrm{v}}}{2|P_{\mathrm{v}}-P_{\mathrm{a}}|}}\frac{dP_{\mathrm{v}}}{dt}\ . \tag{5.12}$$

The physical process of heat loss through the wall consists of three parts: heat convection from the fluid inside the volume to the wall, heat conduction across the wall, and heat convection (as well as possible radiation) from the wall to the ambience. The heat loss $\dot{Q}_{\mathrm{w}}$ can be analyzed through a thermal circuit analysis:

$$\dot{Q}_{\mathrm{w}} = \frac{T_{\mathrm{v}}-T_{\mathrm{a}}}{\Omega}\ , \tag{5.13}$$

where Ω is the total thermal resistance related to the heat conduction (κ), heat convection coefficients (η) and heat radiation. The specific form of Ω depends on the configuration of the resonator in study. Again, if we assume the ambient conditions are steady, then the time derivative of Eq.(5.13) takes the form:

$$\frac{d\dot{Q}_{\mathrm{w}}}{dt} = \frac{1}{\Omega}\frac{dT_{\mathrm{v}}}{dt} = \frac{1}{\Omega\rho_{\mathrm{v}}R_{\mathrm{v}}}\frac{dP_{\mathrm{v}}}{dt}\ . \tag{5.14}$$

Now if we substitute Eqs.(5.9), (5.10), (5.12), and (5.14) into Eq.(5.6), separate V_{v} into $V_{\mathrm{v}} = A_{\mathrm{v}}l_{\mathrm{v}}$ and rearrange terms in Eq.(5.6), we will have:

$$\frac{d^2P_{\mathrm{v}}}{dt^2} + (\mathcal{T}_{\mathrm{i}} + \mathcal{T}_{\mathrm{ii}})\frac{dP_{\mathrm{v}}}{dt} + (\mathcal{T}_{\mathrm{iii}} + \mathcal{T}_{\mathrm{iv}})P_{\mathrm{v}} = \mathcal{T}_{\mathrm{iii}}P_{\mathrm{u}} + \mathcal{T}_{\mathrm{iv}}P_{\mathrm{d}} + \frac{\gamma_{\mathrm{v}}-1}{V_{\mathrm{v}}}\frac{d\dot{Q}_{\mathrm{v}}}{dt}\quad , \tag{5.15}$$

where the terms $\mathcal{T}_{\mathrm{n}}$ are:

$$\begin{aligned}\mathcal{T}_{\mathrm{i}} &= \frac{C_{\mathrm{v}}^2}{V_{\mathrm{v}}}\mathcal{C}_{\mathrm{d}}\epsilon_{\mathrm{A}}A_{\mathrm{w}}\sqrt{\frac{2\rho_{\mathrm{v}}}{|P_{\mathrm{v}}-P_{\mathrm{a}}|}}\ , \\ \mathcal{T}_{\mathrm{ii}} &= \frac{\gamma_{\mathrm{v}}-1}{V_{\mathrm{v}}}\frac{1}{\Omega\rho_{\mathrm{v}}R_{\mathrm{v}}}\ , \\ \mathcal{T}_{\mathrm{iii}} &= \frac{\gamma_{\mathrm{v}}-1}{\gamma_{\mathrm{i}}-1}\left(\frac{C_{\mathrm{i}}^2A_{\mathrm{i}}}{V_{\mathrm{v}}l_{\mathrm{i}}}\right)\ , \\ \mathcal{T}_{\mathrm{iv}} &= \frac{\gamma_{\mathrm{v}}-1}{\gamma_{\mathrm{e}}-1}\left(\frac{C_{\mathrm{e}}^2A_{\mathrm{e}}}{V_{\mathrm{v}}l_{\mathrm{e}}}\right)\ .\end{aligned}$$

Equation 5.15 is the pressure governing equation for a single chamber Helmholtz resonator with different inlet/outlet temperature and gas composition. It also considers the phenomena of fluid bleeding and wall heat transfer. From it we can also assess the contributions of different heat/mass transfer to the system dynamics. Specifically, fluid leakage through bleeding holes (term $\mathcal{T}_{\mathrm{i}}$) and wall heat loss (term $\mathcal{T}_{\mathrm{ii}}$) provide damping to the system. The geometry of the inlet and outlet (term $\mathcal{T}_{\mathrm{iii}}$ and $\mathcal{T}_{\mathrm{iv}}$) affects the system resonance frequency. And the driving force of the system is provided by a combination of upstream pressure P_{u}, downstream pressure P_{d}, and internal heat release $\dot{Q}_{\mathrm{V}}$.

3.2 Dual chamber Helmholtz analysis – the newly proposed model

In the proposed model, the GMTC is simplified and takes the form of an abstract system consisting of four connected bodies, as shown in figure 5.8. Here the four major elements of the system correspond to (0) plenum, (1) injector/swirler, (2) combustion chamber, and (3) chimney. The key assumptions of this model are: *i*) the system elements are assumed to be zero dimensional in space. All gas properties (pressure, temperature, etc.) are uniform within each element; *ii*) the system is operated at low Mach numbers, no compressibility effects are considered. With these assumptions, each element is characterized by its length and cross-section area. Cold mixture flows from plenum through injector into the combustion chamber. It is then immediately ignited and exits from the chimney. The complex flow field across the injector is neglected.

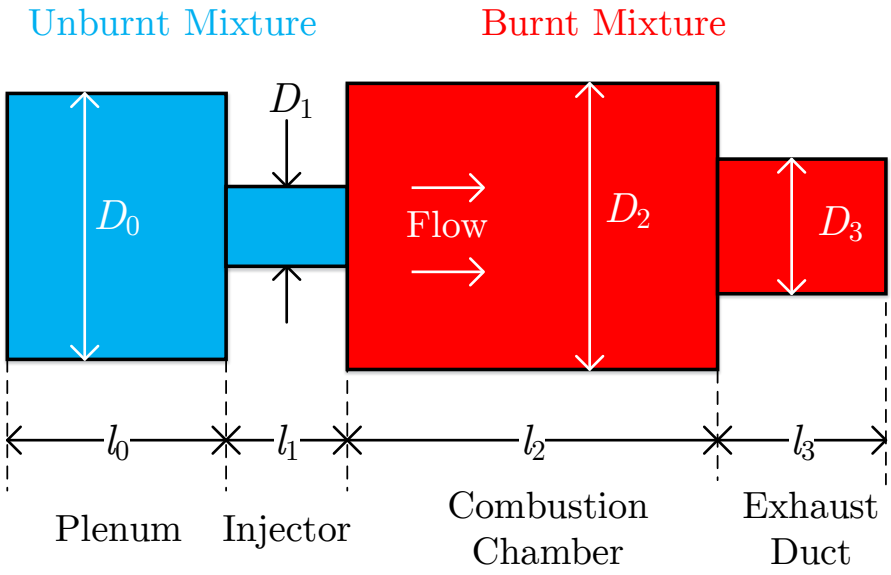

Figure 5.8: Schematic of the geometry considered in proposed reduced-order model (ROM)

The plenum and combustion chamber are identified as the Helmholtz volumes. In the next sections, we apply the analysis laid out in section 3.1 to both plenum and the combustion

chamber of the GTMC to obtain the governing equations of the proposed model.

3.2.1 Plenum pressure equation

Only cold air flows through plenum, so using the terminology laid out in section 3.1, we have $\gamma_{\mathrm{i}} = \gamma_{\mathrm{v}} = \gamma_{\mathrm{e}} = \gamma_{\mathrm{c}}$ and $\dot{Q}_{\mathrm{w}} = 0$ ($\mathcal{T}_{\mathrm{i}} = 0$). Because plenum is constructed with solid steel walls, the bleeding stream is nonexistent. Therefore term $\mathcal{T}_{\mathrm{ii}} = 0$. Additionally, because the upstream of the inlet pipe to the plenum is very long and narrow, we have for plenum that $l_{\mathrm{i}} \to \infty$, hence term $\mathcal{T}_{\mathrm{iii}} = 0$. Furthermore, there is no heat release inside the plenum, so $\dot{Q}_{\mathrm{v}} = 0$. With these conditions, we can write Eq.(5.15) with the notation in the GTMC framework ({v,e,d}→{0,1,2}):

$$\frac{d^2 P_0'}{dt^2} + \left(\frac{C_{\mathrm{c}}^2 A_1}{V_0 l_1}\right) \cdot P_0' = \left(\frac{C_{\mathrm{c}}^2 A_1}{V_0 l_1}\right) \cdot P_2' \,. \tag{5.16}$$

Note that here we only consider the thermo-acoustic fluctuation of the pressure, hence $dP = dP'$. If we define the Helmholtz resonance frequency ω_0 of plenum to be

$$\omega_0 = \sqrt{\frac{C_{\mathrm{c}}^2 A_1}{V_0 l_1}} \,, \tag{5.17}$$

then Eq.(5.16) can be written as:

$$\frac{d^2 P_0'}{dt^2} + {\omega_0}^2 \cdot P_0' = {\omega_0}^2 \cdot P_2' \,. \tag{5.18}$$

3.2.2 Combustion chamber pressure equation

Combustion chamber inlet temperature (∼300K) is very different from that inside the chamber (∼2000K), hence $\gamma_{\mathrm{i}} = \gamma_{\mathrm{c}} \neq \gamma_{\mathrm{v}} = \gamma_{\mathrm{e}} = \gamma_{\mathrm{h}}$. The glass walls of the chamber is thin so the heat loss across them is not negligible ($\mathcal{T}_{\mathrm{ii}} \neq 0$). They also leak some of the hot products out at locations where they come to contact with the steel body of the burner, but for the simplicity of argument this effect is neglected in this study ($\mathcal{T}_{\mathrm{i}} = 0$). At the same time, both the bleeding stream and the outlet discharge into ambient air, therefore $P_{\mathrm{a}} = P_{\mathrm{d}}$ =1 atm. Lastly there is strong heat release inside the chamber, which is much larger than the acoustic disturbances caused by the upstream plenum. Consequently, the remaining acoustic driving term is dropped.

With these conditions, Eq.(5.15) can be written with the transformation of subscripts {i,v,e}→{1,2,3} as:

$$\frac{d^2 P_2'}{dt^2} + \mathcal{T}_{\mathrm{ii}} \frac{dP_2'}{dt} + (\mathcal{T}_{\mathrm{iii}} + \mathcal{T}_{\mathrm{iv}}) P_2' = \frac{\gamma_{\mathrm{h}} - 1}{V_2} \frac{d\dot{Q}_2}{dt} \,, \tag{5.19}$$

with

$$\mathcal{T}_{\mathrm{ii}} = \frac{\gamma_{\mathrm{h}} - 1}{V_2} \frac{1}{\Omega \rho_{\mathrm{h}} R_{\mathrm{h}}} ,$$

$$\mathcal{T}_{\mathrm{iii}} + \mathcal{T}_{\mathrm{iv}} = \frac{\gamma_{\mathrm{h}} - 1}{\gamma_{\mathrm{c}} - 1} \left(\frac{C_{\mathrm{c}}^2 A_1}{V_2 l_1} \right) + \left(\frac{C_{\mathrm{h}}^2 A_3}{V_2 l_3} \right) .$$

If we define the combined Helmholtz resonance frequency of combustion chamber as:

$$\omega_2 = \sqrt{\frac{\gamma_{\mathrm{h}} - 1}{\gamma_{\mathrm{c}} - 1} \left(\frac{C_{\mathrm{c}}^2 A_1}{V_2 l_1} \right) + \left(\frac{C_{\mathrm{h}}^2 A_3}{V_2 l_3} \right)} , \tag{5.20}$$

then Eq.(5.19) can be written as:

$$\frac{d^2 P_2'}{dt^2} + 2\zeta_2 \cdot \omega_2 \cdot \frac{dP_2'}{dt} + {\omega_2}^2 \cdot P_2' = \frac{\gamma_{\mathrm{h}} - 1}{V_2} \cdot \frac{d\dot{Q}'}{dt} , \tag{5.21}$$

with

$$\zeta_2 = \frac{\gamma_{\mathrm{h}} - 1}{V_2} \frac{1}{2\omega_2 \Omega \rho_{\mathrm{h}} R_{\mathrm{h}}} \tag{5.22}$$

being the damping ratio of the combustion chamber.

3.3 Wall heat loss modeling

As shown in Eq.(5.22), in current study the damping ratio ζ_2 represents the heat loss across the wall and is directly related to the total thermal resistance Ω. In section 3.1 we stated that the definition of Ω depends on the configuration of the setup.

Here we consider the heat transfer from the hot reacting fluid inside the combustion chamber into the ambience. The glass walls are the intermediate layers between the heat source (flame) and the heat sink (ambience). There are two channels of heat transfer in this process. Through the first channel heat convects from fluid to the wall, then conduct across the wall and pass into the ambience through natural convection (the ambience is quiescent). Through the second channel heat radiates directly from fluid into the ambience. This is because the fused silica windows can be considered as transparent for electromagnetic waves with a wavelength between 200 nm and 4 μm [147]. For a black body radiation source of 2000 K, 85% of its radiated power is at wavelengths below 4 μm. Hence the inference of the glass walls on the radiative heat transfer is small and is neglected. If we denote the thermal resistance through the first channel as Ω_{i} and that of the second channel as Ω_{ii}, with heat circuit analysis [147] we have:

$$\frac{1}{\Omega} = \frac{\dot{Q}_{\mathrm{w}}}{T_{\mathrm{h}} - T_{\mathrm{c}}} = \frac{1}{\Omega_{\mathrm{i}}} + \frac{1}{\Omega_{\mathrm{ii}}} . \tag{5.23}$$

Ω_{i} is determined by the combination of fluid to wall convection coefficient $\eta_{2\mathrm{w}}$, wall conduction coefficient κ_{w}, wall to ambience convection coefficient η_{wa}, as well as wall area A_{w} and thickness l_{w}:

$$\Omega_{\mathrm{i}} = \frac{1}{\eta_{2\mathrm{w}} A_{\mathrm{w}}} + \frac{l_{\mathrm{w}}}{\kappa_{\mathrm{w}} A_{\mathrm{w}}} + \frac{1}{\eta_{\mathrm{wa}} A_{\mathrm{w}}} \ . \tag{5.24}$$

In convection heat transfer analysis it is convenient to represent the heat transfer coefficient η in terms of Nusselt number ($Nu = \eta l/\kappa$), where l is the characteristic length and κ is the heat conduction coefficient of the fluid evaluated at the mean temperature between fluid and wall. Heat transfer from fluid to wall is a forced convection process, the mean Nusselt number for a turbulent flow through a flat plate ($\overline{Nu}_{\mathrm{fc}}$) is [147]:

$$\overline{Nu}_{\mathrm{fc}} = 0.037 Re^{4/5} Pr^{1/3} \ , \tag{5.25}$$

where $Re = Ul/\nu$ is the Reynolds number defined based on the plate length and $Pr = \nu/\alpha$ is the Prandtl number evaluated at the mean temperature at the mean temperature between fluid and wall.

On the other hand, heat transfer from wall to ambience is a natural convection process.The Nusselt number for a natural convection through a vertical plate with a turbulent boundary layer ($\overline{Nu}_{\mathrm{nt}}$) can be calculated by [148]:

$$\overline{Nu}_{\mathrm{nt}} = \left\{ 0.825 + \frac{0.387 Ra^{1/6}}{\left[1 + (0.492/Pr)^{9/16}\right]^{8/27}} \right\}^2 \ , \tag{5.26}$$

where $Ra = g(T_{\mathrm{w}} - T_{\mathrm{a}}) l^3/(\nu \alpha T_{\mathrm{wa}})$ is the Rayleigh number, g is the gravitational constant, T_{wa} is the mean temperature between the wall and the ambience. With these formulations, the convection heat transfer coefficients $\eta_{2\mathrm{w}}$ and η_{wa} can be calculated by $\eta_{2\mathrm{w}} = \overline{Nu}_{\mathrm{fc}} \kappa_{2\mathrm{w}}/l_2$ and $\eta_{\mathrm{wa}} = \overline{Nu}_{\mathrm{nt}} \kappa_{\mathrm{wa}}/l_2$ respectively. Hence Ω_{i} can be calculated from Eq.(5.24).

Since Ω_{ii} represent a single radiation process, it is simply the inverse of the product of radiation heat transfer coefficient and wall area:

$$\Omega_{\mathrm{ii}} = \frac{1}{A_{\mathrm{w}} \cdot \epsilon_{\mathrm{e}} \sigma_{\mathrm{S-B}} (T_{\mathrm{h}}^2 + T_{\mathrm{c}}^2)(T_{\mathrm{h}} + T_{\mathrm{c}})} \ , \tag{5.27}$$

where ϵ_{e} is the emissivity of the fluid and $\sigma_{\mathrm{S-B}}$ is the Stefan-Boltzmann constant ($\sigma_{\mathrm{S-B}} = 5.67 \times 10^{-8} W/m^2 \cdot K^4$).

3.4 Heat release modeling

To solve Eq.(5.21), we need to relate the heat release rate fluctuation to pressure fluctuations. The total heat release rate $\dot{Q}$ can be related to the total mass flow rate ($\dot{m}_{\mathrm{tot}} = \dot{m}_{\mathrm{f}} + \dot{m}_{\mathrm{o}}$) and lower heating value ($\Delta h_{\mathrm{g}}^{\circ}$) of fuel-air mixture by:

$$\dot{Q} = \frac{\Delta h_{\mathrm{g}}^{\circ}}{AFR_{\mathrm{st}}} \cdot \min(\dot{m}_{\mathrm{f}} \cdot AFR_{\mathrm{st}}, \dot{m}_{\mathrm{o}}) \ , \tag{5.28}$$

where equivalence ratio ϕ and stoichiometric air-fuel ratio (AFR_{st}) are related to fuel flow rate ($\dot{m}_{\mathrm{f}}$) and air flow rate ($\dot{m}_{\mathrm{o}}$) by:

$$\phi = \frac{\dot{m}_{\mathrm{f}}}{\dot{m}_{\mathrm{o}}} \cdot AFR_{\mathrm{st}} \ . \tag{5.29}$$

The "minimum" function (min) in Eq.(5.28) is used to consider the fact that at non-stoichiometric conditions, there will be unburnt fuel or air depending on ϕ. Eq. (5.28) follows a simple one step chemistry concept, partial decomposition of fuel and intermediate reactants are not considered for the simplicity of the model.

In a partially premixed setup like the GTMC, fuel is usually separately injected through a high pressure line. If we assume that the pressure oscillations in the combustion chamber have little effect on the fuel feed lines, then fuel flow rate can be regarded as being constant. If we further decompose the variables in Eq.(5.28) into mean ($\overline{\dot{x}}$) and fluctuation($\dot{x}'$) by $x = \overline{x} + x'$, with $\overline{x'} = 0$, then from Eq.(5.28) we can derive the heat release fluctuation equation in terms of ϕ and $\dot{m}_{\mathrm{o}}$:

$$\dot{Q}' = \frac{\Delta h_{\mathrm{g}}^{\circ}}{AFR_{\mathrm{st}}} \cdot \left[\left(\min(\phi, 1) - \overline{\min(\phi, 1)} \right) \cdot \overline{\dot{m}_{\mathrm{o}}} + \left(\min(\phi, 1) \cdot \dot{m}_{\mathrm{o}}' - \overline{\min(\phi, 1) \cdot \dot{m}_{\mathrm{o}}'} \right) \right] \ . \tag{5.30}$$

Depending on the value of equivalence ratio, specifically the value of $\min(\phi, 1)$, it can be shown that Eq.(5.30) can simplified to:

$$\dot{Q}' = \begin{cases} 0 & \text{if } \max(\phi) < 1 \\ \text{intermittent} & \text{if } \min(\phi) < 1,\ \max(\phi) > 1 \\ \dfrac{\Delta h_{\mathrm{g}}^{\circ}}{AFR_{\mathrm{st}}} \cdot \dot{m}_{\mathrm{o}}' & \text{if } \min(\phi) > 1 \end{cases} \tag{5.31}$$

In the cases where we have non-zero heat release rate fluctuations in a rich mixture, Eq. (5.31) indicates that $\dot{Q}'$ is directly proportional to air mass flow rates. In the present model, the fluctuation of mass flow rate can be related to the fluctuation of swirler exit velocity (U_1') with a convection time delay (τ_{c}):

$$\dot{m}_{\mathrm{o}}' = U_1'(t - \tau_{\mathrm{c}}) \cdot \rho_{\mathrm{c}} \cdot A_1 \ . \tag{5.32}$$

Again, the complex flow pattern across the swirler veins in the injector are neglected. Following the same procedure as shown in the derivation of Eqs.(5.9) and (5.10), we have:

$$\frac{d\dot{Q}'}{dt} = \frac{\Delta h_{\mathrm{g}}^{\circ}}{AFR_{\mathrm{st}}} \frac{d\dot{m}_{\mathrm{o}}'}{dt} = \frac{\Delta h_{\mathrm{g}}^{\circ}}{AFR_{\mathrm{st}}} \frac{A_1}{l_1} \cdot (P_0' - P_2')|_{t - \tau_{\mathrm{c}}} \ . \tag{5.33}$$

3.5 Determination of convection time delay τ_c

The convection time delay τ_c represents the time for the fuel to travel to the flame location after being injected. In a ideal zero-dimensional framework, we assume the uniformity of properties in combustion chamber and hence the flame lift-off height is zero. Therefore there should not be any convection time delay. However, we are aware that a convection delay is realistic phenomenon and an important part of the dynamic process of instability described by Eq.(5.39). So we have to create this concept using some of the multi-dimensional arguments in the context of a zero-dimensional framework. The time delay is just a single number without any spatial or temporal dependency, so in a dimensional sense it should be consistent with the zero-dimensional assumption.

In this model τ_c is estimated to be the ratio of mean lift-off height $\overline{H}_{lo}$ and mean injector exit velocity $\overline{U}_1$:

$$\tau_c = \frac{\overline{H}_{lo}}{\overline{U}_1} \ . \tag{5.34}$$

The mean lift-off height is estimated by the assumptions that: *i*) the axial velocity magnitude decreases along the height of the combustion chamber, the rate of decrease is that of an axial jet ($\sim x^{-1}$) [149]; *ii*) flame is stabilized at the location where the local mean velocity equals to the turbulent burning velocity of the fuel s_T; *iii*) the turbulent burning velocity is assumed to be constant despite the local perturbations. With these assumptions, $\overline{H}_{lo}$ can be calculated as:

$$\overline{H}_{lo} = H_{ref} \cdot \left(\frac{\overline{U}_1}{s_T} \right) \ , \tag{5.35}$$

where H_{ref} is a reference length scale. We can then rewrite Eq.5.34 into:

$$\tau_c = H_{ref} \cdot \left(\frac{\overline{U}_1}{s_T} \right) \cdot \frac{1}{\overline{U}_1} = \frac{H_{ref}}{s_T}, \tag{5.36}$$

which means that by our assumptions the convection time delay is independent of mean flow velocity. It is only a function of turbulent burning velocity, which is a function of equivalence ratio and local velocity fluctuation magnitude. However, as aforementioned, these effects are not considered currently and s_T is considered to be constant for a given equivalence ratio.

3.6 Summary of the governing equations

By this step, we have individually derived the pressure governing equation of combustion chamber as well as the heat release term. We can couple them by substitute Eqs. (5.31) and (5.33) into Eq. (5.21), we have:

$$\frac{d^2 P_2'}{dt^2} + 2\zeta_2 \cdot \omega_2 \cdot \frac{dP_2'}{dt} + {\omega_2}^2 \cdot P_2' = \mathcal{L} \cdot \Theta \cdot (P_0' - P_2')|_{t-\tau_c} \ , \tag{5.37}$$

with $\mathcal{L}$ representing all burner-specific parameters:

$$\mathcal{L} = \frac{\gamma_h - 1}{V_2} \cdot \frac{A_1}{l_1} ,$$

and Θ representing all parameters that are fuel specific:

$$\Theta = \frac{\Delta h_g^\circ}{AFR_{st}} .$$

Now we make the assumption that the pressure in the plenum and the combustion chamber are sinusoidal:

$$P_0' = |P_0'| \cdot \exp(\jmath\omega t) , \quad P_2' = |P_2'| \cdot \exp\left(\jmath(\omega t - \psi_{20})\right) , \tag{5.38}$$

where ψ_{20} is the phase angle between P_0' and P_2'. This should be reasonable for a normal Helmholtz analysis, and this will be verified in the later sections. Substitute Eq. (5.38) into Eqs. (5.18) and (5.37), we would obtain:

$$-\omega^2 + {\omega_0}^2 = {\omega_0}^2 \cdot \mathcal{P} , \tag{5.39a}$$

$$-\omega^2 + 2\zeta_2 \cdot \omega_2 \cdot \jmath\omega + {\omega_2}^2 = \mathcal{L} \cdot \Theta \cdot \exp(-\jmath\omega_r \tau_c) \cdot (1/\mathcal{P} - 1) , \tag{5.39b}$$

where $\mathcal{P}$ is the complex ratio of the two pressure fluctuations defined as:

$$\mathcal{P} = \frac{P_2'}{P_0'} = \frac{|P_2'|}{|P_0'|} \cdot \exp(\jmath\psi_{20}) . \tag{5.40}$$

In Eq. (5.39) the only unknowns are the system instability frequency ω and complex pressure ratio $\mathcal{P}$, all other parameters can be estimated from the configuration and operating conditions that this model is applied to. Hence mathematical closure is achieved. If we further eliminate $\mathcal{P}$ in Eq.(5.39b) with Eq.(5.39a), then we have the governing equation for combustion instability ω alone:

$$-\omega^2 + 2\zeta_2 \cdot \omega_2 \cdot \jmath\omega + {\omega_2}^2 = \mathcal{L} \cdot \Theta \cdot \exp(-\jmath\omega_r \tau_c) \cdot \left(\frac{\omega^2}{\omega_0^2 - \omega^2}\right) . \tag{5.41}$$

4 Model Predictions and Comparisons with Experimental Observations

4.1 Model parameters for the GTMC

To solve Eq.(5.41) we need to provide or estimate a series of parameters. Geometric parameters based on the dimensions of the GTMC are provided in table 5.4 along with some of the thermodynamic parameters.

Table 5.4: Model parameters used in present study

Component	Plenum	Injector	Chamber	Chimney
Subscript	0	1	2	3
Length (l) [cm]	6.5	3.6	11.0	5.0
Diameter (D) [cm]	7.90	2.37*	8.50†	4.00
Cross-sectional area (A) [cm^2]	49.0	4.4	72.3	12.6
Volume (V) [cm^3]	319	16	795	63
Temperature (T) [K]	294	294	2000	2000
Ratio of heat capacities (γ)	1.4	1.4	1.3	1.3
Speed of sound (C) [m/s]	344	344	864	864

* D_1 is calculated as the equivalent diameter combining both the inner and outer swirler.
† The combustion chamber has a square cross section and D_2 is the length of its edge.

The lower heating value of DME is chosen to be $\Delta h_{\mathrm{g}}^{\circ} = 27.6$ MJ/kg [150]. In this work the reference length H_{lo} is taken as the estimated lift-off height of 5 mm. Turbulent burning velocity s_{T} is estimated to be 5 m/s, which is about 10 times larger than the corresponding laminar burning velocity of DME at $\phi = 1.2$. This results in a convection time scale $\tau_{\mathrm{c}} \approx 1$ ms. In addition, the Helmholtz resonance frequencies of plenum and combustion chamber are calculated using Eqs.(5.17) and (5.20):

$$\omega_0 = \sqrt{\frac{C_{\mathrm{c}}^2 A_1}{V_0 l_1}} = 2129 \text{ rad/s} \approx 339 \text{ Hz} ,$$

$$\omega_2 = \sqrt{\frac{\gamma_{\mathrm{h}} - 1}{\gamma_{\mathrm{c}} - 1}\left(\frac{C_{\mathrm{c}}^2 A_1}{V_2 l_1}\right) + \left(\frac{C_{\mathrm{h}}^2 A_3}{V_2 l_3}\right)} \approx 796 \text{ Hz} .$$

The calculation of damping ratio involves calculating the heat transfer coefficients. With an estimated mean axial velocity U_2 of 10 m/s and gas properties evaluated at 2000 K, the Reynolds number based on the length of the combustion chamber is about 2780. The Prandtl number at 2000 K is estimated to be 0.672, hence the forced convection average Nusselt number ($\overline{Nu}_{\mathrm{fc}}$) between fluid and wall is determined to be 18.47 with Eq.(5.25). If we estimate the surface temperature of the glass wall to be 500 K, then the natural convection Nusselt number between wall and ambience is determined to be 27.81. With these parameters, the non-radiation thermal resistance Ω_{i} defined in Eq.(5.24) is 2.81 K/W. The radiation thermal resistance Ω_{ii} is 0.1 K/W, if the emissivity is estimated to be 0.5. This calculation tells us that the major channel of heat transfer in the current setup is heat radiation as the radiation thermal resistance is much smaller than the non-radiation thermal resistance. The total thermal resistance Ω is 0.1 K/W and the calculated damping ratio ζ_2 from Eq.(5.22) is then 0.016.

4.2 Benchmark at case R1

With the the parameters determined in the previous section, we can use the proposed model to predict the trends in the changes of combustion instability frequency when certain parameters of the system is changed and compare them with the experimental data. Before that, we need to establish a benchmark case to serve as a reference value for later comparisons.

Here case R1 is chosen as the benchmark case, because it is the most distinctly unstable case with our test matrix. Equation 5.39 is solved with the parameters stated in the previous sections. The solution contains two variables: the complex instability frequency ω and complex pressure ratio $\mathcal{P}$. The real part of ω, ω_r is the instability frequency observable by experiments. The magnitude of $\mathcal{P}$, $|\mathcal{P}|$, is the ratio of the pressure amplitude in plenum and combustion chamber. The complex phase angle of $\mathcal{P}$, ψ_{20}, is the phase angle between the pressure in plenum and combustion chamber. These predicted variables are compared with experimental data in Chen and Driscoll [143] and the results are shown in table 5.5.

Table 5.5: Comparison of instability frequency between predictions of proposed model and experimental data for case R1.

	Model prediction	Experiment*	Difference
ω_r	329 Hz	330 Hz	¡ 0.3%
$\|\mathcal{P}\|$	0.63	0.5	¡ 26%
ψ_{20}	76°	50°	¡ 52%

* Data from Chen and Driscoll [143], with a different combustion chamber wall configuration, see discussions in text.

The reason that we chose the data in reference rather from the current study is that we do not have a simultaneous measurement of plenum pressure and combustion chamber pressure in the current work. In our setup such measurement requires that one of the combustion chamber to be replaced with a steel wall, which was done in Chen and Driscoll [143]. The difference in combustion instability frequency between current study and Chen & Driscoll (320 Hz vs. 330 Hz) is discussed in section 4.5.

From table 5.5 we can see that the proposed model accurately predicted the instability frequency. Even compared to the present measured instability frequency of 320 Hz, the difference is still within 3%. The predictions of complex pressure ratio $\mathcal{P}$ have larger deviations from experiment data. Specifically, the magnitude of the pressure ratio is 40% smaller and the phase angle is 50% larger than the experiment. Such discrepancies can be caused by a variety of reasons. Firstly the proposed reduced order greatly simplified the physical processes involved. For example, the complex geometry in the dual-swirler is neglected, which may have a effect over the interactions between the pressure in plenum and combustion chamber. Secondly, experimental measurement uncertainties have to be taken into consideration.

Even considering the differences, we can see that the proposed model is able to provide predictions that are in the same range as the experimental observations with fist order accuracy. This prediction is then established as the reference value for studies in the next sections.

4.3 Effect of varying the dimensions of the GTMC

With all the parameters estimated at the reference point (case R1, DME flame, $\phi = 1.2$, $\dot{m}_o = 282$ g/min), we can start to explore the effect of changing geometric parameters of the GTMC in our model and compare the results with the experimental data provided by Allison et al. [132].

The first parameter we explore is the plenum volume V_0. The model is evaluated for a range of different plenum volumes as determined by the experimental data. The normalized result is shown in figure 5.9.

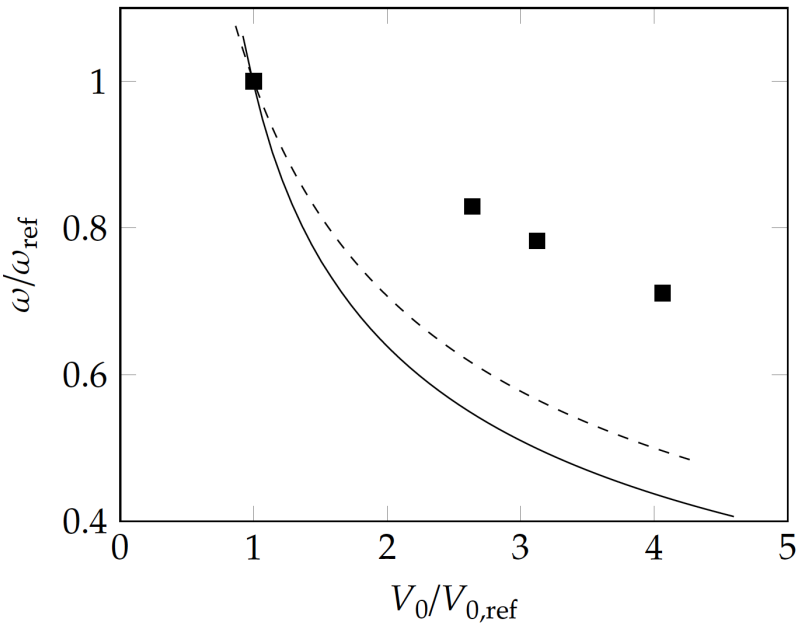

Figure 5.9: Effect of varying plenum volume V_0 on the instability frequency: solid squares are experimental data by Allison et al. [132], solid line is prediction made by, dashed line is predictions of classical Helmholtz theory.

In figure 5.9 it shows that our prediction follows the same trend as the experimental data. Specifically the instability frequency decreases as the volume of plenum increases. This is expected because from Helmholtz analysis we know that as plenum volume increases, the characteristic frequency will decrease. Since our combustion instability frequency is dependent on the Helmholtz frequency of the plenum, it should also decrease.

For reference, in figure 5.9 the prediction of an ideal Helmholtz resonance frequency for plenum is also plotted (the dashed line). We can see that our prediction is closer to the ideal Helmholtz resonator than experimental data. The remaining difference between our model prediction and the Helmholtz theory lies in the fact that the predicted instability is affected not only by the plenum, but also by the combustion chamber. Also, in most of the time the instability frequency is not at the resonance frequency of either chamber, hence its deviation from Helmholtz resonance frequency prediction of plenum is understandable.

The difference between our model prediction and experimental data lies at the slope of the curve. Our model as well as Helmholtz theory predicts that frequency decreases at a rate of $V_0^{-0.5}$ whereas in the experimental data the frequency decreases at a rate of $V_0^{-0.25}$. Sensitivity analysis has been conducted and we found that varying ζ_2 would not mitigate this discrepancy. We have also varied the value of τ_c from 1 ms to 2 ms. Even though the magnitude of the predicted frequency gets closer to the corresponding experimental value, the difference of slope is still evident. We suspect experimental uncertainty may play a part in this disagreement.

Next we examine the effect of changing the dimensions of the chimney over the instability frequency. Allison et al. [132] stated that the instability frequency has a dependence over the geometry of the chimney. In figure 5.10 the predicted results of are compared against Allison's data on a normalized base.

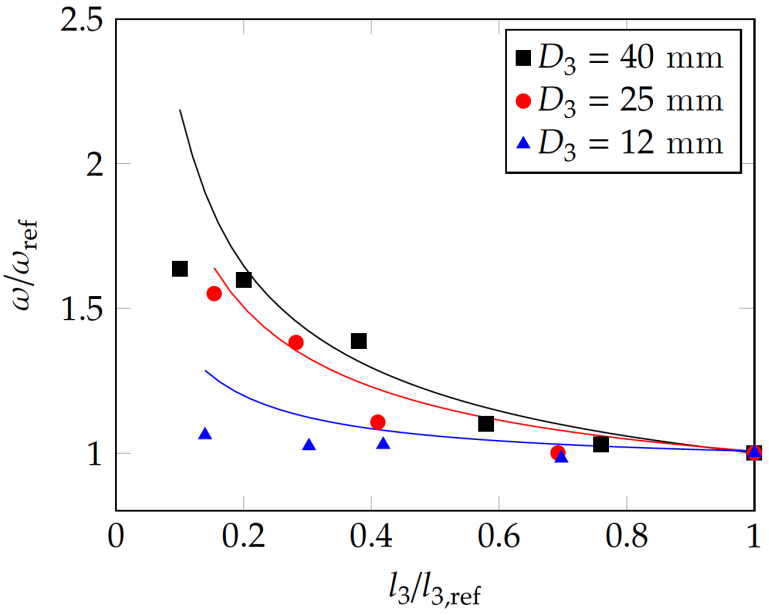

Figure 5.10: Effect of varying chimney length l_3 on the instability frequency at different chimney diameter (D_3): solid squares are experimental data by Allison et al. [132], solid line is the prediction made by proposed reduced order model.

If the combustion instability frequency is purely attributed to the influence of the plenum,

then the change in chimney would have no effect on the instability. From experimental data we can see that this is clearly not the case, and because our model considers the interaction between plenum and combustion chamber, the effect of the chimney is captured. We can see from figure 5.10 that our model predictions adequately captured the trend when chimney diameter and length are changed.

In Allison et al.'s paper [132], it was reported that the change of combustion chamber length from 30% to 300% of its original length results in less than 5% of change in measured combustion instability frequency. The predictions of the reduced order model in the same range of combustion chamber lengths are shown in figure 5.11.

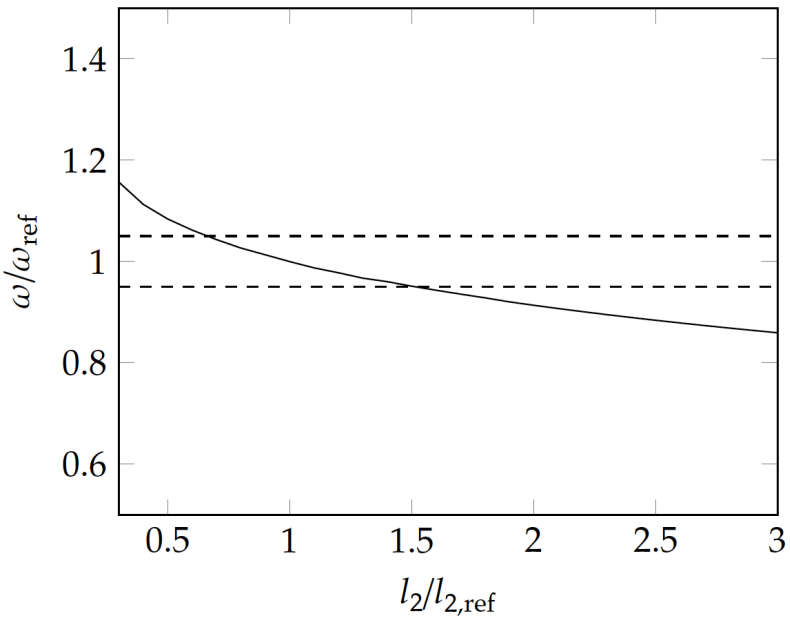

Figure 5.11: Effect of varying combustion chamber length l_2 on the instability frequency: solid line is the prediction made by proposed reduced order model, dashed lines are the range of frequencies measured by Allison et al. [132].

The proposed model predicts that the instability frequency decreases as the combustion chamber length is increased. Within ±50% of the reference value of l_2 the frequency remains within ±5% of the original instability frequency. At three times the original combustion chamber length, the instability frequency decreases to about 90% of the original value. Even though the change in our model prediction is larger, the results of the model agree reasonably well with the experimental observations, i.e., the system instability frequency is insensitive to the change of combustion chamber volume.

In this first part of this section we see that the instability frequency is sensitive to plenum volume and chimney dimensions. This is because these parameters are directly affecting the Helmholtz frequency of plenum (ω_0) and combustion chamber (ω_2), which are the important

coefficients in Eq.(5.39). The changes in combustion chamber length and hence its volume will also affect ω_2. However because V_2 is also present on the right hand side of Eq.(5.39b), the effects of change in ω_2 is partially offset. This results in the relative insensitivity of ω on l_2 and V_2.

4.4 Effect of varying equivalence ratio

In section 2.5 we summarized our experimental observations of the change in system dynamics as the equivalence ratio is changed. Similar to the observations made by Allison et al. [133], the fuel-lean flame L1 with $\phi = 0.75$ was considered to be "stable" because of its very small pressure oscillation. The flame S1 with $\phi = 1.0$ was considered as "intermittent" because of its intermittent pressure fluctuations, while the flame R1 with $\phi = 1.2$, is considered as "unstable" because of its very large pressure fluctuations.

To predict the influence of equivalence ratio on combustion instability, we need to look into the heat release term of the governing equation. We summarized the heat release model for partially premixed flame with direct fuel injection in Eq.(5.31). This equation states that when the mixture is very lean ($\max(\phi) < 1$), the heat release rate is constant, and its fluctuation is zero. Considering that the heat release rate fluctuation is the driving force for combustion chamber pressure fluctuation, which in turn drives plenum pressure fluctuations, $\dot{Q}' = 0$ means that Eq. (5.39b) will have a trivial solution of $P'_* = 0$. This in reality means that there will not be combustion instability present.

By the same logic, Eq. (5.31) predicts that if the mixture is near stoichiometric, the flame will be unstable in the instances when it is fuel rich, while the flame stays stable in the instances when it is lean. Hence this will produce a "intermittently" unstable flame. Lastly, if the mixture is very rich in fuel, the flame will be continuously driven by the fluctuating heat release rate and become unstable. This difference is illustrated in figure 5.12.

Our model prediction describes precisely what we were observing in our experiment. In other words, from our model we propose the hypothesis that the flame instability in is controlled by the deficient stream (fuel or air) flow rate. At the same time, we have to fully understand that such hypothesis is based on the assumption that: *i*) the chemistry involved is a one-step reaction, there is no partial fuel decomposition; *ii*) all chemical reactions are much faster compared to the flow residence time (Damköhler number is infinite); *iii*) heat release is not affected by the mean flow rate or turbulence levels, for example blow-out is not considered; and *iv*) the incoming fuel flow rate is constant and there is no fuel-trapping near the injection nozzle due to complex flow interactions. Some of these assumptions are very likely violated in the , but our proposed model nonetheless provides a theoretical base to understand fundamental physical processes in this burner.

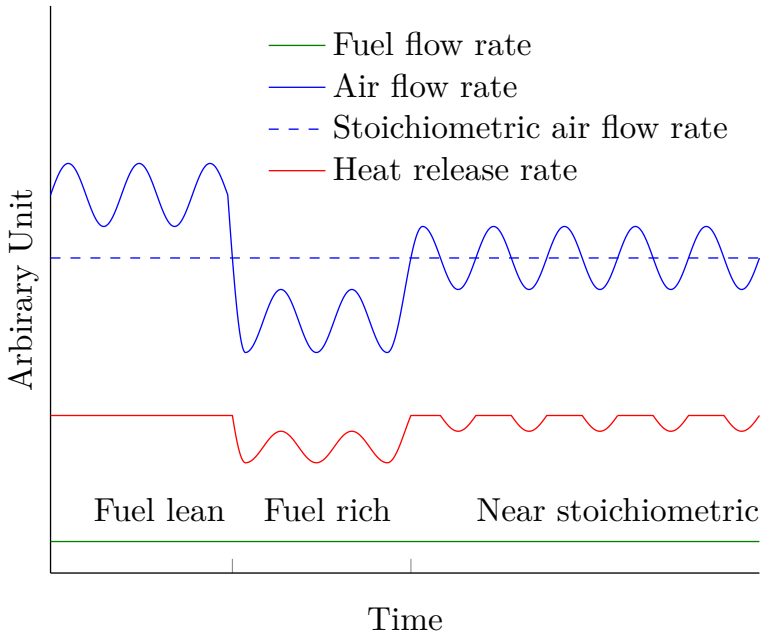

Figure 5.12: Prediction of Eq.(5.31) on the existence of combustion instability under different equivalence ratio values

4.5 Effect of combustion chamber wall configuration

Experimentally it has been found that the configuration of the walls affects the resulting frequency. For example, in the study of Allison et al. [133] (figure 3), the pressure measurement was done with three steel walls and one glass wall, and for case R1 the frequency was about 360 Hz. In the study by Chen and Driscoll [143] the configuration consisted of three glass walls and one steel wall, and the resultant frequency was around 330 Hz. In present study, the combustion chamber has four glass walls and the measured instability frequency is about 320 Hz.

Physically, the configuration of walls can affect the combustion instability in two ways. Firstly, the heat transfer mechanism between the fluid inside the combustion chamber and ambience will be altered. In section 3.3 we discussed the heat transfer process across a glass wall, the conclusion is that heat can pass across the glass wall via convection/conduction or directly through the wall via radiation. Calculations in section 4.1 reveals that in operating condition R1 the wall heat loss mainly results from radiation. If a glass wall is replaced with a steel wall, then the wall will be opaque to radiation instead of being transparent. In this case the most important heat transfer mechanism from fluid to outside will be that of convection.

Secondly, in the case of a glass wall, there will be gas leakage from the gaps between the glass and the grove of the burner pillar. Such gap is tightly filled when a steel wall is

installed. In our single chamber Helmholtz resonator analysis in section 3.1 we considered the effect of bleeding holes on the wall of a resonator, the conclusion was that fluid leakage will add another term for the damping term. Since the exact area of the gap is very difficult to estimate or measure, and the total leakage mass flow rate is believed to be small, we neglected this effect in this study.

Since the effect of wall configurations on combustion instability is multi-fold and depends much on the specific conditions of the burner such as manufacturing precisions. An exact prediction of by the proposed model is difficult. Nonetheless, since we acknowledge that the wall configurations will change the damping ratio ζ_2, we solved the governing equation Eq.(5.41) through a range of ζ_2 values and plotted the solution of instability frequency ω against that of the pressure ratio $|\mathcal{P}|$ as shown in figure 5.13. The values of experimentally measured instability frequency for different wall configurations are also plotted onto the same figure.

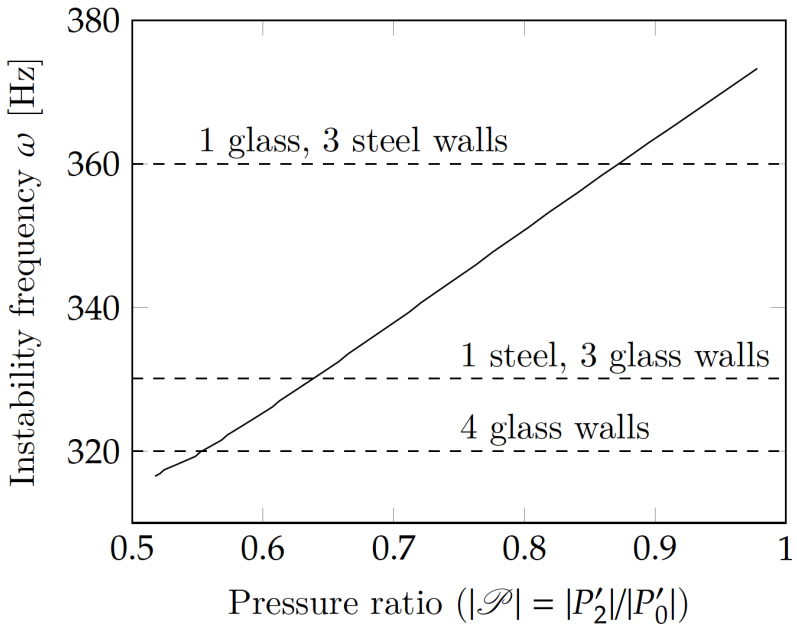

Figure 5.13: Relationship between predicted instability frequency ω and predicted combustion chamber / plenum pressure ratio ($|\mathcal{P}|$), dashed lines show the measured instability frequency for case R1 with different combustion chamber wall configurations.

The proposed model predicts that instability frequency is proportional to pressure ratio inside the combustion chamber. Since experimentally it is shown that more steel walls result in higher instability frequency, that leads to the prediction that as more steel walls are installed, the pressure inside the combustion chamber approaches that of the plenum.

4.6 Effect of varying mass flow rate

There is no explicit dependence on air mass flow rate in our governing equation Eq.(5.41). However, the air mass flow rates, and hence the mean velocity does play a key role in determining the damping term in the equations. Specifically, as the mass flow rate increases, the Reynolds number in the combustion chamber increase proportionally. This will result in a increase in the convection heat transfer coefficient. Another aspect that mass flow rate may affect the system is through friction loss. As the velocity magnitude increase, the wall shear stress also increases. In our previous analysis we neglected the latter process for simplicity.

Let's only consider the effect of mass flow rate on heat transfer. In section 4.1 it was shown that for glass walls the major heat transfer mechanism is radiation, which is independent of gas velocity. If we consider the case where all walls made of steel, as the case in measurements made by Allison et al [133], then convection will be the dominant heat transfer mechanism. In this case, we can calculate the dependence of predicted instability frequency on mass flow rates through the change of damping ratio ζ_2, as shown in figure 5.14.

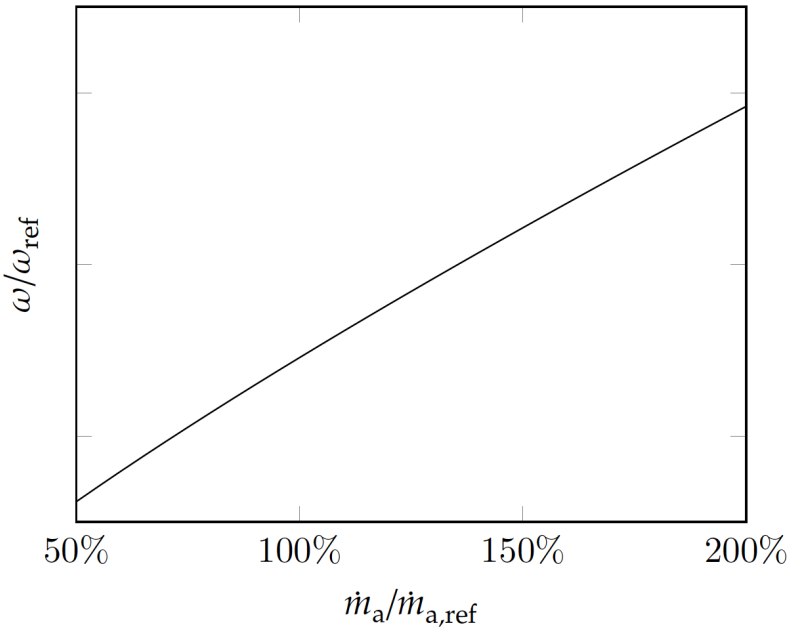

Figure 5.14: Dependence of predicted instability frequency ω on air mass flow rate $\dot{m}_{\text{a}}$.

From figure 5.14 we can see that the predicted instability frequency increases monotonically with the increase of air flow rates. This agrees with the experimental observations made by Allison et al. for different fuels.

5 Summary and Conclusions

The DLR gas turbine model combustor (GTMC) was operated with DME fuel at four operating conditions: rich (R1), lean (L1), stoichiometric (S1), and reduced flow rate (R2). Highspeed PIV-PLIF-pressure measurements were carried out at a sustained frequency of 4kHz. The flow structures and the spectrum of pressure, heat release, and velocity vectors were thus investigated. Thereafter a reduced order model based on multi-chamber Helmholtz analysis was proposed based on the experimental observations. Supplied with the realistic values of GTMC for its parameters, the model is used to predict the instability frequency and complex pressure ratio at a fixed operating condition (case R1). It was also used to explore the effect of geometry, equivalence ratio, and mass flow rate on combustion instability.

We conclude that:

- The PLIF data showed that the spectrum of flame surface density oscillations has a sharp spike at the same frequency as the spike in the pressure spectrum. This proves that the heat release rate is coupled to the pressure fluctuations. The kilohertz PIV data showed that the velocity field also has a peak at the instability frequency in unstable flames. This allows us to measure the relative phases between these quantities if proper spectral filtering is applied.

- Velocity spectrum analysis in this study revealed that the effect of combustion instability would change the axial and radial velocity distribution as well. In an unstable flame the major dynamics happened in the radial direction, with velocity undergoing a large oscillation radially. In a stable flame the velocity oscillation was more evenly distributed between axial and radial directions.

- In a quiet flame where PLIF and pressure measurements show no signs of thermoacoustic instability, PIV identified large velocity fluctuations caused by the PVC. This supports our hypothesis that mass flow rates oscillation alone does not necessarily result in acoustic instability.

- Unlike the MIT model that only considers the combustor chamber or the EM2C model that requires experimental calibration, the proposed reduced order model utilizes a set of coupled ODEs that consider a system with two volumes (plenum and combustion chamber) and two constrictions (injector and chimney).The measured frequency agrees with the frequency predicted by the proposed model.

- The model at its current form is tailored to model the GTMC specifically. It needs to be modified to model other setups. Additionally, its current form only considers Helmholtz-type instability and flat flames. If other target burners have different physics, the model will need to be extended before application.

- The reduced order model successfully explained most, but not all of the experimental data. The model is not predictive, but it shows that if a reasonable value of acoustic

damping is estimated, several of the trends computed by the model are similar to the measured trends.

- The model provides an explanation to the dependence of combustion instability on equivalence ratios. It hypothesizes that the heat release rate is controlled by the flow rate of the deficient stream. If the fuel flow rate is constant, then in all fuel lean conditions the heat release rate stays constant and combustion instabilities will not occur. This idea is an extension to existing equivalence ratio oscillation theories. It is only valid if we ignore the effect of fluid dynamics on the flame and assume one-step chemistry. Hence its predictions are not general and should be confined to the present operating conditions of the GTMC.

- Previous experimental data shows that the instability frequency also depends linearly on laminar flame speed, which the current model is not capable of explaining. More research is needed to expand the model to account for this parameter.

Chapter 6

Publications

1 PhD Thesis

- Yuntao Chen, "Investigation of Partially Premixed Combustion Instabilities through Experimental, Theoretical, and Computational Methods." Department of Aerospace Engineering, University of Michigan. Advisors: James F. Driscoll and Matthias Ihme.
- Yee Chee See, "Analysis of Hydrodynamic Instabilities and Combustion Dynamics in Turbulent Reacting Flows." Department of Aerospace Engineering, University of Michigan. Advisor: Matthias Ihme.
- Patton M. Allison, "Experimental Characterization of Combustion Instabilities and Flow-Flame Dynamics in a Partially-Premixed Gas Turbine Model." Department of Aerospace Engineering, University of Michigan. Advisors: James F. Driscoll and Matthias Ihme.

2 Journal Articles

- Matthias Ihme, "On the role of turbulence and compositional fluctuations in rapid compression machines: Autoignition of syngas mixtures." Combustion and Flame, 159, 1592-1604, 2012.
- See, Y. C. and Ihme, M., "Large eddy simulation of a partially-premixed gas turbine model combustor." Proceedings of the Combustion Institute, 35, 2015, 1225-1234.
- Grogan, K. P., Goldsborough, S. S., and Ihme, M., "Ignition regimes in rapid compression ma-chines." Combustion and Flame, 2015, 162, 3071-3080.
- Wu, H. and Ihme, M., "Effects of flow-field and mixture inhomogeneities on the ignition dynamics in continuous flow reactors." Combustion and Flame, 161, 9, 2317-2326, 2014.

- Patton M. Allison, Yuntao Chen, Matthias Ihme, and James F. Driscoll, Coupling of Flame Geometry and Combustion Instabilities Based on Kilohertz Formaldehyde PLIF Measurements, Proceedings of the Combust. Inst., Vol. 35, 2014.

- Allison, P.M., Driscoll, J.F., Ihme, M., "Acoustic Characterization of a Partially-Premixed Gas Turbine Model Combustor: Syngas and Hydrocarbon Fuel Comparisons," Proc. Combust. Inst. 34, 3145-3153, 2013.

- David A. Rosenberg, Patton M. Allison, and James F. Driscoll, Method to Measure Flame Index in a Partially-Premixed Gas Turbine Combustor, AIAA paper AIAA 2013-1181. Accepted by Combustion and Flame for journal publication.

- Experimental Studies and Modeling of Acoustic Instabilities in a Gas Turbine Model Combustor, YunTao Chen and James F. Driscoll, Department of Aerospace Engineering, University of Michigan, Ann Arbor, MI 48109, USA, AIAA 2015-1566.

3 Conference Papers

- Simon Weiher and Matthias Ihme, "Characterization of mixing and ignition effects in flow-reactor facilities using a particle method." AIAA-paper 2012-499, presented at 50th AIAA Aerospace Sciences Meeting including the New Horizons Forum and Aerospace Exposition, Nashville, Tennessee, Jan. 9-12, 2012.

- Patton M. Allison, James F. Driscoll, and Matthias Ihme, "Acoustic behavior of a partially-premixed gas turbine model combustor." AIAA-paper 2012-504, presented at 50th AIAA Aerospace Sciences Meeting including the New Horizons Forum and Aerospace Exposition, Nashville, Tennessee, Jan. 9-12, 2012.

- Acoustic Behavior of a Partially-Premixed Gas Turbine Model Combustor, Allison, P., Driscoll, J.F., Ihme, M., AIAA paper AIAA-2012-0504.

- See, Y. C. and Ihme, M., "Investigation of flow field sensitivity in a gas turbine model combus-tor." Paper presented at the AIAA Science and Technology Forum and Exposition (SciTech2014), AIAA 2014-0621, Washington, DC, 2014.

- Patton M. Allison David A. Rosenberg James F. Driscoll, "Combustion Instability Interaction with Fuel-Air Mixing in a Partially-Premixed Gas Turbine Model Combustor," 8th U. S. National Combustion Meeting of the Combustion Institute, May 19-22, 2013.

- Grogan, K., Wang, Q., and Ihme, M., "Modeling gas dynamic effects in shock-tubes for reaction kinetics measurements." Paper presented at the 53rd AIAA Science and Technology Forum and Exposition (SciTech2015), AIAA 2015-0414, Orlanda, FL, 2015.

- Grogan, K., Goldsborough, S. S., and Ihme, M., "Mild ignition phenomena in rapid compression machines." Proceedings of the 25th International Colloquium on the Dynamics of Explosions and Reeactive Systems, August, 2-7, 2015, Leeds, UK.

Bibliography

[1] M. Chaos and F. L. Dryer. Syngas combustion kinetics and applications. *Combust. Sci. Tech.*, 180:1053–1096, 2008.

[2] P. Chiesa, S. Consonni, T. Kreutz, and R. H. Williams. Co-production of hydrogen, electricity and co2 from coal with commercially ready technology. part a: Performance and emissions. *Int. J. Hydrogen Energy*, 30:747–767, 2005.

[3] C.-J. Sung and C. K. Law. Fundamental combustion properties of H_2/CO mixtures: Ignition and flame propagation at elevated pressures. *Combust. Sci. Tech.*, 180:1097–1116, 2008.

[4] K. M. Tait and M. M. McDonald. Recent developments in IGCC technology. *CIM Bulletin*, 87(981):27–35, 1994.

[5] M. M. Johsi and S. G. Lee. Integrated gasification combined cycle - A review of IGCC technology. *Energy Sources*, 18(5):537–568, 1996.

[6] D. M. Todd and R. A. Battista. Demonstrated applicability of hydrogen fuel for gas turbines. In *Proc. of the IchemE Gasification 4 Conference*. Noordwijk, Netherlands, 2000.

[7] P. Chiesa, G. Lozza, and L. Mazzocchi. Using hydrogen as gas turbine fuel. *J. Eng. Gas Turbines Power*, 127:73–80, 2005.

[8] L. He and P. Clavin. Premixed hydrogen-oxygen flames. Part I: Flame structure near the flammability limits. *Combust. Flame*, 93:391–407, 1993.

[9] S. D. Tse, D. L. Zhu, and C. K. Law. Morphology and burning fluxes of expanding spherical flames in H_2/O_2 inert mixtures up to 60 atmospheres. *Proc. Combust. Inst.*, 28:1793–1800, 2000.

[10] C. K. Law. *Combustion Physics*. Cambridge University Press, Cambridge, 2006.

[11] N. Shilling and R. Jones. The response of gas turbines to a co2 constrained environment, 2003. Gasification Technologies Conference.

[12] E. L. Petersen, D. M. Kalitan, A. B. Barrett, S. C. Reehal, J. D. Mertens, D. J. Beerer, R. L. Hack, and McDonell V. G. New syngas/air ignition data at lower temperature and elevated pressure and comparison to current kinetics models. *Combust. Flame*, 149:244–247, 2007.

[13] S. M. Walton, X. He, B. T. Zigler, and M. S. Wooldridge. An experimental investigation of the ignition properties of hydrogen and carbon monoxide mixtures for syngas turbine applications. *Proc. Combust. Inst.*, 31:3147–3154, 2007.

[14] G. Mittal, C. J. Sung, and R. A. Yetter. Autoignition of H2/CO at elevated pressures in a rapid compression machine. *Int. J. Chem. Kinet.*, 38:516, 2006.

[15] G. Mittal, C.-J. Sung, M. Fairweather, A. S. Tomlin, J. F. Griffiths, and K. J. Hughes. Significance of the ho2+co reaction during the combustion of co+h-2 mixtures at high pressures. *Proc. Combust. Inst.*, 31:419–427, 2007.

[16] W. C. Gardiner, M. McFarlan, K. Morinaga, T. Takeyama, and Walker B. F. Initiation rate for shock-heated hydrogen-oxygen-carbon monoxide-argon mixtures as determined by OH induction time measurements. *J. Phys. Chem.*, 75:1504, 1971.

[17] A. M. Dean, D. C. Steiner, and E. E. Wang. Shock-tube study of $H_2/O_2/CO/Ar$ and $H_2/N_2O/CO/Ar$ systems: Measurement of rate constant for $H + N_2O = N_2 + OH$. *Combust. Flame*, 32(1):73–83, 1978.

[18] C. G. Fotache, Y. Tan, C. J. Sung, and C. K. Law. Ignition of CO/H2/N2 versus heated air in counterflow: Experimental and modeling results. *Combust. Flame*, 120:417–426, 2000.

[19] I. Wierzba and V. Kilchyk. Flammability limits of hydrogen-carbon monoxide mixtures at moderately elevated temperatures. *Int. J. Hyd. Energy*, 26:639–643, 2001.

[20] M. O'Conaire, H. J. Curran, J. M. Simmie, W. J. Pitz, and C. K. Westbrook. A comprehensive modeling study of hydrogen oxidation. *Int. J. Chem. Kinet.*, 36:603–622, 2004.

[21] J. Li, Z. Zhao, A. Kazakov, and F. L. Dryer. An updated comprehensive kinetic model of hydrogen combustion. *Int. J. Chem. Kinet.*, 36:566–575, 2004.

[22] M. A. Mueller, R. A. Yetter, and F. L. Dryer. Flow reactor studies and kinetic modeling of the h2/o2/nox and co/h2o/o2/nox reactions. *Int. J. Chem. Kin.*, 31:705, 1999.

[23] S. G. Davis, A. V. Joshi, H. Wang, and F. Egolfopoulos. An optimized kinetic model of H_2/CO combustion. *Proc. Combust. Inst.*, 30:1273–1281, 2005.

[24] I. Gy Zsély, J. Zádor, and T. Turányi. Uncertainty analysis of updated hydrogen and carbon monoxide oxidation mechanisms. *Proc. Combust. Inst.*, 30:1273–1281, 2005.

[25] F. L. Dryer and M. Chaos. Ignition of syngas/air and hydrogen/air mixtures at low temperatures and high pressures: Experimental data interpretation and kinetic modeling implications. *Combust. Flame*, 152:293–299, 2008.

[26] S. M. Walton, X. He, B. T. Zigler, and M. S. Wooldridge. An experimental investigation of the ignition properties of hydrogen and carbon monoxide mixtures for syngas turbine applications. *Proc. Combust. Inst.*, 31:3147–3154, 2007.

[27] D. F. Davidson and R. K. Hanson. Recent advances in shock tube/laser diagnostic methods for improved chemical kinetics measurements. *Shock Waves*, 19:271–283, 2009.

[28] M. Chaos and F. L. Dryer. Chemical-kinetic modeling of ignition delay: Considerations in interpreting shock tube data. *Int. J. Chem. Kinet.*, 42:143–150, 2010.

[29] J. F. Griffiths, Q. Jiao, W. Kordylewski, M. Schreiber, J. Meyer, and K. F. Knoche. Experimental and numerical studies of ditertiary butyl peroxide combustion at high pressures in a rapid compression machine. *Combust. Flame*, 93:303–315, 1993.

[30] D. Lee and S. Hochgreb. Rapid compression machines: Heat transfer and suppression of corner vortex. *Combust. Flame*, 114:531–545, 1998.

[31] J. Würmel and J. M. Simmie. CFD studies of a twin-piston rapid compression machine. *Combust. Flame*, 141:417–430, 2005.

[32] G. Mittal and C.-J. Sung. Aerodynamics inside a rapid compression machine. *Combust. Flame*, 145:160–180, 2006.

[33] C. Strozzi, J. Sotton, A. Mura, and M. Bellenoue. Characterization of a two-dimensional temperature field within a rapid compression machine using a toluene planar laser-induced fluorescence imaging technique. *Meas. Sci. Technol.*, 20:125403, 2009.

[34] P. Guibert, A. Keromnes, and G. Legros. An experimental investigation of the turbulence effect on the combustion propagation in a rapid compression machine. *Flow, Turb. Combust.*, 84(1):79–95, 2010.

[35] J. E. Elsworth, W. W. Haskell, and I. A. Read. Non-uniform ignition processes in rapid-compression machines. *Combust. Flame*, 13:437–438, 1969.

[36] D. R. Lancaster. Effects of engine variables on turbulence in a spark-ignition engine. *SAE Paper 760159*, pages 671–688, 1976.

[37] R. J. Tabaczynski, D. P. Hoult, and J. C. Keck. High Reynolds numer flow in a moving corner. *J. Fluid Mech.*, 42:249–255, 1970.

[38] J. C. R. Hunt and D. J. Carruthers. Rapid distortion theory and the 'problems' of turbulence. *J. Fluid Mech.*, 212:497–532, 1990.

[39] C. Cambon and J. F. Scott. Linear and nonlinear models of anisotropic turbulence. *Annu. Rev. Fluid Mech.*, 31:1–53, 1999.

[40] I. Hadžić and K. Hanjalić. Modeling the response of turbulence subjected to cyclic irrotational strain. *Phys. Fluids*, 13(6):1739–1747, 2001.

[41] M. T. Donovan, X. He, B. T. Zigler, T. R. Palmer, M. S. Wooldridge, and A. Atreya. Demonstration of a free-piston rapid compression facility for the study of high temperature combustion phenomena. *Combust. Flame*, 137:351–365, 2004.

[42] T. Poinsot and D. Veynante. *Theoretical and Numerical Combustion*. R.T. Edwards, Inc., Philadelphia, PA, 2001.

[43] P. A. Durbin and B. A. Pettersson Reif. *Statistical Theory and Modeling for Turbulent Flows*. John Wiley & Sons, Inc., 2001.

[44] J. C. R. Hunt. A review of the theory of rapidly distorted turbulent flows and its applications. *Fluid Dyn. Trans.*, 9:121–152, 1977.

[45] A. M. Savill. Recent developments in rapid-distortion theory. *Annu. Rev. Fluid Mech.*, 19:531–575, 1987.

[46] S. B. Pope. *Turbulent Flows*. Cambridge University Press, Cambridge, 2000.

[47] R. O. Fox. *Computational Models for Turbulent Reacting Flows*. Cambridge University Press, Cambridge, 2003.

[48] N. Peters. *Turbulent Combustion*. Cambridge University Press, Cambridge, 2000.

[49] S. Tanaka, F. Ayala, and J. C. Keck. A reduced chemical kinetic model for HCCI combustion of primary reference fuels in a rapid compression machine. *Combust. Flame*, 133:467–481, 2003.

[50] J. Li, Z. Zhao, A. Kazakov, M. Chaos, F. L. Dryer, and J.J. Scire, Jr. A comprehensive kinetic mechanism for CO, CH_2O, and CH_3OH combustion. *Int. J. Chem. Kinet.*, 39:109–136, 2007.

[51] R. A. Fraser and R. A. Bracco. Cycle-resolved LDV integral length scale measurements investigating clearance height scaling, isotropy, and homogeneity in an I.C. engine. *SAE Paper 890615*, 1989.

[52] M. S. Wooldridge and D. Karwat, 2010. Private communication.

[53] W. T. Peschke and L. J. Spadaccini. Determination of autoignition and flame speed characteristics of coal gases having medium heating value. Report No. EPRI-AP-4291, United Technologies Research Center, 1985.

[54] J. E. Dec. Advanced compression-ignition engines – understanding the in-cylinder processes. *Proc. Combust. Inst.*, 32:2727–2742, 2009.

[55] Y. B. Zeldovich. Regime classification of an exothermic reaction with nonuniform initial conditions. *Combust. Flame*, 39:211–214, 1980.

[56] J. H. Chen, E. R. Hawkes, R. Sankaran, S. D. Mason, and H. G. Im. Direct numerical simulation of ignition front propagation in a constant volume with temperature inhomogeneities: I. Fundamental analysis and diagnostics. *Combust. Flame*, 145:128–144, 2006.

[57] G. Mittal, M. P. Raju, and C.-J. Sung. Computational fluid dynamics modeling of hydrogen ignition in a rapid compression machine. *Combust. Flame*, 155:417–428, 2008.

[58] C. J. Sung and H. J. Curran. Using rapid compression machines for chemical kinetics studies. *Prog. Energy Combust. Sci.*, 44:1–18, 2014.

[59] R. K. Hanson and D. F. Davidson. Recent advances in laser absorption and shock tube methods for studies of combustion chemistry. *Prog. Energy Combust. Sci.*, 44:103–114, 2014.

[60] F. L. Dryer, F. M. Haas, J. Santner, T.I. Farouk, and M. Chaos. Interpreting chemical kinetics from complex reaction-advection-diffusion systems: Modeling of flow reactors and related experiments. *Prog. Energy Combust. Sci.*, 44:19–39, 2014.

[61] P. Pepiot-Desjardins and H. Pitsch. An efficient error-propagation-based reduction method for large chemical kinetic mechanisms. *Combust. Flame*, 154:67–81, 2008.

[62] P. Park and J. C. Keck. Rapid compression machine measurements of ignition delays for primary reference fuels. *SAE Paper 900027*, 1990.

[63] M. Ihme. On the role of turbulence and compositional fluctuations in rapid compression machines: Autoignition of syngas mixtures. *Combust. Flame*, 159(4):1592–1604, 2012.

[64] P.E. Hamlington and M. Ihme. Modeling of non-equilibrium homogeneous turbulence in rapidly compressed flows. *Flow, Turb. Combust.*, 93(1):93–124, 2014.

[65] J. C. Livengood and W. A. Leary. Autoignition by rapid compression. *Ind. Eng. Chem.*, 43:2797–2805, 1951.

[66] J. W. Meyer and A. K. Oppenheim. On the shock-induced ignition of explosive gases. *Proc. Combust. Inst.*, 13:1153–1164, 1971.

[67] D. J. Vermeer, J. W. Meyer, and A. K. Oppenheim. Auto-ignition of hydrocarbons behind reflected shock waves. *Combust. Flame*, 18:327–336, 1972.

[68] K. Fieweger, R. Blumenthal, and G. Adomeit. Shock-tube investigations on the self-ignition of hydrocarbon-air mixtures at high pressures. *Proc. Combust. Inst.*, 25:1579–1585, 1994.

[69] K. Fieweger, R. Blumenthal, and G. Adomeit. Self-ignition of S.I. engine model fuels: A shock tube investigation at high pressure. *Combust. Flame*, 109:599–619, 1997.

[70] H. Yamashita, J. Kasahara, Y. Sugiyama, and A. Matsuo. Visualization study of ignition modes behind bifurcated-reflected shock waves. *Combust. Flame*, 159:2954–2966, 2012.

[71] Y. Uygun, S. Ishihara, and H. Olivier. A high pressure ignition delay time study of 2-methylfuran and tetrahydrofuran in shock tubes. *Combust. Flame*, 161:2519–2530, 2014.

[72] S. M. Walton, X. He, B. T. Zigler, M. S. Wooldridge, and A. Atreya. An experimental investigation of iso-octane ignition phenomena. *Combust. Flame*, 150:246–262, 2007.

[73] A. Mansfield and M. S. Wooldridge. High-pressure low-temperature ignition behavior of syngas mixtures. *Combust. Flame*, 161:2242–2251, 2014.

[74] A. Mansfield, M. S. Wooldridge, H. Di, and X. He. Low-temperature ignition behavior of iso-octane. *Fuel*, 139:79–86, 2015.

[75] C. Strozzi, A. Mura, J. Sotton, and M. Bellenoue. Experimental analysis of propagation regimes during the autoignition of a fully premixed methane-air mixture in the presence of temperature inhomogenieites. *Combust. Flame*, 159:3323–3341, 2012.

[76] H. Wu and M. Ihme. Effects of flow-field and mixture inhomogeneities on the ignition dynamics in continuous flow reactors. *Combust. Flame*, 161, 2014. 2317-2326.

[77] N. Peters, B. Kerschgens, and G. Paczko. Super-knock prediction using a refined theory of turbulence. *SAE Paper 2013-01-1109*, 2013.

[78] Y. B. Zeldovich, V. B. Librovich, G. M. Makhviladze, and G. I. Sivashinsky. On the development of detonations in a non-uniformly preheated gas. *Acta Astronautica*, 15:313–321, 1970.

[79] J. H. Lee, R. Knystautas, and N. Yoshikawa. Photochemical initiation of gaseous detonations. *Acta Astronautica*, 5:971–982, 1978.

[80] J. H. S. Lee. *The Detonation Phenomenon*. Cambridge University Press, Cambridge, 2008.

[81] X. Gu, D. Emerson, and D. Bradley. Modes of reaction front propagation from hot spots. *Combust. Flame*, 133:63–74, 2003.

[82] K. Grogan and M. Ihme. Weak and strong ignition of hydrogen/oxygen mixtures in shock-tube systems. *Proc. Combust. Inst.*, 35(2):2181–2189, 2014.

[83] R. Blumenthal, K. Fieweger, K. H. Komp, and G. Adomeit. Gas dynamic features of self ignition of non diluted fuel/air mixtures at high pressure. *Combust. Sci. Tech.*, 113:137–166, 1996.

[84] R. Sankaran, H. G. Im, E. R. Hawkes, and J. H. Chen. The effects of non-uniform temperature distribution on the ignition of a lean homogeneous hydrogen–air mixture. *Proc. Combust. Inst.*, 30:875–882, 2005.

[85] S. R. Turns. *An Introduction to Combustion: Concepts and Applications*. McGraw Hill, 2000.

[86] H. Di, X. He, P. Zhang, Z. Wang, M. S. Wooldridge, C. K. Law, C. Wang, S. Shuai, and J. Wang. Effects of buffer gas composition on low temperature ignition of iso-octane and n-heptane. *Combust. Flame*, 161:2531–2538, 2014.

[87] G. Mittal. *A Rapid Compression Machine - Design, Characterization, and Autoignition Investigation*. PhD thesis, Case Western Reserve University, January 2006.

[88] W.S. Affleck and A. Thomas. An opposed piston rapid compression machine for pre-flame reaction studies. *Proc. Inst. Mech. Eng.*, 183(19):365–387, 1968.

[89] B. Marks, O. Mathieu, R. Archuleta, E. L. Petersen, J. Bugler, A. Heufer, and H. Curran. Ignition delay time measurements and modeling of n-pentane and iso-pentane at elevated pressures. *AIAA Paper 2013-0160*, 2013.

[90] J. F. Griffiths and B. J. Whitaker. Thermokinetic interactions leading to knock during homogeneous charge compression ignition. *Combust. Flame*, 131:386–399, 2002.

[91] K. H. Casleton, R. W. Breault, and G. A. Richards. System issues and tradeoffs associated with syngas production and combustion. *Combust. Sci. Tech.*, 180:1013–1052, 2008.

[92] G. A. Richards, M. M. McMillian, R. S. Gemmen, W. A. Rogers, and S. R. Cully. Issues for low-emission, fuel-flexible power systems. *Prog. Energy Combust. Sci.*, 21(2):141–169, 2001.

[93] D. M. Kalitan, J. D. Mertens, M. W. Crofton, and E. L. Petersen. Ignition and oxidation of lean CO/H_2 fuel blends in air. *J. Prop. Power*, 23(6):1291–1304, 2007.

[94] D. J. Beerer and V. G. McDonell. Autoignition of hydrogen and air inside a continuous flow reactor with application to lean premixed combustion. *J. Eng. Gas Turbines Power*, 130(051507), 2008.

[95] S. Samuelsen, V. McDonell, J. Chen, and V. Jermakian. Correlation of ignition delay with fuel composition and state for application to gas turbine combustion. Final Report, UCI-ARTR-00-5(e), University of California Irvine, 2003.

[96] R. J. Santoro. Autoignition studies of syngas and hydrogen (SGH) fuels. Final Report, UTSR Project No. 05-01-SR117, Pennsylvania State University, 2009.

[97] L. J. Spadaccini and J. A. Tevelde. Autoignition characteristics of aircraft-type fuels. *Combust. Flame*, 46:283–300, 1982.

[98] A. Lefebvre, W. Freeman, and L. Cowell. Spontaneous ignition delay characteristics of hydrocarbon fuel/air mixtures. NASA/CR-175064, NASA, 1986.

[99] M. P. Burke, M. Chaos, Y. Ju, F. L. Dryer, and S. J. Klippenstein. Comprehensive H_2/O_2 kinetic model for high-pressure combustion. *Int. J. Chem. Kinet.*, 44(7):444–474, 2012.

[100] S.B. Pope. Simple models of turbulent flows. *Phys. Fluids*, 23(011301), 2011.

[101] P. J. Colucci, F. A. Jaberi, P. Givi, and S. B. Pope. Filtered density function for large eddy simulation of turbulent reacting flows. *Phys. Fluids*, 10(2):499–515, 1998.

[102] P. Gokulakrishnan, A. Kazakov, and F. Dryer. Comparison of numerical and experimental kinetic data for flow reactor systems: Mixing effects, 2003. Paper PK10, Third U.S. Joint Meeting of the Combustion Institute.

[103] E. Mastorakos. Ignition of turbulent non-premixed flames. *Prog. Energy Combust. Sci.*, 35:57–97, 2009.

[104] W. T. Peschke and L. J. Spadaccini. Determination of autoignition and flame speed characteristics of coal gases having medium heating values. Epri ap-4291, project 2357-1, UTRC East Hartford, CT, 1985.

[105] N. Peters. The turbulent burning velocity for large-scale and small-scale turbulence. *J. Fluid Mech.*, 384:107–132, 1999.

[106] G. Damköhler. Der Einfluß der Turbulenz auf die Flammengeschwindigkeit in Gasgemischen. *Z. Elktrochem. Angew. P.*, 46(11):601–626, 1940.

[107] John W. S. Rayleigh. The Explanation of Certain Acoustical Phenomena. *Nature*, 18(455):319–321, July 1878.

[108] Ben T. Zinn and Timothy C. Lieuwen. Combustion instabilities: Basic concepts. In Lieuwen and Yang [151], chapter 1.

[109] Hukam C. Mongia, T. J. Held, G. C. Hsiao, and R. P. Pandalai. Challenges and Progress in Controlling Dynamics in Gas Turbine Combustors. *Journal of Propulsion and Power*, 19(5):822–829, 2003.

[110] Tim C. Lieuwen and Ben T. Zinn. The role of equivalence ratio oscillations in driving combustion instabilities in low NOx gas turbines. *Symposium (International) on Combustion*, 27(2):1809–1816, January 1998.

[111] Thierry Schuller, Daniel Durox, and Sébastien M. Candel. Dynamics of and noise radiated by a perturbed impinging premixed jet flame. *Combustion and Flame*, 128(1-2):88–110, January 2002.

[112] Werner Krebs, Sven Bethke, Joachim Lepers, Patrick Flohr, Bernd Prade, Cliff Johnson, and Stan Sattinger. Thermoacoustic design tools and passive control: Siemens power generation approaches. In Lieuwen and Yang [151], chapter 5.

[113] Jeffrey M. Cohen and Andrzej Banaszuk. Factors Affecting the Control of Unstable Combustors. *Journal of Propulsion and Power*, 19(5):811–821, 2003.

[114] Jeffrey M. Cohen, N. M. Rey, C. a. Jacobson, and T. J. Anderson. Active Control of Combustion Instability in a Liquid-Fueled Low-NOx Combustor. *Journal of Engineering for Gas Turbines and Power*, 121(2):281, 1999.

[115] Jacob E. Temme, Patton M. Allison, and James F. Driscoll. Combustion instability of a lean premixed prevaporized gas turbine combustor studied using phase-averaged PIV. *Combustion and Flame*, 161(4):958–970, April 2014.

[116] K. Zähringer, Daniel Durox, and F. Lacas. Helmholtz behavior and transfer function of an industrial fuel swirl burner used in heating systems. *International Journal of Heat and Mass Transfer*, 46(18):3539–3548, 2003.

[117] Jong Ho Uhm and Sumanta Acharya. Low-bandwidth open-loop control of combustion instability. *Combustion and Flame*, 142(4):348–363, 2005.

[118] Daniel Durox, Thierry Schuller, N. Noiray, a. L. Birbaud, and Sébastien M. Candel. Rayleigh criterion and acoustic energy balance in unconfined self-sustained oscillating flames. *Combustion and Flame*, 156(1):106–119, 2009.

[119] K. R. McManus, Thierry Poinsot, and Sébastien M. Candel. A review of active control of combustion instabilities. *Progress in Energy and Combustion Science*, 19(1):1–29, 1993.

[120] Sébastien Ducruix, Thierry Schuller, Daniel Durox, and Sébastien M. Candel. Combustion Dynamics and Instabilities: Elementary Coupling and Driving Mechanisms. *Journal of Propulsion and Power*, 19(5):722–734, September 2003.

[121] Peter Weigand, Wolfgang Meier, Xu Ru Duan, W. Stricker, and Manfred Aigner. Investigations of swirl flames in a gas turbine model combustor I. Flow field, structures, temperature, and species distributions. *Combustion and Flame*, 144(1-2):205–224, January 2006.

[122] Robert Giezendanner-Thoben, O. Keck, Peter Weigand, Wolfgang Meier, Ulrich Meier, W. Stricker, and Manfred Aigner. Periodic combustion instabilities in a swirl burner studied by phase-locked planar laser-induced fluorescence. *Combustion Science and Technology*, 175:721–741, 2003.

[123] Robert Giezendanner-Thoben, Peter Weigand, Xu Ru Duan, Wolfgang Meier, Ulrich Meier, B. Lehmann, W. Stricker, and Manfred Aigner. Characterization of Thermoacoustic Instabilities in a Gas Turbine Model Combustor by Laser Spectroscopic Measurements. In *Proceeding of the European Combustion Meeting 2003*, 2003.

[124] Adam M. Steinberg, Isaac Boxx, Michael Stöhr, Wolfgang Meier, and Campbell D. Carter. Effects of Flow Structure Dynamics on Thermoacoustic Instabilities in Swirl-Stabilized Combustion. *AIAA Journal*, 50(4):952–967, April 2012.

[125] Michael Stöhr, Christoph M. Arndt, and Wolfgang Meier. Effects of Damköhler number on vortexflame interaction in a gas turbine model combustor. *Proceedings of the Combustion Institute*, 34(2):3107–3115, January 2013.

[126] Adam M. Steinberg, Isaac Boxx, Michael Stöhr, Campbell D. Carter, and Wolfgang Meier. Flowflame interactions causing acoustically coupled heat release fluctuations in a thermo-acoustically unstable gas turbine model combustor. *Combustion and Flame*, 157(12):2250–2266, December 2010.

[127] Xu Ru Duan, Wolfgang Meier, Peter Weigand, and B. Lehmann. Phase-resolved laser Raman scattering and laser Doppler velocimetry applied to periodic instabilities in a gas turbine model combustor. *Applied Physics B*, 80(3):389–396, January 2005.

[128] Michael Stöhr, Isaac Boxx, Campbell D. Carter, and Wolfgang Meier. Experimental study of vortex-flame interaction in a gas turbine model combustor. *Combustion and Flame*, 159(8):2636–2649, August 2012.

[129] Michael Stöhr, Christoph M. Arndt, and Wolfgang Meier. Transient effects of fuelair mixing in a partially-premixed turbulent swirl flame. *Proceedings of the Combustion Institute*, 35(3):3327–3335, July 2015.

[130] Michael Stöhr, R. Sadanandan, and Wolfgang Meier. Phase-resolved characterization of vortexflame interaction in a turbulent swirl flame. *Experiments in Fluids*, 51(4):1153–1167, June 2011.

[131] Wolfgang Meier, Xu Ru Duan, and Peter Weigand. Investigations of swirl flames in a gas turbine model combustor II. Turbulencechemistry interactions. *Combustion and Flame*, 144(1-2):225–236, January 2006.

[132] Patton M. Allison, James F. Driscoll, and Matthias Ihme. Acoustic characterization of a partially-premixed gas turbine model combustor: Syngas and hydrocarbon fuel comparisons. *Proceedings of the Combustion Institute*, 34(2):3145–3153, January 2013.

[133] Patton M. Allison, Yun Tao Chen, and James F. Driscoll. Investigation of Dimethyl Ether Combustion Instabilities in a Partially - Premixed Gas Turbine Model Combustor Using High-Speed Laser Diagnostics. In *AIAA Aerospace Sciences Meeting*, number January, Reston, Virginia, January 2014. American Institute of Aeronautics and Astronautics.

[134] Patton M. Allison, Yun Tao Chen, Matthias Ihme, and James F. Driscoll. Coupling of flame geometry and combustion instabilities based on kilohertz formaldehyde PLIF measurements. *Proceedings of the Combustion Institute*, 35(3):3255–3262, July 2015.

[135] Yee Chee See and Matthias Ihme. Large eddy simulation of a partially-premixed gas turbine model combustor. *Proceedings of the Combustion Institute*, September 2014.

[136] J. P. Hathout, M. Fleifil, A. M. Annaswamy, and Ahmed F. Ghoniem. Combustion Instability Active Control Using Periodic Fuel Injection. *Journal of Propulsion and Power*, 18(2):390–399, March 2002.

[137] Sébastien M. Candel, Daniel Durox, Thierry Schuller, Jean-François Bourgouin, and Jonas P. Moeck. Dynamics of Swirling Flames. *Annual Review of Fluid Mechanics*, 46(1):147–173, January 2014.

[138] N. Noiray, Daniel Durox, Thierry Schuller, and Sébastien M. Candel. A unified framework for nonlinear combustion instability analysis based on the flame describing function. *Journal of Fluid Mechanics*, 615:139–167, November 2008.

[139] Thierry Schuller, Daniel Durox, Paul Palies, and Sébastien M. Candel. Acoustic decoupling of longitudinal modes in generic combustion systems. *Combustion and Flame*, 159(5):1921–1931, May 2012.

[140] Paul Palies, Daniel Durox, Thierry Schuller, and Sébastien M. Candel. Nonlinear combustion instability analysis based on the flame describing function applied to turbulent premixed swirling flames. *Combustion and Flame*, 158(10):1980–1991, October 2011.

[141] Camilo Fernando Silva, Franck Nicoud, Thierry Schuller, Daniel Durox, and Sébastien M. Candel. Combining a Helmholtz solver with the flame describing function to assess combustion instability in a premixed swirled combustor. *Combustion and Flame*, 160(9):1743–1754, September 2013.

[142] Christian Brackmann, Jenny Nygren, Xiao Bai, Zhongshan Li, Henrik Bladh, Boman Axelsson, Ingemar Denbratt, Lucien Koopmans, Per-Erik Bengtsson, and Marcus Aldén. Laser-induced fluorescence of formaldehyde in combustion using third harmonic Nd:YAG laser excitation. *Spectrochimica Acta Part A: Molecular and Biomolecular Spectroscopy*, 59(14):3347–3356, December 2003.

[143] Yun Tao Chen and James F. Driscoll. Experimental Studies and Modeling of Acoustic Instabilities in a Gas Turbine Model Combustor. In *AIAA Aerospace Sciences Meeting*, number January, Kissimmee, FL, 2015.

[144] J.-M. Samaniego, F.N. Egolfopoulos, and C. T. Bowman. CO2* Chemiluminescence in Premixed Flames. *Combustion Science and Technology*, 109(1-6):183–203, 1995.

[145] J. G. Lee and D. A. Santavicca. Experimental Diagnostics for the Study of Combustion Instabilities in Lean Premixed Combustors. *Journal of Propulsion and Power*, 19(5):735–750, 2003.

[146] B. O. Ayoola, R. Balachandran, J. H. Frank, E. Mastorakos, and C. F. Kaminski. Spatially resolved heat release rate measurements in turbulent premixed flames. *Combustion and Flame*, 144(1-2):1–16, 2006.

[147] Frank P. Incropera, David P. Dewitt, Theodore L. Bergman, and Adrienne S. Lavine. *Fundamentals of Heat and Mass Transfer*. Wiley, 2007.

[148] Stuart W. Churchill and Humbert H.S. Chu. Correlating equations for laminar and turbulent free convection from a vertical plate. *International Journal of Heat and Mass Transfer*, 18(11):1323 – 1329, 1975.

[149] H. Tennekes and J. L. Lumley. *A First Course in Turbulence*. MIT Press, 1972.

[150] Constantine Arcoumanis, Choongsik Bae, Roy Crookes, and Eiji Kinoshita. The potential of di-methyl ether (DME) as an alternative fuel for compression-ignition engines: A review. *Fuel*, 87(7):1014–1030, June 2008.

[151] Timothy C. Lieuwen and Vigor Yang, editors. *Combustion Instabilities in Gas Turbine Engines*, volume 210 of *Progress in Astronautics and Aeronautics*. AIAA, 2005.